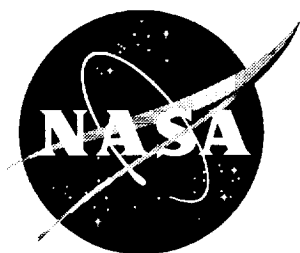


NASA/CR-1998-208721



Operational Data Reduction Procedure for Determining Density and Vertical Structure of the Martian Upper Atmosphere From Mars Global Surveyor Accelerometer Measurements

*George J. Cancro, Robert H. Tolson, and Gerald M. Keating
The George Washington University
Joint Institute for Advancement of Flight Sciences
Langley Research Center, Hampton, Virginia*

National Aeronautics and
Space Administration

Langley Research Center
Hampton, Virginia 23681-2199

Prepared for Langley Research Center
under Cooperative Agreement NCC1-104

October 1998

Available from the following:

NASA Center for AeroSpace Information (CASI)
7121 Standard Drive
Hanover, MD 21076-1320
(301) 621-0390

National Technical Information Service (NTIS)
5285 Port Royal Road
Springfield, VA 22161-2171
(703) 487-4650

Abstract

The success of aerobraking at Mars by the Mars Global Surveyor (MGS) spacecraft was partly due to the analysis of MGS accelerometer data. Accelerometer data was used to determine the effect of the atmosphere on each orbit, to characterize the nature of the atmosphere, and to predict the atmosphere for future orbits. To properly interpret the accelerometer data, a data reduction procedure was developed which utilizes inputs from the spacecraft, the MGS Navigation Team, and pre-mission aerothermodynamic studies to produce density estimations at various points and altitudes on the planet. This data reduction procedure was based on the calculation of acceleration due to aerodynamic forces from the accelerometer data by considering acceleration components due to gravity gradient, solar pressure, angular motion of the instrument, instrument bias, thruster activity, and a vibration component due to the motion of the damaged solar array. Methods were developed to calculate all of the acceleration components including a 4 degree of freedom dynamics model used to gain a greater understanding of the damaged solar array. An iteration process was developed to calculate density by calculating deflection of the damaged array and a variable force coefficient. The total error inherent to the data reduction procedure was calculated as a function of altitude and density considering contributions from ephemeris errors, errors in force coefficient, and instrument errors due to bias and digitization. Comparing the results from this procedure to the data of other MGS Teams has demonstrated that this procedure can quickly and accurately describe the density and vertical structure of the Martian upper atmosphere.

Table of Contents

Abstract.....	i
Table of Contents.....	iii
List of Figures	v
List of Tables	vii
Nomenclature.....	viii
1. Introduction.....	1
2. MGS Aerobraking Scenario.....	3
2.1 Accelerometer Instrument.....	3
2.2 MGS Aerobraking Configuration	3
2.3 Complexities of the MGS Aerobraking Mission	4
2.4 Accelerometer Team Responsibilities	6
2.5 Description of Panel Malfunction	8
3. Analysis of Acceleration Data	10
3.1 Development of the Acceleration Term.....	10
3.2 Development of the Spacecraft Velocity Term	21
3.3 Development of the Ballistic Coefficient Term	22
4. Operational Data Reduction Procedure	28
4.1 Operational Constraints	28
4.2 Operational Accelerometer Instrument.....	29
4.3 Quantity of Accelerometer Data Necessary to Perform Operations.....	31
4.4 Operational Data Reduction Process	34
4.5 Special Products	40
4.6 Prediction Methods.....	43
5. Analysis of Process Errors	45
5.1 Ephemeris Errors.....	45
5.2 Errors in Determining Ballistic Coefficient	46
5.3 Errors in Determining Bias.....	47

5.4 Errors due to Instrument Output.....	48
5.5 Total Data Reduction Process Error	49
6. Verification of Accelerometer Results.....	51
6.1 Data Reduction Process Verification	51
6.2 Prediction Scheme Verification	54
7. The Effect of Panel Vibration on MGS and the Accelerometer Data Reduction Process.....	57
7.1 Effectiveness of the 4 DOF Dynamics Model	58
7.2 Verification of the Dynamics Model And Assumptions.....	59
7.3 Sensitivity Studies on Panel Physical Parameters	61
7.4 Averaging Techniques Used to Compensate for Vibrating Panel Effects.....	64
8. Conclusions	65
References	67
APPENDIX A: Description of Quick-Look Data Product	69
APPENDIX B: 4 DOF Derivation for Eliminating SAM panel Motions from Z-Accelerometer Data	74
APPENDIX C: LaRC Aerothermodynamic Database for MGS Operations	80
APPENDIX D: Planetary Ephemeris and Physical Data	89
APPENDIX E: MGS Physical Properties	90
APPENDIX F: Verification of 4 DOF Model Derivation.....	91

List of Figures

Figure 2-1: MGS aerobraking configuration	4
Figure 2-2: Diagram of basic MGS project team relationships	7
Figure 2-3: Spare yoke with suspected failure mode	9
Figure 3-1: Typical spacecraft angular rates (Orbit 162)	16
Figure 3-2: Typical x, y and z angular accelerations (Orbit 162)	16
Figure 3-3: Typical thruster fire times (Orbit 16)	18
Figure 3-4: Acceleration data with large amplitude vibrations (Orbit 95)	19
Figure 3-5: Diagram of 2-body 4 DOF model used to estimate moving panel acceleration	19
Figure 3-6: Ux and Uy coordinate definition	23
Figure 3-7: Force coefficient in spacecraft z-direction, C_z , vs. density level for all panel deflections	24
Figure 3-8: C_z tables for free molecular densities (0 degree SAM Deflection and 10 degree SAM Deflection)	25
Figure 3-9: Typical quaternions (Orbit 162)	26
Figure 3-10: Typical Ux and Uy diagram (Orbit 162)	27
Figure 4-1: Typical IMU temperatures and voltage to IMU heater (Orbit 162)	30
Figure 4-2: Results of Accelerometer Data Rate Simulation	32
Figure 4-3: Results of accelerometer data rate simulation considering all possible outcomes	33
Figure 4-4: Data reduction process flow chart	34
Figure 4-5: Typical accelerometer instrument bias calculation	36
Figure 4-6: Development of density flow chart	37
Figure 4-7: Typical z-force coefficient and panel deflection from Orbit 162	38
Figure 4-8: Comparison of the operational averaging techniques	39
Figure 4-9: Look-ahead model diagram	44
Figure 5-1: Accelerometer process error vs. model altitude and density	50

Figure 6-1: Comparison of panel position calculated using accelerometer data and sun sensor data.....	52
Figure 6-2: Orbital decay comparison of NAV and ACC using $\rho\sqrt{H_s}$ product	53
Figure 6-3: Comparison of effectiveness of persistence, 5-orbit mean, longitudinal wave, and look ahead prediction schemes over Orbits 100-200	55
Figure 7-1: Acceleration profiles for Orbit 162 - raw data, reduced data using 4 DOF model, and reduced data using band-pass filtering method	58
Figure 7-2: Acceleration profiles for Orbit 95 - raw data, reduced data using 4 DOF model, and reduced data using band-pass filtering method	59
Figure 7-3: Sensitivity study on SAM moment of inertia about the spacecraft x-axis at the SAM center of mass.....	62
Figure 7-4: Sensitivity study on SAM mass	62
Figure 7-5: Sensitivity study on SAM center of gravity position	63
Figure 7-6: Sensitivity study on crack-line position.....	63
Figure 7-7: Comparison between 4 DOF dynamics model and 40 pt (left) and 6 pt running means (right) for Orbit 162.....	64

List of Tables

Table 3-1: Aerodynamic Force Acceleration Simulation Results	11
Table 3-2: Gravity Gradient Acceleration Simulation Results	13
Table 3-3: Results of Range Error Study Between Exact Ephemeris and Ephemeris Generated From Osculating Elements at Periapsis	22
Table 4-1: Telemetry Data Types And Rates For Operations	29
Table 4-2: Results From Reliability of Accelerometer Data Simulation	33
Table 5-1: Total Altitude Error Results	46
Table 5-2: Ephemeris Timing Error Results for 0.1 Seconds of Timing Error	46
Table 5-3: Bias Percent Error as a Function of Count Level	48
Table 5-4: Quantization and Data Rate Error Results	48
Table 5-5: Total Data Reduction Process Error	49
Table 6-1: Results of NAV Simulation Runs with Accelerometer Calculated Effective Scale Height.....	54
Table 7-1: Crack-Line Position and Resulting Physical Parameters for Sensitivity Study.....	61

Nomenclature

α_{sun}	= right ascension of the sun in Mars equatorial coordinates, rad
$\alpha_{\text{s/c}}$	= right ascension of the spacecraft in Mars equatorial coordinates, rad
$\overline{\alpha}$	= angular acceleration of the spacecraft, rad/s ²
A	= spacecraft reference area, 17.03 m ²
ACC	= Accelerometer
ADL	= Atmospheric Disturbance Level
a,e,i,w, Ω , τ	= Keplerian orbital elements: semi-major axis, eccentricity, inclination, argument of periapsis, longitude of ascending node, time of periapsis
a_z	= acceleration due to aerodynamic forces in spacecraft z-axis, m/s ²
$a_{z_{BP}}$	= band-pass filtered z-axis acceleration, m/s ²
BUS	= spacecraft main body
C_1, C_2	= parameters of band-pass filter
$C_x C_y C_z$	= force coefficients in the spacecraft x, y, z axes, respectively
$C_{Mx} C_{My} C_{Mz}$	= moment coefficients about the spacecraft x, y, z axes, respectively
c	= speed of light, 3*10 ⁸ m/s
δ_{sun}	= declination of the sun in Mars equatorial coordinates, rad
$\delta_{\text{s/c}}$	= declination of the spacecraft in Mars equatorial coordinates, rad
DCM	= Direction Cosine Matrix
DOF	= Degrees Of Freedom
$\Delta \overline{R}$	= areocentric distance to accelerometer instrument, km
$\Delta r, \Delta \theta, \Delta z$	= cylindrical components of $\Delta \overline{R}$
ETC	= Ephemeris Timing Correction
F_s	= solar constant, 590 W/m ² at Mars
f	= true anomaly
f_m	= flattening of Mars
g	= acceleration of gravity on Mars surface, 3.4755 m/s ²
HGA	= High Gain Antenna

H_s	= scale height, km
h	= angular momentum of an orbit, km^2/s
IMU	= Inertial Measurement Unit
L	= longitude, deg
\dot{L}	= rotation rate of Mars, deg/day
LMA	= Lockheed Martin Astronautics
LST	= Local Solar Time, Martian hrs
μ	= gravitational constant for Mars, $42828 \text{ km}^3/\text{s}^2$
m	= spacecraft mass, kg
MGS	= Mars Global Surveyor
NAV	= Navigation
$\bar{\omega}$	= angular velocity of the spacecraft, rad/s
ρ	= density, kg/km^3
ρ_0	= base density, kg/km^3
Q	= free stream heat flux, W/cm^2
q	= dynamic pressure, N/m^2
q_r	= reflectance factor for solar pressure
q_1, q_2, q_3, q_4	= spacecraft quaternions
\bar{R}	= areocentric distance to accelerometer instrument, km
\bar{R}_{cm}	= areocentric distance to spacecraft center of mass, km
R, θ, Z	= cylindrical orbit coordinates: distance from planet, angular distance along orbit path, distance perpendicular to orbit path
r_{cm}	= radial distance from Mars center to spacecraft center of mass, km
SAM	= Solar Array Minus (on -Y spacecraft axis)
SAP	= Solar Array Plus (on +Y spacecraft axis)
SZA	= Solar Zenith Angle, deg
S/C	= Spacecraft
$\dot{\theta}$	= angular velocity in orbit plane, deg/s
θ_δ	= deflection angle of the damaged solar array, deg

θ_i	= Incidence angle of solar radiation, deg
θ_L	= areocentric latitude, deg
θ_L'	= areodetic latitude, deg
T	= spring torque, in-lbs
T_0	= base temperature, K
T_1	= temperature change with altitude, K/km
TCM	= Trajectory Correction Maneuver
U_x, U_y	= direction sines describing the orientation of the relative wind with respect to the spacecraft x and y axes
v	= orbital velocity of spacecraft, km/s
z	= areodetic altitude, km
z_0	= base altitude, km

1. Introduction

The Mars Global Surveyor (MGS) spacecraft is NASA's first orbiter to return to the red planet in 20 years. MGS represents the first project in the NASA Mars Surveyor Program, a series of missions to Mars every 25 months over a period of 10 years. The goals of the Mars Surveyor Program are to analyze the physical and atmospheric properties of the planet and gain a greater understanding of how Mars formed [1]. The MGS mission begins this analysis by achieving the following science goals:

- (1) Successfully characterize the gravity field and surface properties of the planet,
- (2) Establish the nature of the magnetic field, and
- (3) Monitor the global structure of the atmosphere [2].

To accomplish these goals while maintaining a low budget, a technique called "aerobraking" was planned to position the MGS spacecraft close enough to the planet for onboard science instruments to properly collect data. Aerobraking is the process of using atmospheric drag to remove kinetic energy from an orbit. The MGS spacecraft used repeated encounters with the atmosphere (aerobraking passes) to gradually change a long period-high eccentricity orbit to a short period-low eccentricity orbit. By relying on multiple aerobraking passes instead of propulsive maneuvers to modify the orbit, less fuel was needed during the MGS mission and, therefore, the design weight of the spacecraft was reduced.

Aerobraking had to be monitored during each pass through the atmosphere to ensure the safety of the spacecraft and the effectiveness of the technique. To monitor aerobraking, Keating et al. [Keating, G.M., Tolson, R.H., Bougher S.W., Blanchard R.C., "MGS Accelerometer Proposal for JPL Operations, Dec 1995. Available from author] proposed the use of on-board accelerometer data to produce density estimations as a function of altitude for each pass and density predictions for future passes. In accord with this proposal, a data reduction procedure was created. This paper presents the data reduction procedure and demonstrates the effectiveness of this procedure in calculating

and predicting densities for 149 aerobraking orbits completed by MGS. These 149 orbits occurred during the first 201 orbits at Mars, called the 1st phase of aerobraking.

First, this paper discusses the MGS aerobraking scenario including descriptions of the accelerometers, the MGS spacecraft and the malfunction of one of the solar arrays on the spacecraft. Next, the relationship between atmospheric density and acceleration due to aerodynamic forces is examined. Methods were developed to determine each of the components of this relationship. One such method is a dynamics model designed to compensate for the effects of the damaged solar array on the measured acceleration. These methods are combined with an iterative process to form the data reduction procedure which determines density from accelerometer data. The errors inherent to the data reduction procedure are calculated by considering ephemeris errors, force coefficient errors, and instrument errors. The data reduction procedure is verified using panel deflection data determined by the MGS Spacecraft Team and orbital period reduction data generated by the MGS Navigation Team.

Finally, the methods developed in this report are used to give a greater insight into the solar array malfunction. The dynamics model mentioned briefly above, successfully compensates for 90% of vibration signal associated with the solar array malfunction. Sensitivity studies were performed using the dynamics model to determine the source of the remaining 10%.

2. MGS Aerobraking Scenario

This section will describe the key elements of the MGS aerobraking scenario including the accelerometer instrument, the aerobraking configuration, the complexities of aerobraking at Mars, and the role of the team monitoring the aerobraking process using on-board accelerometer data.

During deployment, one of the two solar arrays on the MGS spacecraft malfunctioned. This section also gives a brief description of this malfunction and how the malfunction effects the analysis of accelerometer data.

2.1 Accelerometer Instrument

The MGS accelerometers are instruments that measure the change in velocity of the spacecraft over a time interval by measuring the fluctuations of voltage to an electromagnetic assembly. The assembly is essentially a magnetic proof mass suspended on a thin flexure in an electromagnetically charged ring. When the spacecraft accelerates, the position of the proof mass inside the ring is maintained by varying the voltage. After the instrument is calibrated in a known g-field, the acceleration of the spacecraft can be calculated by recording the change in voltage to the ring.

2.2 MGS Aerobraking Configuration

Several minutes before beginning the aerobraking pass through the Martian atmosphere, the MGS spacecraft was placed in the aerobraking configuration. The aerobraking configuration, shown in Figure 2-1, consists of the spacecraft oriented with the main engine nozzle (spacecraft -z axis) pointed in the direction of spacecraft motion or the “velocity vector” and the High Gain Antenna (spacecraft x axis) pointed toward the planet, “nadir”, or away from the planet, “zenith”. The two solar arrays, solar array plus

(SAP) and solar array minus (SAM), extend from the +Y and -Y faces of the main body, or “BUS”, respectively. The solar arrays consist of two separate panels (inner and outer) and are composed of carbon-carbon composite facesheets over honeycomb core. Gallium arsenide and silicon solar cells cover only one face of these arrays. During aerobraking, the majority of the atmospheric drag on the spacecraft was produced by these solar arrays which were planned to be oriented with the non-cell face into the wind and swept back 30 degrees for aerodynamic stability. The four accelerometers used during aerobraking are contained with four gyros inside the Inertial Measurement Unit (IMU). The IMU is located on the top deck of the BUS along with the other MGS science instruments.

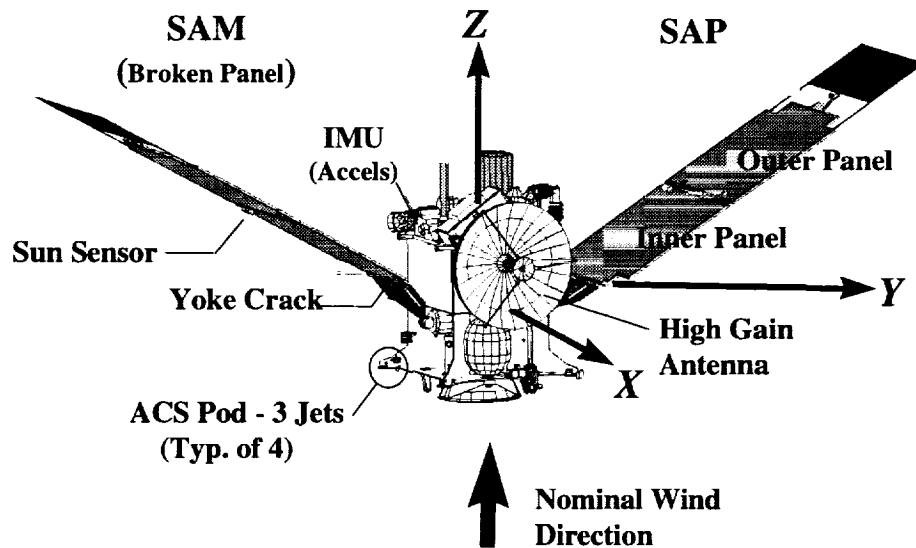


Figure 2-1: MGS aerobraking configuration

2.3 Complexities of the MGS Aerobraking Mission

Aerobraking is not a new technique. Planetary aerobraking was used at Venus during the Magellan mission to circularize the orbit [3] and used again in the Termination Experiment to study the Venusian atmosphere and improve the estimates of the aerodynamic properties of the Magellan spacecraft [4].

Planetary aerobraking at Mars represented a new and unique challenge for the following four reasons.

1) Success of the MGS science mission depended on aerobraking.

For a successful science mission at Mars, aerobraking must enable the MGS spacecraft to safely reach the low-altitude, sun-synchronous, circular mapping orbit required by the science instruments. In contrast, the Magellan primary science mission had been completed before aerobraking began at Venus.

2) The Martian upper atmosphere characteristics were relatively unknown.

Three probes have entered the Martian neutral upper atmosphere: Viking 1, Viking 2, and Mars Pathfinder. The data collected by these entry probes only represents several data points at aerobraking altitudes. Aerobraking at Mars was dependent on the limited data from previous probes and any new data collected by MGS. In comparison, a complete model of the Venusian atmosphere had already been developed before Magellan began aerobraking [5].

3) The MGS spacecraft performed aerobraking in aerodynamic regimes not experienced by any other orbiter at any planet.

For aerodynamic analysis, the atmosphere is divided into regimes defined by the Knudsen number. Knudsen number is the mean free path of the atmospheric molecules divided by the characteristic length of the spacecraft. The free molecular regime is defined by Knudsen numbers greater than one. The transitional flow regime is defined by Knudsen numbers between 1.0 and 0.01. At Venus, Magellan reached the edges of the transition regime (Knudsen number approximately 3.0), whereas, the MGS spacecraft was designed to perform aerobraking well into the rarefied transition regime (Knudsen numbers ranging from 0.7 to 0.07) [6]. Extensive computational studies had to be performed to calculate the aerodynamic reactions of the spacecraft in this environment [7].

4) The density of the Martian atmosphere can increase rapidly due to dust storms

The MGS spacecraft arrived at Mars during southern hemisphere spring, near the time when dust storms are most likely to form on the planet [8]. These storms raise the temperature of the lower atmosphere, thereby, expanding the upper atmosphere. If the MGS spacecraft unknowingly encountered such an expansion, the atmosphere could overheat the solar arrays on the spacecraft.

2.4 Accelerometer Team Responsibilities

To compensate for the complexities above, the Accelerometer (ACC) Team was formed from senior personnel and graduate students of the George Washington University at NASA Langley. Using inputs from the MGS spacecraft and the MGS Navigation (NAV) Team, the ACC Team was assigned to support the aerobraking process by:

- 1) Producing atmospheric structure information on each aerobraking pass,
- 2) Supporting the NAV Team by providing density and density scale height information, and
- 3) Providing predictions of density on future aerobraking passes.

By producing atmospheric structure information for each pass, the ACC Team provided critical results concerning the upper atmosphere to the Atmospheric Advisory Group (AAG), which was responsible for monitoring the entire atmosphere on Mars. The ACC Team also supported the NAV Team, responsible for orbit determination, by providing density at periapsis and a scale height used to determine the orbit during the aerobraking pass. Scale height is the altitude increase over which the density decreases by a factor of e . Finally, by providing predictions of density on future aerobraking passes, the ACC Team assisted the MGS project to plan future passes and ensure the safety of the spacecraft.

To accomplish these tasks, a procedure was developed for determining several atmospheric properties including density, scale height, pressure, temperature, dynamic

pressure and free-stream heatflux for each aerobraking pass. The procedure was separated into two steps: Accelerometer Data Reduction and Atmospheric Data Modeling as shown in Figure 2-2 below.

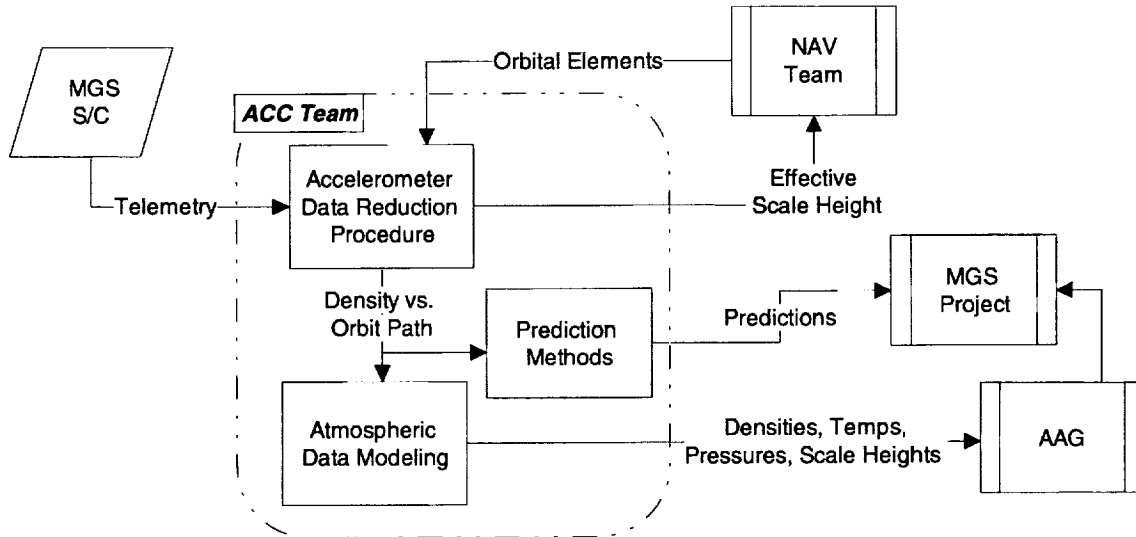


Figure 2-2: Diagram of basic MGS project team relationships

The accelerometer data reduction procedure used telemetry from the MGS spacecraft and orbital elements supplied by the NAV Team to calculate density along the orbit path. The atmospheric data modeling procedure used the density and orbit path information to develop empirical models that characterized the atmosphere. The empirical models used during this procedure include (1) constant temperature atmospheric model which is defined by two parameters (base density and scale height), (2) linear temperature model of the atmosphere defined by three parameters (base density, base temperature and temperature change with altitude), and (3) Bates temperature model defined by 6 parameters (exospheric temperature, lower atmospheric temperature, base density, temperature of the inflection point, shape factor above the inflection point and shape factor below the inflection point). Once the atmospheric density profile was modeled, any information on densities, temperatures, pressures or scale heights could be determined at any point above the planet. To determine future densities, several prediction methods were developed from observations of density trends in longitude and

latitude. This process culminated in a “quick-look” report distributed to all MGS project teams. A typical quick-look report is described in Appendix A.

This paper describes in detail the methods used in the accelerometer data reduction procedure as well as several prediction methods. The methods used in the atmospheric data modeling procedure are not presented in this paper but are available in the paper by Wilkerson [Wilkerson, B., “Upper Atmospheric Modeling for Mars Global Surveyor Aerobraking Using Least Squared Processes,” Graduate Research Paper for George Washington University, 1998. Available from author].

2.5 Description of Panel Malfunction

On November 6, 1996, MGS spacecraft telemetry indicated that the solar array on the spacecraft -Y axis (SAM) failed to deploy into the fully extended position. To remedy the failed deployment, the spacecraft was oriented such that aerodynamic forces would extend the SAM during aerobraking passes at Mars. Early aerobraking passes showed the SAM position moving closer to full extension. However, on pass 15 the MGS spacecraft unexpectedly entered a high density region of the Martian atmosphere forcing the panel to deflect past full extension by approximately 17 degrees based on sun sensor measurements.

Following several aerobraking orbits at higher altitudes, aerobraking was stopped altogether and an extensive testing program was initiated to determine the cause of the over-extension and to evaluate the risk of continued aerobraking. After 25 days, it was decided that the most likely scenario was that a crack had developed in the facesheet of the SAM yoke. This crack, thought to be due to the initial deployment malfunction, was apparently located on the compression facesheet where the thickness of the facesheet was reduced. This theory was developed using spacecraft data and ground test data from a spare MGS yoke [9]. The crack produced during the ground test is highlighted in Figure 2-3.

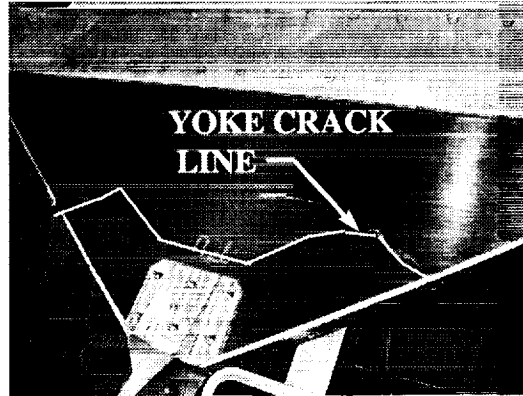


Figure 2-3: Spare yoke with suspected failure mode

Assuming the integrity of the cracked yoke would not degrade under smaller forces, aerobraking resumed at altitudes with lower dynamic pressures.

The analysis of accelerometer data had to consider the malfunction of the SAM panel. The SAM panel, under the force of the atmosphere, deflected several degrees during each aerobraking pass. The panel was also vibrating during each pass. Methods were developed to compensate for both the deflection and the vibration.

3. Analysis of Acceleration Data

The aerodynamic force relationship forms the main equation for determining density using data from an onboard accelerometer. For MGS, the z-accelerometer was the primary data source used to measure the acceleration due to aerodynamic forces. The equation that describes the density as a function of the acceleration due to aerodynamic forces in the z-direction is

$$\rho = \frac{2 m a_z}{v^2 C_z A} \quad (3-1)$$

In this equation, ρ is the atmospheric density, a_z is the acceleration of the spacecraft in the spacecraft z-direction due to aerodynamic forces, v is the velocity of the spacecraft with respect to the atmosphere, and $m/C_z A$ is the spacecraft ballistic coefficient. The ballistic coefficient consists of the force coefficient in the spacecraft z-direction, the spacecraft mass, and the spacecraft reference area. Methods developed to determine the acceleration, the spacecraft velocity and the ballistic coefficient are discussed in the sections below.

3.1 Development of the Acceleration Term

To determine the acceleration due to aerodynamic forces, all non-aerodynamic effects must be removed from the acceleration measured by on-board accelerometers. The measured acceleration signal can be written as

$$\bar{a}_{measured} = \bar{a}_{aero} + \bar{a}_{gravgrad} + \bar{a}_{solar} + \bar{a}_{bias} + \bar{a}_{angular} + \bar{a}_{thruster} + \bar{a}_{vibration} \quad (3-2)$$

The terms on the right hand side of Equation 3-2 represent the acceleration due to aerodynamic forces, the gravity gradient acceleration, the acceleration due to solar pressure, the instrument bias, the acceleration due to angular motion of the spacecraft, the

acceleration produced during thruster activity, and the acceleration due to vibration of the damaged solar array. Each of these terms are described in more detail in Sections 3.1.1 through 3.1.7.

3.1.1 Acceleration Due To Aerodynamic Forces

The acceleration due to aerodynamic forces is a function of the spacecraft size, spacecraft velocity, spacecraft mass, and the density and flight regime of the atmosphere. To compare the magnitude of the acceleration due to aerodynamic forces to the other terms on the right hand side of Equation 3-2, pre-flight simulations were made to determine the acceleration due to aerodynamic forces in the spacecraft z-direction.

To estimate the acceleration due to aerodynamic forces in the spacecraft z-direction, a_z was determined using Equation 3-1 and the following data. The spacecraft was assumed to always have the spacecraft -z axis aligned with the velocity vector. Spacecraft velocity was estimated from a 24 hour orbit ($a=20180.3$ km $e=0.827$, $i=93.175$ deg, $w=320.037$ deg, $\Omega=143.817$ deg). The density was estimated using a constant density scale height atmosphere with the MGS project target periapsis density of 60 kg/km^3 and a scale height 7 km. The simulation used the following constants: spacecraft mass equal to 760 kg, reference area equal to 17.03 m^2 , and C_z equal to 2.0 . The results of the simulation are shown in Table 3-1.

Table 3-1: Aerodynamic Force Acceleration Simulation Results

Altitude (km)	Simulated Density (kg/km^3)	Aero Acceleration (m/s^2)
170	0.005	2.48×10^{-6}
140	1.3	6.45×10^{-4}
103	60	2.99×10^{-2}

3.1.2 Gravity Gradient Acceleration

The gravity gradient acceleration is due to the differences in the gravitational force on different parts of the spacecraft. The Equation 3-3 describes the gravity gradient acceleration experienced by the accelerometer instrument [10].

$$\Delta \ddot{\bar{R}} = -\mu \left[\frac{\bar{R}}{|\bar{R}|^3} - \frac{\bar{R}_{cm}}{|\bar{R}_{cm}|^3} \right] - \dot{\theta} \hat{e}_\theta \times (\dot{\theta} \hat{e}_\theta \times \Delta \bar{R}) \quad (3-3)$$

In Equation 3-3, μ is the gravitational constant for Mars, $\Delta \bar{R}$ is the distance between the center of mass of the spacecraft and the instrument, \bar{R}_{cm} is the distance from Mars to the center of mass of the spacecraft, \bar{R} is the distance from Mars to the instrument, and $\dot{\theta} \hat{e}_\theta$ is the angular velocity of the spacecraft in the orbit plane. \bar{R} expressed in this R, θ ,Z cylindrical coordinate system is

$$\bar{R} = (r_{cm} + \Delta r) \hat{e}_r + \sqrt{r_{cm}^2 + r_{cm}^2 \Delta \theta^2} \hat{e}_\theta + \sqrt{r_{cm}^2 + \Delta z^2} \hat{e}_z \quad (3-4)$$

where r_{cm} is the radial distance to the spacecraft center of mass, Δr is the radial distance from the spacecraft center of mass to the instrument, $\Delta \theta$ is the distance along the orbit from the spacecraft center of mass to the instrument, and Δz is the perpendicular distance off the orbit plane from the spacecraft center of mass to the instrument.

If Equation 3-4 is substituted into Equation 3-3, the gravity gradient acceleration at the position of the accelerometer instrument to 1st order is

$$\Delta \ddot{r} = \left(\frac{h^2}{r_{cm}^4} + \frac{2\mu}{r_{cm}^3} \right) \Delta r \quad \Delta \ddot{\theta} = 0 \quad \Delta \ddot{z} = \frac{h^2 \Delta z}{r_{cm}^4} \quad (3-5)$$

where h is the angular momentum of the orbit.

To determine the magnitude of the gravity gradient acceleration, sample values were substituted into Equation 3-5. The orbital elements described in Section 3.1.1 were used and the distance between the spacecraft center of mass and the accelerometer instrument was assumed to be 0.44 meters in the R-direction and 0.38 meters in the Z-direction. The results of the gravity gradient acceleration are shown in Table 3-2 for various altitudes.

Table 3-2: Gravity Gradient Acceleration Simulation Results

Altitude (km)	Gravity Gradient Acc (m/s ²)		
	R	θ	Z
170	$1.60 \cdot 10^{-6}$	0	$6.54 \cdot 10^{-7}$
140	$1.65 \cdot 10^{-6}$	0	$6.76 \cdot 10^{-7}$
103	$1.69 \cdot 10^{-6}$	0	$6.98 \cdot 10^{-7}$

If the spacecraft is always oriented with the spacecraft z-axis on the velocity vector (the θ direction in the cylindrical coordinate system), the simulation results in Table 3-2 demonstrate the gravity gradient will have no first order effect on the acceleration measured in the z-direction.

The spacecraft z-axis will not always remain aligned with the velocity vector, therefore, other orientations of the spacecraft must be considered to determine the maximum gravity gradient. The control system used for MGS limits the spacecraft to a 20 degree deviation of heading from the velocity vector during the aerobraking pass. Assuming the spacecraft is 20 degrees off the velocity vector towards the radial direction from the planet, the maximum gravity gradient acceleration measured by the spacecraft z-axis accelerometer is $5.5 \cdot 10^{-7} \text{ m/s}^2$. As shown in Table 3-1, the maximum gravity gradient is less than 1 percent of the aerodynamic acceleration below 140 km. However, the gravity gradient component is approximately 22 percent of the 170 km acceleration estimate.

Since the main focus of this investigation was to estimate and predict density values up to 30 km above the periapsis altitude, the gravity gradient was considered negligible. If higher altitudes are examined with the methods outlined in this paper, the gravity gradient term should be included in the development of the measured acceleration. The gravity gradient term can be included by using Equation 3-5 to find the gravity gradient acceleration in the R, θ , Z coordinate system and then transforming this acceleration into the spacecraft coordinates by determining the orientation of the spacecraft relative to the velocity vector.

3.1.3 Acceleration Due To Solar Pressure

The acceleration due to solar pressure is caused by solar radiation interacting with the surface of the satellite. The solar pressure is a function of the size of the spacecraft, the distance from the spacecraft to the sun and the orientation and reflecting properties of the spacecraft surface. Equation 3-6 was used to examine the magnitude of the acceleration due to solar pressure [11].

$$|\bar{a}_{solar}| = \frac{F_s}{mc} A(1 + q_r) \cos \theta_i \quad (3-6)$$

In Equation 3-6, F_s is solar constant, 590 W/m^2 at Mars, c is the speed of light, A is the cross-sectional area of the satellite in the direction of incoming radiation, m is the satellite mass, q_r is the reflectance factor which ranges from 0 to 1 (0 corresponds to photon absorption, i.e. no reflection, and 1 is perfect reflection) and θ_i is the incidence angle of the incoming radiation. To estimate the magnitude of the acceleration due to solar pressure, the properties for spacecraft mass and area from Section 3.1.1, a reflectance factor of 1, and an incidence angle of 0 degrees were substituted into Equation 3-6. Using these values, the acceleration due to solar pressure was determined to be $8.8 \times 10^{-8} \text{ m/s}^2$. When compared to the calculations of acceleration due to aerodynamic forces, the value for acceleration due to solar pressure was negligible and, therefore, omitted from the calculation of measured acceleration.

3.1.4 Bias Acceleration

As stated in Section 2.1, the accelerometer instrument measures the voltage necessary to keep a proof mass suspended inside a magnetic ring. The voltage reading necessary to keep the mass in balance during periods of no acceleration is known as the instrument bias. The acceleration reading corresponding to this instrument bias is the bias acceleration. The bias acceleration is a function of instrument properties and instrument

temperature. To determine the acceleration bias, the instrument must be continually checked and the surrounding temperature continuously monitored such that drift, i.e. change in the bias value as a function of time, can be determined.

For the MGS mission, bias was determined by monitoring the accelerometer instrument during periods before and after entering the atmosphere. The bias acceleration was then estimated over the entire pass by averaging the data from the pre- and post-atmospheric entry periods. The pre- and post-atmospheric periods were defined by instrument on and off times and an altitude limit of the atmosphere. For the MGS mission, the altitude limit was set by examining the acceleration profile and selecting an altitude well above the first indications of accelerations due to the atmosphere, typically 200 km.

3.1.5 Angular Motion Acceleration

The acceleration from the angular motion of the spacecraft is caused by the accelerometer instrument not being at the center of mass of the spacecraft. This acceleration can be estimated by the Equation 3-7 [12].

$$\bar{a}_{angular} = \bar{\omega} \times (\bar{\omega} \times \bar{r}) + \bar{\alpha} \times \bar{r} \quad (3-7)$$

The angular acceleration component is a function of the distance between the center of mass of the spacecraft and the instrument, \bar{r} , the angular rate of the spacecraft, $\bar{\omega}$, and the angular acceleration of the spacecraft, $\bar{\alpha}$.

For the MGS mission, angular rate was determined by on-board gyros and shown for a typical pass in Figure 3-1.

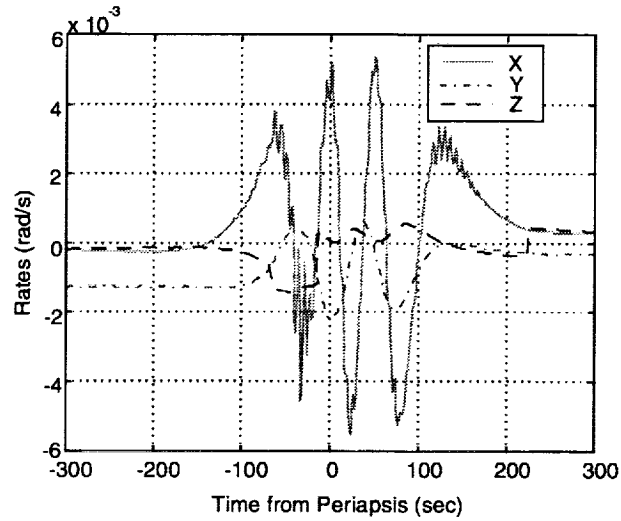


Figure 3-1: Typical spacecraft angular rates (Orbit 162)

Angular acceleration was not monitored by any instrument and was determined from the angular rates. The method used during MGS aerobraking was based on a running Chebyshev polynomial fit. In this method a series of five rate data points were fit with a 3rd order Chebyshev polynomial. By differentiating the polynomial and evaluating the derivative at the central point of the fit, the angular acceleration at that point was determined. The combination of five fit points with a 3rd order polynomial was selected because this combination was the fastest computationally and had good fitting qualities. The fit to the rate data contained errors on the order of 1% (1×10^{-5} rad/s errors on rate values of 1×10^{-3} rad/s). An example of the angular accelerations determined using this method and the rate data in Figure 3-1 is shown in Figure 3-2.

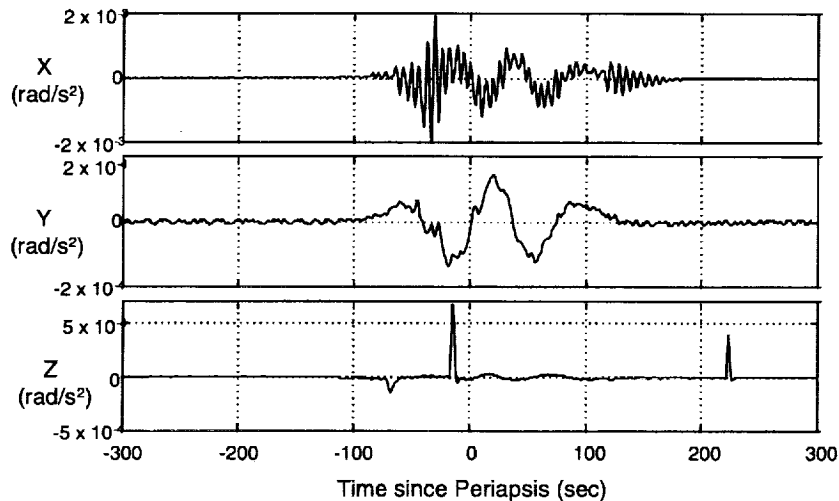


Figure 3-2: Typical x, y and z angular accelerations (Orbit 162)

By examining the angular acceleration data in Figure 3-2, several spacecraft activities can be observed. First, the spikes shown in the z-angular accelerations indicate times of control system thruster activity. Second, the vibration of the SAM can be observed by examining the x-angular accelerations.

The motion of the SAM, does cause the center of mass of the entire spacecraft to move in the body. The term compensating for this motion, i.e. the term describing the changing distance between the center of mass and the instrument, is neglected in Equation 3-7. This distance between the instrument and the center of mass was assumed constant in this investigation because the spacecraft center of mass moves very little due to panel motion. One degree of panel motion only causes approximately 0.1 cm of center of mass motion.

The magnitude of the acceleration due to angular motion was estimated using Equation 3-7, the distance between the accelerometer instrument and the spacecraft center of mass from Section 3.1.2, and the angular rate and angular acceleration in Figures 3-1 and 3-2. The maximum acceleration due to angular motion for this sample pass was approximately 0.0008 m/s^2 . When this estimation is compared to aerodynamic force acceleration estimations, the accelerations due to angular motion cannot be considered a negligible contributor to the measured acceleration equation.

3.1.6 Thruster Acceleration

The exact spacecraft reactions to thruster activity are very difficult to determine because the force of the thruster is a combination of several quantities that are difficult to model [13], such as, the effectiveness of the blow down phase, the temperature of the catalyst, and the interference of the thruster plume with the atmospheric flow [6].

The MGS spacecraft has 12 attitude control thrusters located in four pods off the lower corners of the spacecraft bus (Figure 2-1). In each pod, two nozzles point in the spacecraft negative -z direction and one in the roll direction (rotation about z). For the

MGS spacecraft, thruster activity is monitored by cumulative thruster duration which is recorded every 8 seconds. Changes in duration, shown as step functions in Figure 3-3, indicate thruster activity occurred during the 8 second interval before the duration change was recorded. Yaw, Pitch, and Roll thruster activity produce rotations about the x, y and z spacecraft axes respectively.

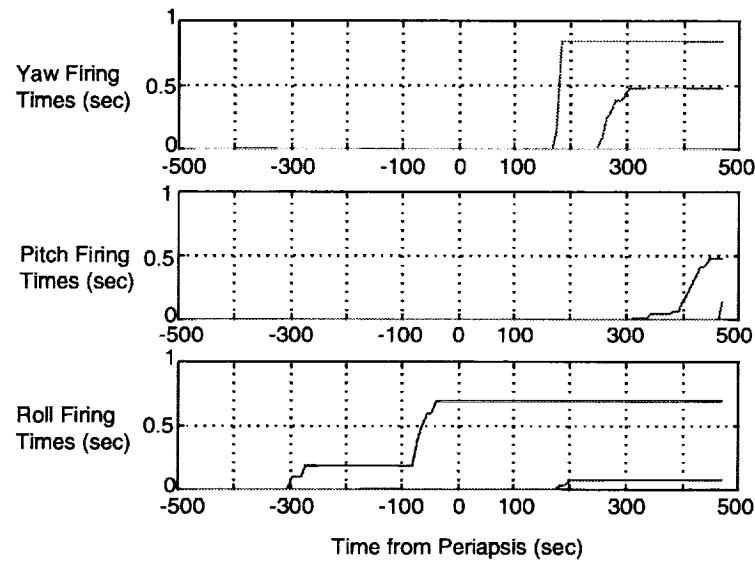


Figure 3-3: Typical thruster fire times (Orbit 16)

The acceleration due to thruster activity was compensated for by not using any data during yaw or pitch thruster activity to determine density. Since only the z-axis accelerometer was used to calculate density and roll thruster activity produces no acceleration in the z-axis, data during roll thruster activity was used to determine density. This assumption was verified by examining the z-axis acceleration data during roll thruster fires.

3.1.7 Vibration Acceleration

Figure 3-4 demonstrates a worst-case sample of the vibration signal recorded during aerobraking. This vibration was identified as the SAM panel because the frequency of the data was identical to frequencies discovered during “shake tests” en route to Mars. During these shake tests, the gimbal motor on the attachment point

between the bus and the SAM panel was activated in quick bursts to try to vibrate the panel.

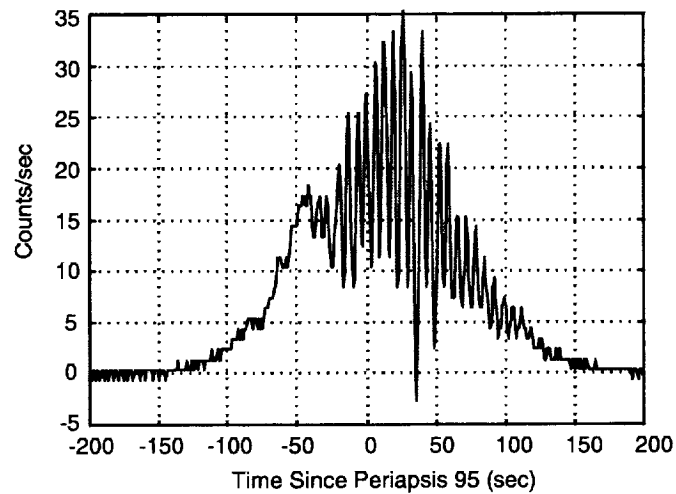


Figure 3-4: Acceleration data with large amplitude vibrations (Orbit 95)

Assuming that the SAM panel was vibrating during the pass, a model was created to estimate the effect of this vibration on the measured acceleration.

In the model, the SAM and the remaining parts of the spacecraft, the bus and the solar array on the +y spacecraft axis (BUS+SAP), were assumed to be two separate bodies. Aerodynamic forces on the two bodies were neglected to isolate the acceleration contribution of the panel vibration measured by the z-axis accelerometer. The two bodies were attached by a spring at the suspected SAM yoke crack line, as shown in Figure 3-5.

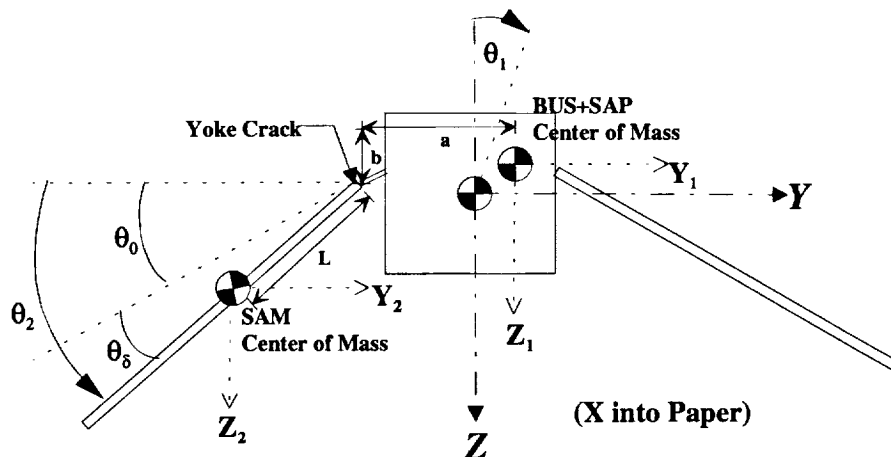


Figure 3-5: Diagram of 2-body 4 DOF model used to estimate moving panel acceleration

The spring is described by Equation 3-8, developed in shake tests during cruise [Personal Communication, W. Willcockson, 8/22/97]. In this equation, the spring torque, T , is a function of the deflection angle, θ_δ .

$$T = (1300 \frac{\text{in-lbs}}{\text{deg}}) * \theta_\delta^{1.3} \quad (3-8)$$

To construct the model, rotations about the spacecraft y and z axis and translations in the x-direction were neglected. The kinetic and potential energy of the two body, 6 degree of freedom (DOF) system was calculated and are shown in Equation 3-9.

$$\begin{aligned} T_{\text{system}} = & \frac{1}{2} m_1 (\dot{y}_1^2 + \dot{z}_1^2) + \frac{1}{2} I_{xx_{BUS+SAF}} \delta \dot{\theta}_1^2 + \frac{1}{2} m_2 (\dot{y}_2^2 + \dot{z}_2^2) \\ & + \frac{1}{2} I_{xx_{SAM(SAMcom)}} (\delta \dot{\theta}_1^2 - 2 \delta \dot{\theta}_1 \delta \dot{\theta}_\delta + \delta \dot{\theta}_\delta^2) \end{aligned} \quad (3-9)$$

$$V_{\text{system}} = \int M d\theta = \int (T_c \theta^{X_c}) d\theta = \frac{1}{X_c + 1} T_c \theta_\delta^{X_c + 1}$$

The z_2 and y_2 coordinates can be expressed in terms of the remaining coordinates using Equation 3-10, reducing the system to 4 DOF.

$$\begin{aligned} y_2 &= y_1 - a \cos \theta_1 - b \sin \theta_1 - L \cos(\theta_2 - \theta_1) \\ z_2 &= z_1 - a \sin \theta_1 + b \cos \theta_1 + L \sin(\theta_2 - \theta_1) \end{aligned} \quad (3-10)$$

When Equation 3-10 is substituted into Equation 3-9 and the Lagrangian is formed, the z_1 , y_1 , θ_1 coordinates were found to be cyclic. Using conservation of the conjugate momentum in z_1 , y_1 and θ_1 , and assuming no exterior forces and small angle approximations, the equations of motion for this system were developed and are shown in Equation 3-11.

$$\begin{aligned} (m_1 + m_2) \ddot{y}_1 + (-m_2 b - m_2 L \sin \theta_0) \delta \ddot{\theta}_1 + (m_2 L \sin \theta_0) \delta \ddot{\theta}_\delta &= 0 \\ (m_1 + m_2) \ddot{z}_1 + (-m_2 a - m_2 L \cos \theta_0) \delta \ddot{\theta}_1 + (m_2 L \cos \theta_0) \delta \ddot{\theta}_\delta &= 0 \\ \ddot{z}_1 (-m_2 a - m_2 L \cos \theta_0) + \ddot{y}_1 (-m_2 b - m_2 L \sin \theta_0) \\ + \delta \ddot{\theta}_\delta (-m_2 a L \cos \theta_0 - m_2 L^2 - m_2 b L \sin \theta_0 - I_{xx_{SAM(SAMcom)}}) \\ + \delta \ddot{\theta}_1 (m_2 a^2 + 2 m_2 a L \cos \theta_0 + m_2 L^2 + m_2 b^2 + 2 m_2 b L \sin \theta_0 + I_{xx_{BUS+SAF}} + I_{xx_{SAM(SAMcom)}}) &= 0 \end{aligned} \quad (3-11)$$

In this problem $\ddot{\theta}_1$ is the angular acceleration in the spacecraft x-direction, which was determined from onboard gyro data as shown in Section 3.1.5. Equation 3-11 is solved for \ddot{z}_1 , the acceleration of the BUS+SAP center of mass due to the motion of the SAM panel. A complete derivation of the system is shown in Appendix B.

An important note is that by assuming the BUS+SAP and SAM are separate masses, the gyros located on the BUS are only monitoring the BUS+SAP body. Therefore, to identify the acceleration from spacecraft angular motion described in Section 3.1.5, the center of mass of the BUS+SAP body must be used instead of the entire spacecraft center of mass to determine the distance, r , in the angular motion equation, Equation 3-7. This distance, r , is assumed constant because the BUS+SAP body is considered rigid.

3.2 Development of the Spacecraft Velocity Term

The satellite velocity term is the magnitude of the spacecraft velocity with respect to the atmosphere. To estimate the velocity with respect to the atmosphere, the velocity of the Martian atmosphere was assumed negligible when compared to the orbital velocity. To determine orbital velocity, 2-body equations were used. Kepler's equation was solved by successive substitution using osculating elements (a, e, i, w, Ω, τ) at periapsis. The orbital velocity term was then the magnitude of the areocentric velocity vector which was determined with areocentric position using Equations 3-12.

$$\begin{aligned} \bar{R}_{cm} = & r_{cm}(\cos(w + f)\cos\Omega - \sin(w + f)\sin\Omega\cos i)\hat{e}_x \\ & r_{cm}(\cos(w + f)\sin\Omega + \sin(w + f)\cos\Omega\cos i)\hat{e}_y \\ & r_{cm}(\sin(w + f)\sin i)\hat{e}_z \end{aligned} \quad (3-12)$$

$$\begin{aligned} \dot{\bar{R}}_{cm} = & \dot{r}_{cm}\hat{e}_r + r_{cm}\dot{f}(-\sin(w + f)\cos\Omega - \cos(w + f)\sin\Omega\cos i)\hat{e}_x \\ & r_{cm}\dot{f}(-\sin(w + f)\sin\Omega + \cos(w + f)\cos\Omega\cos i)\hat{e}_y \\ & r_{cm}\dot{f}(\cos(w + f)\sin i)\hat{e}_z \end{aligned}$$

In Equation 3-12, r_{cm} is the radial position, w is the argument of periapsis, f is the true anomaly, Ω is the longitude of the ascending node, and i is the inclination.

Since periapsis osculating elements only represent the orbit at periapsis, using 2-body equations away from periapsis resulted in errors in position and velocity. To estimate these errors, areocentric position was used as a measure of the effectiveness of the 2-body equation procedure. A simulation was developed which determined the error between a known orbit and an orbit generated from the 2-body equation using periapsis osculating elements [Personal Communication, C. Acton, 9/6/97]. First, the exact position and velocity for several times near periapsis of a sample orbit were generated. Next, a set of osculating elements were generated at periapsis for the same orbit. Finally, the position developed from these osculating elements was compared to the exact position and the error in range was calculated. The results of the study for pre-mission sample orbit #34 ["MGS Orbit Propagation and Timing Geometry File v001: optg_i_970912-980219_ab0422bl", JPL May 8, 1997. Available from MGS NAV Team] are shown in Table 3-3.

Table 3-3: Results of Range Error Study Between Exact Ephemeris and Ephemeris Generated From Osculating Elements at Periapsis

Time From Periapsis (sec)	Approx. Areocentric Altitude (km)	Range Error [Exact-Kepler] (km)
240	186.2	0.218
200	167.2	0.175
150	136.4	0.130
100	118.4	0.081
50	107.5	0.027
0	103.9	0.000

In Section 5, the range error is converted to equivalent density error so that a comparison to other process errors can be made.

3.3 Development of the Ballistic Coefficient Term

The ballistic coefficient is composed of the force coefficient, the spacecraft reference area and the mass of the spacecraft. The spacecraft mass was assumed constant

during an aerobraking pass because fuel usage by control system thrusters was small ($\ll 1\text{ kg}$) compared to the total spacecraft mass (approx. 760 kg). The spacecraft reference area was calculated as the cross-sectional area seen by the flow when the spacecraft is in the aerobraking configuration with the spacecraft -z axis aligned with the velocity vector. The force coefficient was determined by developing an aerodynamic database of force coefficients and interpolating the value of the coefficient by knowing the spacecraft orientation, and by estimating the panel deflection angle and the density of the atmosphere. The following sections describe the development of the aerodynamic database and the use of the database to determine force coefficients.

3.3.1 Development of the Aerodynamic Database

The calculations performed to construct the aerodynamic database are described by Wilmoth [7]. Force coefficients (C_x , C_y , C_z) and moment coefficients (C_{Mx} , C_{My} , C_{Mz}) were calculated for the MGS spacecraft using a DSMC code (Direct Simulation Monte Carlo) and assuming an atmosphere to be 95.37% carbon dioxide and 4.63% molecular nitrogen, an MGS spacecraft surface temperature of 300 K, diffuse scattering, and full energy and momentum accommodation. These calculations covered SAM deflections of 0, 10, and 20 degrees, densities of $\rho=0.1, 12, 72$, and 120 kg/km^3 and wind orientations, U_y and U_x equal to -15, 0 and 15 degrees. Orientation of the wind for this investigation was described by U_x and U_y , the direction sines of the relative wind in the spacecraft coordinate system, as shown in Figure 3-6. For this analysis, the reference area of the spacecraft was assumed to be 17.03 m^2 and the reference length for all moment coefficients was assumed to be 8.73 m.

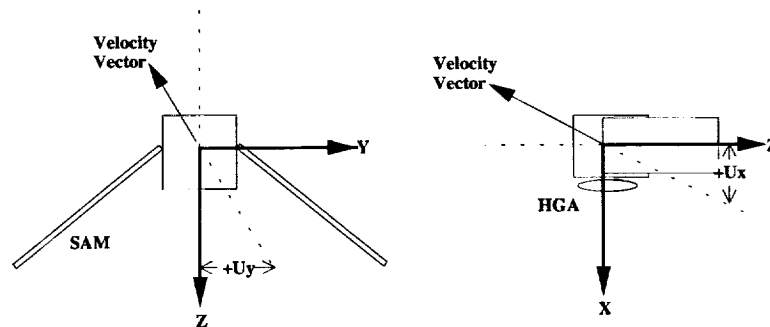


Figure 3-6: U_x and U_y coordinate definition

Figures 3-7 and 3-8 summarize the results from the aerodynamic database generated for aerobraking operations. Figure 3-7 demonstrates how the force coefficient varies with density and panel deflection. Note any density value below 0.1 kg/km^3 was considered free molecular flow (corresponding to Knudsen numbers greater than 1).

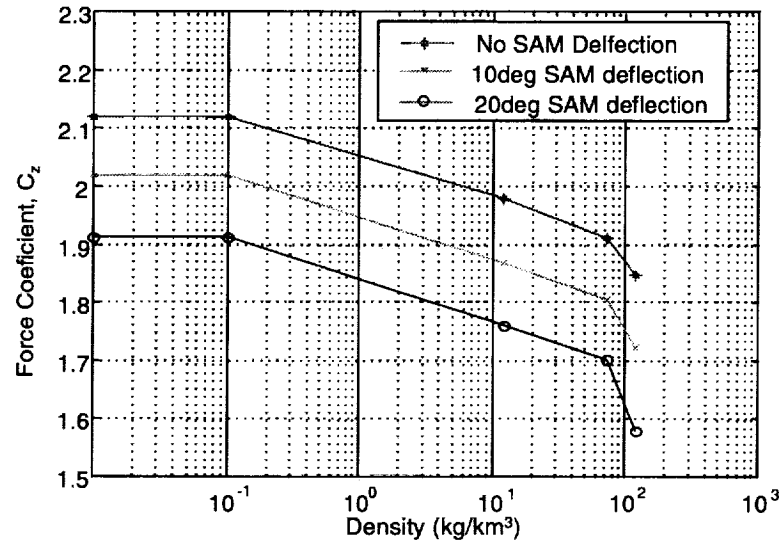


Figure 3-7: Force coefficient in spacecraft z-direction, C_z , vs. density level for all panel deflections

Each 10 degrees of panel deflection reduces C_z by approximately 5 percent, due primarily to reduction in frontal area [6]. Note that change in C_z is linear with change in panel deflection.

Figure 3-8, demonstrates how the C_z force coefficient varies with wind orientation. The left side of the figure shows the contour generated with no-deflection and a density of 12 kg/km^3 . The right side of Figure 3-8, demonstrates the contour generated with a density of 12 kg/km^3 and 10 degrees of SAM panel deflection.

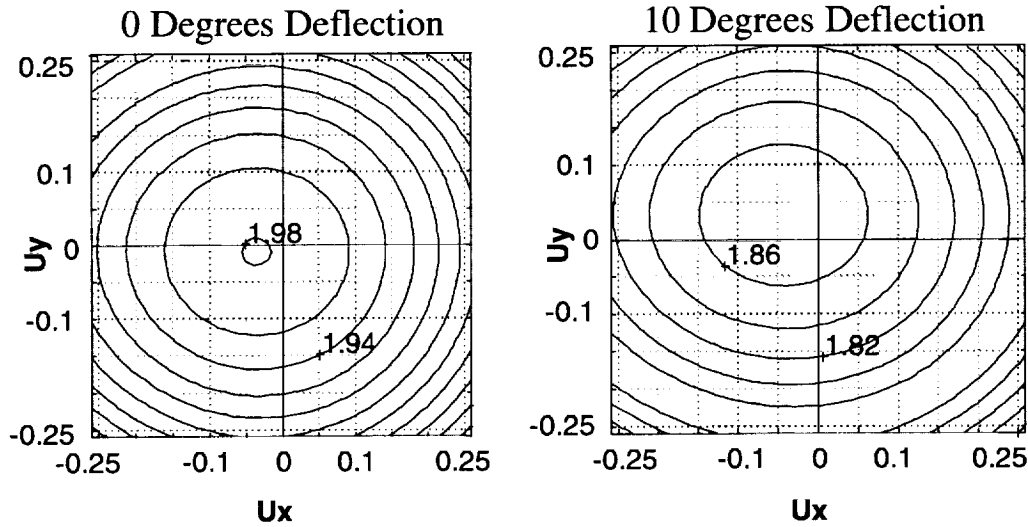


Figure 3-8: C_z tables for free molecular densities (0 degree SAM Deflection and 10 degree SAM Deflection)

With zero panel deflection, C_z is nearly symmetric about U_y and offset approximately 2 degrees from U_x equal to zero. This is due to the geometric symmetry about the spacecraft z-x plane and the asymmetry caused by the high gain antenna about the z-y plane. With 10 degrees panel deflection, the peak C_z value decreases and shifts approximately 2.8 degrees toward positive U_y . This decrease is due to area change from panel deflection. The shift demonstrates that during 10 degree panel deflections, the largest area occurs when the spacecraft is rotated 2.8 degrees about the spacecraft negative x-axis.

Important to the analysis of spacecraft dynamics were DSMC simulations done on the SAM disregarding the rest of the spacecraft. Using the same assumptions mentioned previously, analyses were made to calculate force and moment coefficients of the panel for all wind orientations, all deflection angles and all density ranges used in the analysis of the entire spacecraft. The entire database of force and moment coefficient values used during MGS aerobraking for the entire spacecraft and the SAM panel without the remaining parts of the spacecraft is shown in Appendix C.

3.3.2 Determining Force Coefficients

Force coefficients were determined by interpolation of the aerodynamic database. Inputs to this interpolation were the orientation of the relative wind, density, and panel position. Density and panel position were determined by the iterative scheme discussed in Section 4.4.3. The orientation of the incoming wind was determined by combining the orbital velocity and the atmospheric winds in the spacecraft centered system.

To determine the orbital velocity in the spacecraft system, quaternions produced onboard the spacecraft, shown in Figure 3-9, were used to form a direction cosine matrix, (DCM) using Equation 3-13 [14]. Using the DCM, the orbital velocity in the planet centered system (Section 3.2) can be transformed into the spacecraft centered system.

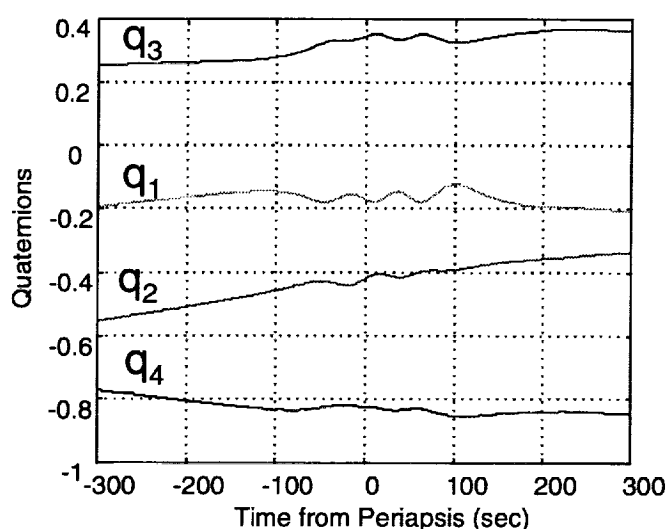


Figure 3-9: Typical quaternions (Orbit 162)

$$\begin{bmatrix} x \\ y \\ z \end{bmatrix}_{\text{SpacecraftCentered}} = [DCM] * \begin{bmatrix} X \\ Y \\ Z \end{bmatrix}_{\text{PlanetCentered}} \quad (3-13)$$

$$[DCM] = \begin{bmatrix} q_1^2 - q_2^2 - q_3^2 + q_4^2 & 2(q_1q_2 + q_3q_4) & 2(q_1q_3 - q_2q_4) \\ 2(q_1q_2 - q_3q_4) & -q_1^2 + q_2^2 - q_3^2 + q_4^2 & 2(q_2q_3 + q_1q_4) \\ 2(q_1q_3 + q_2q_4) & 2(q_2q_3 - q_1q_4) & -q_1^2 - q_2^2 + q_3^2 + q_4^2 \end{bmatrix}$$

The atmospheric wind is modeled as the wind due to rigid rotation of the atmosphere. The velocity of the atmospheric wind was calculated using Equation 3-14, the rotation rate of the planet, $\bar{\dot{L}}$, and the spacecraft distance from the planet, \bar{R}_{cm} .

$$\bar{v}_{WIND} = \bar{\dot{L}} \times \bar{R}_{cm} \quad (3-14)$$

This wind was then transformed with the same DCM created above into the spacecraft centered system.

A typical ‘orientation of the relative wind’ diagram for an entire pass is shown in Figure 3-10, where each dot represents 50 seconds of time from periapsis.

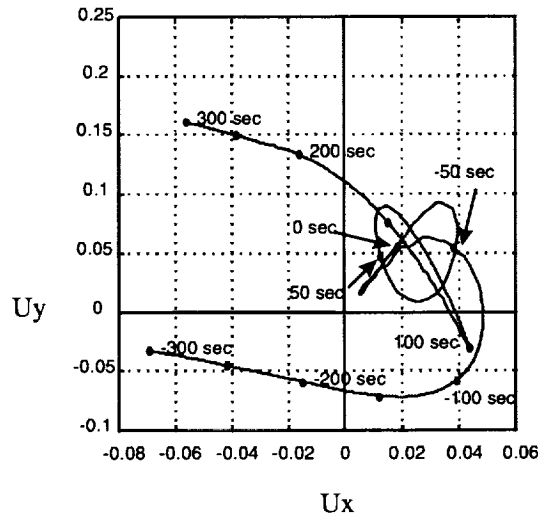


Figure 3-10: Typical Ux and Uy diagram (Orbit 162)

The interpolation of the aerodynamic database for one moment or force coefficient value was a 4-D interpolation process accomplished in three steps. First, all the density and panel deflection permutations were interpolated for the Ux and Uy orientation of the wind using 2-D cubic spline interpolation. Second, the results of the first step were interpolated for the density value using a logarithmic-linear interpolation (i.e. the logarithm of the density values is used instead of the density values in a linear interpolation). Third, the results of the second step were interpolated for the panel position value using a standard linear interpolation.

4. Operational Data Reduction Procedure

Section 4 will discuss the procedures and studies performed to create the operational data reduction procedure used to determine densities from accelerometer data during the 1st phase of aerobraking at Mars. First the operational scenario including mission constraints and the operational accelerometer instrument is discussed. The amount of accelerometer data necessary to perform the operational responsibilities is determined. Next, the data reduction procedure is described using Section 3 methods modified for the MGS operational scenario. Finally, several extra products of the data reduction procedure as well as prediction methods are discussed.

4.1 Operational Constraints

To be effective during aerobraking operations, methods used to calculate density have to be computed quickly and accurately over a range of altitudes. According to MGS project constraints, all accelerometer data analysis must be completed within 2 hours of receiving data. Since most of this time should be devoted to the analysis of density trends, the procedure to calculate density for the entire orbit should be completed in one quarter of the allowable time or 30 minutes. To fully understand the atmosphere, the calculation of density must be accurate over a large range of altitudes. The methods were designed to be accurate over an altitude range of 30 km above periapsis. This altitude range was chosen to allow density to be calculated over approximately 4 scale heights.

The data provided to perform the accelerometer data reduction process included all values shown in Table 4-1. These data types were provided every aerobraking pass by telemetry. Note accelerometer data rate for the first 15 aerobraking orbits was 10 samples every 8 seconds. This data rate was increased to 1 sample every 0.1 seconds when aerobraking resumed after the investigation of the panel over-extension.

Table 4-1: Telemetry Data Types And Rates For Operations

Telemetry Name	Units	Data Rate
Accelerometer (Z only)	counts (0.332mm/s)	1 sample / 0.1 sec
Angular Rates (X, Y, Z)	rad/s	All 3 / 1 sec
Quaternions (1,2,3,4)	--	All 4 / 1 sec
Thruster Fire Times (12 thrusters)	sec	All 12 / 8 sec
IMU temperatures (Outside, Inside and voltage)	degC / volts	All 3 / 4 sec
Solar Panel Temperatures (8 thermistors)	degC	All 8 / 4 sec
Sun Sensor Panel Deflection	degrees	1 sample / 8 sec

Data from the NAV Team, not shown in table, included osculating orbital elements at periapsis. The orbital elements were provided twice an orbit, a set of prediction elements before the aerobraking pass and a set of reconstructed elements after a proper scale height was produced by the ACC Team. All data listed in Table 4-1 and orbital elements, satisfy the requirements necessary to perform the methods outlined in Section 3.

4.2 Operational Accelerometer Instrument

The accelerometers on the MGS spacecraft are the Sundstrand QA1200-AA08 model Q-Flex accelerometer. The four accelerometers (X,Y,Z and skew) are contained in the IMU (Inertial Measurement Unit) package located on the nadir deck, see Figure 2-1. The accelerometers measure the change in velocity of the spacecraft in each of the principle directions over 0.1 second intervals. The acceleration data is recorded in instrument counts, quantized velocity increments with a 0.332 mm/s per count resolution. The accelerometer accumulates the change in velocity every 0.1 seconds so that the remainder of the change in velocity after quantization is added to the next 0.1 second.

Monitoring the accelerometers during cruise and throughout the 1st phase of aerobraking has demonstrated the quality of the instrument. First, the 0.0332 mm/s² acceleration resolution is very sensitive, 38 times better than the resolution of the accelerometer used on the Viking entry probes [15]. Second, the instrument is very

stable. During the travel to Mars, two separate measurements taken before trajectory correction maneuvers (TCM), 8 months apart, resulted in a bias change of only 2% (TCM-1 bias=5.62 +/- 0.12 counts/0.1 sec, TCM-2 bias=5.70 +/- 0.05 counts/0.1 sec). During aerobraking, the bias remained at 5.66 +/- 0.005 counts/0.1 sec, varying only 0.1 percent over the entire 201 passes (192 days) of the 1st phase of aerobraking. This bias stability is due to the temperature control of the instrument. The temperature of the IMU box is monitored by two temperature sensors, one inside the box and one on the box housing, and controlled by a single heater. A sample plot of the output of the two sensors and the voltage to the heater is shown in Figure 4-1.

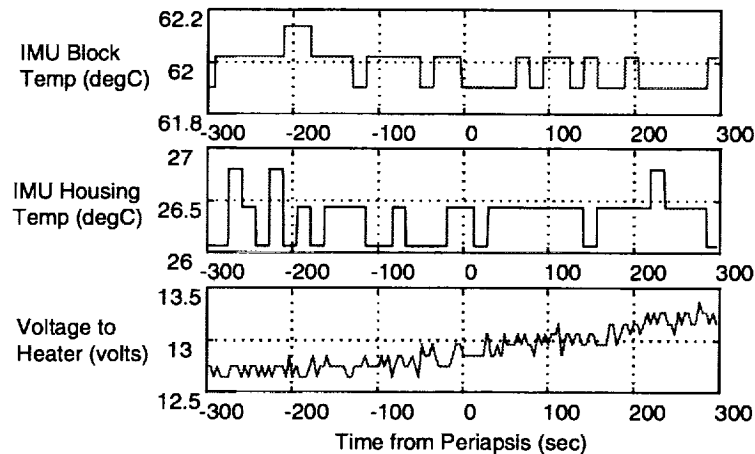


Figure 4-1: Typical IMU temperatures and voltage to IMU heater (Orbit 162)

Examining Figure 4-1, the quantum of temperature measurement inside the IMU is 0.117 °C and the highest temperature variation was 2 quanta over a period of 4 seconds. To calculate the effect of this temperature variation on accelerometer measurements, the accelerometer manufacturer's estimate of 0.3 counts of acceleration change per °C of temperature change was used ["Sundstrand Data Control's Q-Flex Servo Accelerometers: QA-1200 and QA-1300 Data Sheet.", 1984. Available from The Sundstrand Data Control Corporation]. Therefore, a 2 quanta temperature variation over 4 seconds resulted in an acceleration change of $5.8 \times 10^{-6} \text{ m/s}^2$. When compared to the acceleration values of Section 3.1.1, the value of acceleration due to temperature change was negligible for altitudes within 30 km of periapsis. By further examining Figure 4-1 above, the

temperature did not exhibit any increase or decrease that would indicate atmospheric heating was affecting the accelerometers inside the IMU.

4.3 Quantity of Accelerometer Data Necessary to Perform Operations

To determine the quantity of accelerometer data necessary to complete all operational responsibilities, a simulation was developed to test the amount of accelerometer data needed to reproduce a known atmospheric trend. The simulation examined several different amounts of accelerometer data by first creating a atmosphere with a known density trend, and then simulating the spacecraft with an accelerometer instrument moving through that atmosphere. If the quantity of data being examined was sufficient, the results from the model should reproduce the known atmosphere.

To set up the simulation the following parameters and assumptions were used. To model the spacecraft motion, a 24 hour orbit ($a=20180.3$ e=0.827, $i=93.175$ deg, $w=320.037$ deg, $\Omega=143.817$ deg) was used. To model the accelerometer instrument, Equation 3-1 was solved for the acceleration, a_z , and then this acceleration was quantized and accumulated as described in Section 4.2. The coefficient of drag, spacecraft mass and spacecraft cross-sectional area were all assumed to be constant ($C_D=2$, mass=760 kg, $A=17$ m²). To model the atmosphere, a linear temperature model was used such that the density at any altitude was described by Equation 4-1 [Wilkerson, B., "Upper Atmospheric Modeling for Mars Global Surveyor Aerobraking Using Least Squared Processes," Graduate Research Paper for George Washington University, 1998. Available from author].

$$\ln \rho = \ln \rho_0 - \left(1 + \frac{g}{RT_1}\right) \ln \left(1 + \frac{T_1}{T_0}(z - z_0)\right) \quad (4-1)$$

In Equation 4-1, ρ is the density, ρ_0 is the base density, R is the universal gas constant (8.314 J/K*mole) divided by the mean molecular weight of the atmosphere (42.91 g/mole), T_1 is the temperature gradient, T_0 is the base temperature, g is the acceleration of

gravity on Mars (3.4755 m/s^2), z is the altitude, and z_0 is the base altitude. For this simulation, the following values were assumed: $\rho_0=60 \text{ kg/km}^3$, $T_1 = 2.862 \text{ K/km}$, $T_0=131.2 \text{ K}$, $z_0=103 \text{ km}$.

The simulation investigated three data rates including: one 0.1 second measurement every second, ten 0.1 second measurements every 8 seconds, and ten 0.1 second measurements every second. For the second case, the 10 measurements were contiguous and cover an entire second. The third case represented the “full potential data rate”, or a measurement every 0.1 seconds during the drag pass. All the data rates were averaged with a 40 second running mean. The results are shown in the three plots in Figure 4-2.

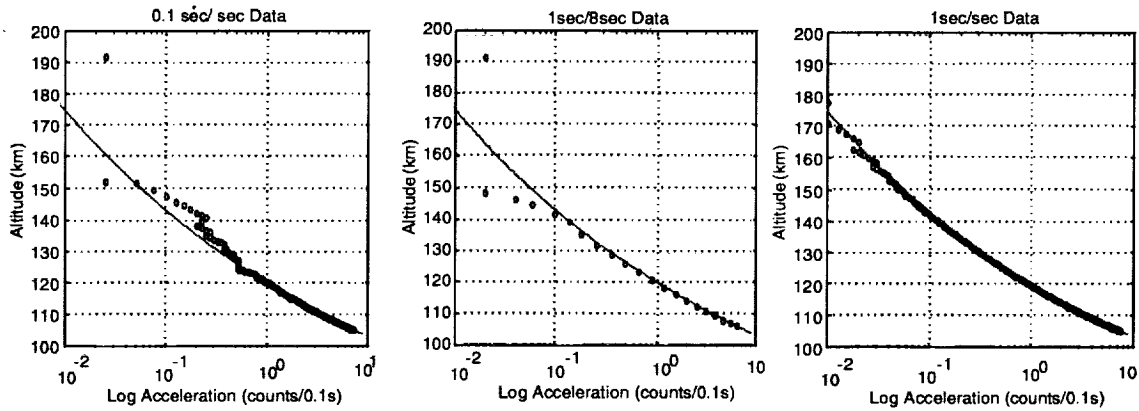


Figure 4-2: Results of Accelerometer Data Rate Simulation

In Figure 4-2, the line represents the a priori density model converted into acceleration and the circles represent the output from the simulation.

A very important feature of this study was that a change in the start time of the simulation produced different results. Since it is unknown when the start of the atmosphere would occur relative to the measurements that were sampled, many different density profiles were possible. Case 1 has 100 possible density profiles, case 2 has 80 possible density profiles, and case 3 has 10 possible density profiles. Each profile was achieved by changing the start time of the simulation by 0.1 seconds. The results of the three cases with all possible outcomes is shown in Figure 4-3.

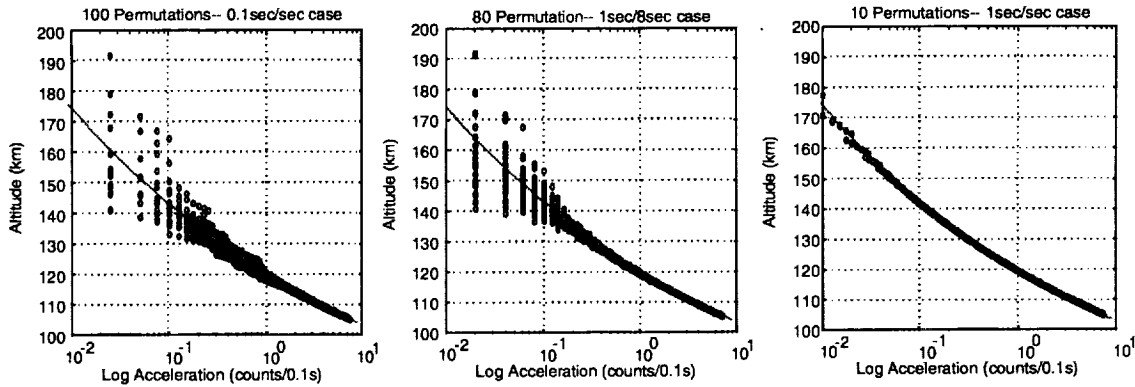


Figure 4-3: Results of accelerometer data rate simulation considering all possible outcomes

Using Figure 4-3, the effectiveness of each case was determined by considering the errors of all possible outcomes from the known atmosphere. The error of each point was calculated by subtracting the known acceleration from the model acceleration and then dividing by the known acceleration. Since the effectiveness of the data rates varies with altitude, several different altitude ranges were inspected: 110 - 120 km, 120 - 130 km, 130 - 140 km, 140-150 km, 150-160 km, and 160-170 km. In each of these altitude ranges, the standard deviation of all the errors in the altitude range were calculated and shown in Table 4-2.

Table 4-2: Results From Reliability of Accelerometer Data Simulation

Altitude Range (km)	Model Drag Accel Range (counts/0.1sec)	Case 1 StdDev (%) (0.1sec of data/sec)	Case 2 StdDev(%) (1sec of data/8sec)	Case 3 StdDev(%) (1sec of data/sec)
110-120	3.60 → 1.00	5.12	1.57	0.89
120-130	1.00 → 0.34	14.60	4.03	0.44
130-140	0.34 → 0.13	28.60	13.56	0.79
140-150	0.13 → 0.06	44.63	36.22	1.85
150-160	0.06 → 0.03	76.21	49.97	4.37
160-170	0.03 → 0.01	98.03	70.13	6.84

If the standard deviation limit of an accurate analysis is set at 5%, Table 4-1 shows that case 1 can only be used over the 17 km range between periapsis at 103 km and 120 km. This corresponds to acceleration values greater than 1.0 counts/0.1sec. Case 2 extends this range to 130 km corresponding to acceleration values greater than 0.34 counts/0.1sec. Case 3 can be used up to 160 km or acceleration values greater than 0.03

counts/0.1sec. Since case 2 and case 3 were accurate over an altitude range of 30 km above periapsis, both were used during MGS operations.

4.4 Operational Data Reduction Process

The accelerometer operational data reduction process was designed to determine density during the entire aerobraking pass by using inputs from the MGS spacecraft and the MGS NAV Team. The process is broken down into 4 steps: calculate orbital parameters, remove non-aero accelerations, the iterative density process and data averaging. The diagram showing the relationships of these steps is given in Figure 4-4.

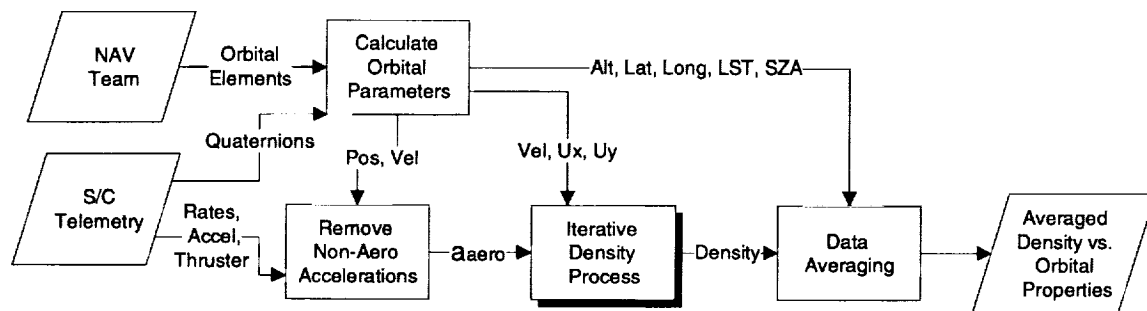
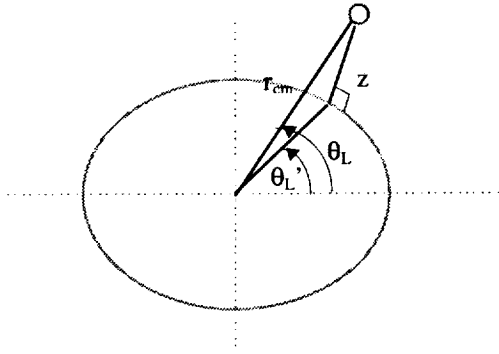


Figure 4-4: Data reduction process flow chart

As stated in Section 4.1, to function effectively in aerobraking operations, the data reduction procedure was originally allocated 30 minutes to complete. The average time from initial input of data to a final output of density was approximately 7 minutes. This time was for 16 minutes of data (approximately 9600 acceleration points) using a 200 MHz Pentium processor with 32 MB of memory.

4.4.1 Calculate Orbital Parameters

To develop atmospheric trends, density measurements were compared to various orbital parameters such as areodetic latitude, areodetic altitude, longitude, local solar time (LST) and solar zenith angle (SZA). These parameters were determined from the areocentric position vector and velocity vector, Mars planetary physical data shown in Appendix D, the position of the Sun in the Mars centered system, and the following formulas in Equation 4-2.



$$\tan \theta_L = \frac{\tan \theta_L'}{(1 - f_m)^2}$$

$$z = r_{cm} - \frac{a(1 - f_m)}{\sqrt{1 - f_m(2 - f_m)\cos^2 \theta'}}$$

$$SZA = \cos^{-1}(\sin \delta_{SUN} * \sin \delta_{SC} + \cos \delta_{SUN} * \cos \delta_{SC} * \cos(\alpha_{SC} - \alpha_{SC}))$$

$$LST = (\alpha_{SC} - \alpha_{SUN}) * \frac{24}{\dot{L}}$$

Equation 4-2: Equations for calculating orbital parameters

In Equation 4-2, r_{cm} is the radial distance of the spacecraft, z is areodetic altitude, a is the planet equatorial radius, f_m is the planet flattening, θ_L is the areocentric latitude, θ_L' is the areodetic latitude, α_{sun} is the right ascension of the sun in the Mars equatorial system, α_{sc} is the right ascension of the spacecraft in the Mars equatorial system, δ_{sun} is the declination of the sun in the Mars equatorial system, δ_{sc} is the declination of the spacecraft in the Mars equatorial system and \dot{L} is the rotation rate of Mars. Areocentric latitude was calculated by Napier's Rule using argument of periapsis, true anomaly, and inclination.

The 'calculate orbital parameters' process also determined the orientation of the wind for the entire pass. The procedure described in Section 3.3.2 was used to calculate the U_x and U_y parameters given the areocentric position vectors and areocentric velocity vectors, and the quaternions from the spacecraft telemetry.

4.4.2 Remove Non-Aero Accelerations

The 'remove non-aero accelerations' process was divided into three steps. First, the acceleration due to angular motion and SAM vibration were determined using the procedures described in Section 3.1.5 and Section 3.1.7 and removed from the measured acceleration. The vibration acceleration procedure was not used during the 1st phase of aerobraking due to the late development of this procedure, but is mentioned here to show its correct position in the overall data reduction process. Second, the thruster acceleration

procedure was applied according to Section 3.1.6, by removing all accelerometer data inside the 8 second interval during yaw and pitch thruster activity. Third, the bias acceleration was calculated as described in Section 3.1.4.

Due to the stability of the instrument and the unchanging temperature conditions of the IMU, the bias drift equation developed to describe a time varying bias over the entire aerobraking pass was reduced to just a constant term. The bias acceleration is then removed from the measured acceleration leaving the estimate for the acceleration due to aerodynamic forces. A typical plot of the bias calculation is shown in Figure 4-5.

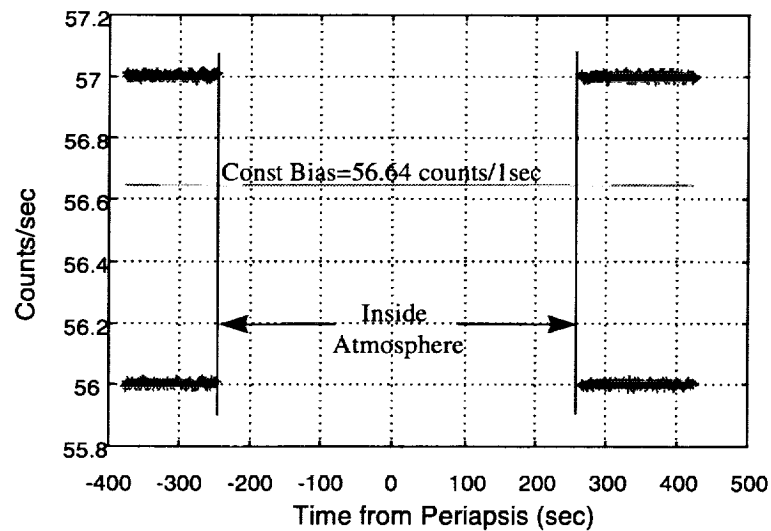


Figure 4-5: Typical accelerometer instrument bias calculation

4.4.3 Iterative Density Process

Density was determined through a double-loop iterative process which estimates force coefficient and panel position to calculate density. A diagram of the process is shown in Figure 4-6.

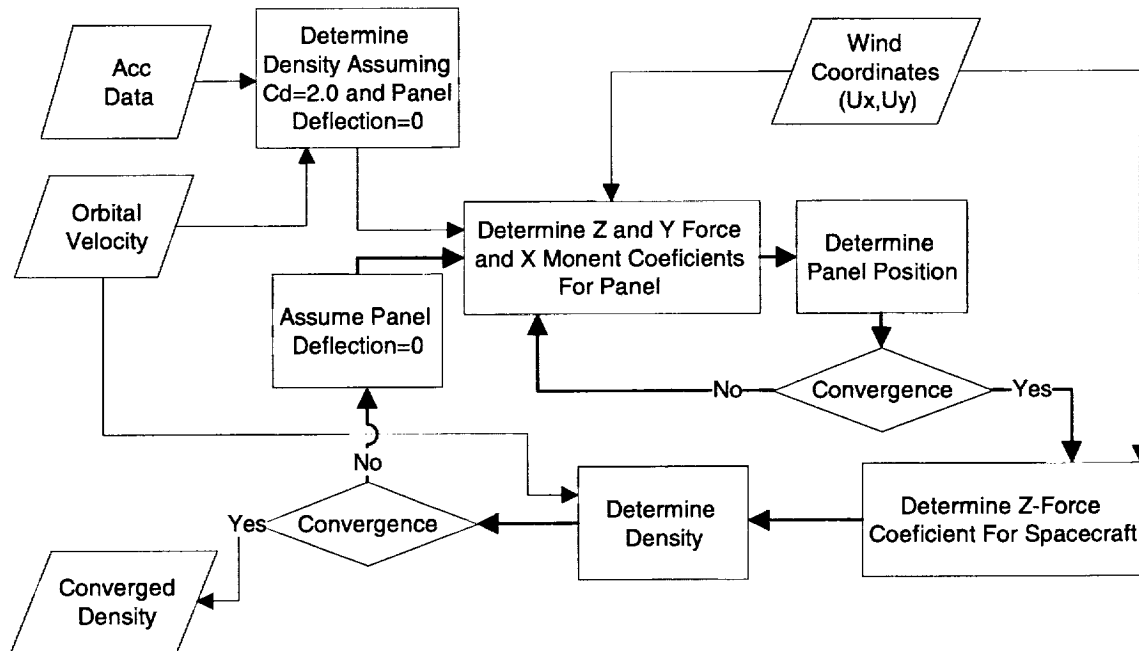


Figure 4-6: Development of density flow chart

As shown in Figure 4-6, aerodynamic acceleration was used to calculate the first density estimate assuming no deflection of the SAM panel and a force coefficient of 2.0. Next U_x and U_y data, the density, and panel deflection equal to zero were used to interpolate force and moment coefficients at every point during the pass for the SAM panel using methods outlined in Section 3.2.2. Using the interpolation data and physical information about the SAM, panel deflections were estimated for the entire pass.

Panel deflection was determined by, first, using the y-force coefficient, C_y , the z-force coefficient, C_z , and the density to calculate the magnitude of the force perpendicular to the panel. Next, the moment coefficient about x, C_{Mx} , was used to determine the moment on the panel. The center of pressure on the panel was determined by comparing the moment on the panel to the force perpendicular to the panel. Next, the distance from the center of pressure to the crack was multiplied by the normal force to determine the moment about the crack. Finally, using Equation 3-7, the deflection of the panel was determined. The entire process was iterated, using the panel deflection estimation to determine improved force and moment coefficients for the panel, until the panel position profile converged to less than 0.01 degrees from the previous estimation.

The resulting panel deflection, the density, and the wind orientation were used to determine of the force coefficient in the spacecraft z-direction for the entire spacecraft. Using the improved z-direction force coefficient for the spacecraft, the density was improved. This process was repeated until each density point converged to less than 0.01 kg/km³ from the previous density estimation.

Through this double iteration process, estimates of panel deflection and force coefficient over the entire pass were determined. Sample plots of these products are shown in Figure 4-7.

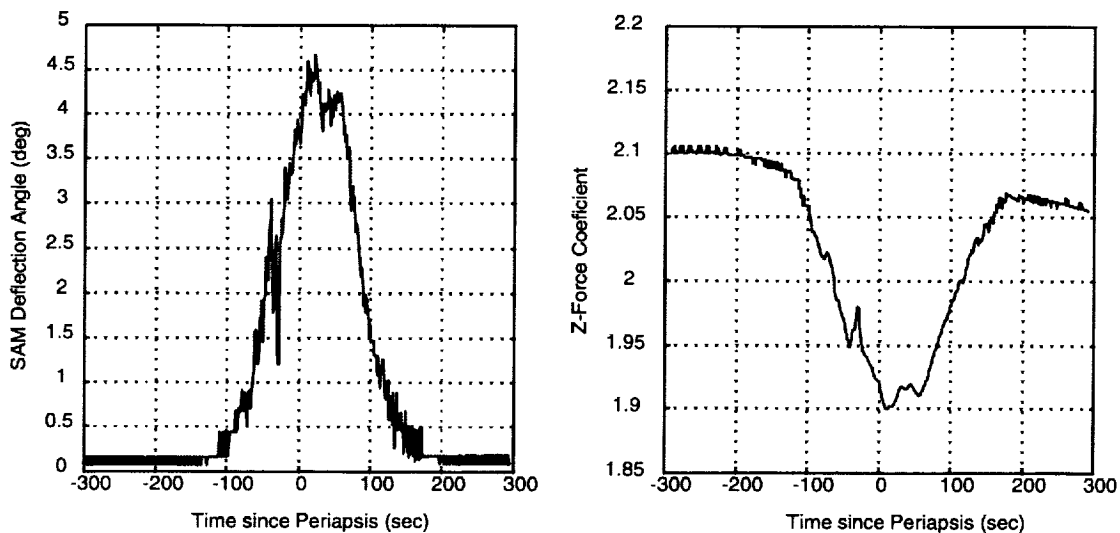


Figure 4-7: Typical z-force coefficient and panel deflection from Orbit 162

4.4.4 Data Averaging

The data averaging process used various averaging techniques to emphasize different sections of the aerobraking pass and also to reduce the effect of panel vibration on the accelerometer data. A six second running mean was used to identify density variations in low-altitude, localized sections of the pass and is shown in Figure 4-8 in comparison to the unaveraged (raw) density data. Also shown in this figure is the 40 second running mean which was used to analyze large sections of the pass by filtering out atmospheric waves, spacecraft-induced effects and instrument noise. Another averaging

technique used was a 67 point running mean or 6.7 second running mean. This averaging technique attempted to remove the 6.7 second period vibration signal by averaging over the vibration period. The 67 point technique is shown in comparison to the raw density data in Figure 4-8. Note the curves were each displaced by 5 kg/km³ for clarity.

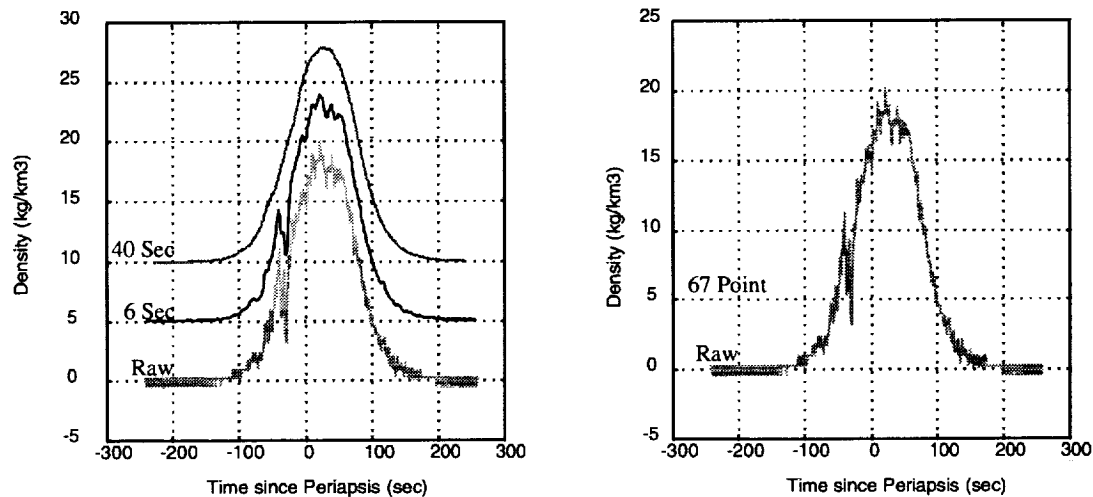


Figure 4-8: Comparison of the operational averaging techniques

As shown in Figure 4-8, the comparison between the raw acceleration profile and the 40 second mean demonstrates that the 40 second mean can remove all the sensor system noise throughout the pass and the any high magnitude oscillations similar to the one at -50 seconds. By removing these signals, the localized effects of the atmosphere shown in the 6.7 second mean are also removed. However, both the 6 second and 6.7 second means provide insight into these small scale effects.

An important issue with averaging density data was associating the data with a proper altitude. Pre-flight simulations, similar to simulations described in Section 4.3, showed that the straight average of altitudes will not reproduce the simulated density-altitude structure. This problem was attributed to the large density variations that could occur over 40 seconds of the orbit. To solve this problem density-weighted altitude averaging was used.

Density-weighted averaging involved the use of density values to construct the effective altitude. The method, shown in Equation 4-3, divides the summation of all

density and altitude products by a summation of the densities over the averaging range to determine the averaged altitude.

$$z_{AVG} = \frac{\sum_{i=1}^n \rho_i z_i}{\sum_{i=1}^n \rho_i} \quad (4-3)$$

In Equation 4-3, n is the number of points to be averaged, ρ_i is the density of the i^{th} point, and z_i is the altitude of the i^{th} point.

4.5 Special Products

Several special products were required by other MGS Project Teams. These special products included dynamic pressure, free-stream heat flux, ephemeris timing correction, effective scale height for NAV, and atmospheric disturbance level.

4.5.1 Dynamic Pressure and Free Stream Heat Flux

Dynamic pressure and free stream heat flux were used to evaluate present and future aerobraking passes for effectiveness and safety. Free-stream heat flux was calculated to monitor the heating levels in the solar arrays and dynamic pressure was a metric used to avoid further damage to the craft and to describe the effectiveness of aerobraking passes. Dynamic pressure and free stream heat flux are both functions of the density and the velocity of the spacecraft and are calculated using Equation 4-4.

$$q = \frac{1}{2} \rho v^2 \quad Q = \frac{1}{2} \rho v^3 \quad (4-4)$$

In Equation 4-4, q is the dynamic pressure, ρ is the density, v is the velocity of the spacecraft and Q is the free stream heat flux.

Note that using the operational data reduction process allowed for calculation of these two parameters at any time during the drag pass. This allowed the ACC Team to

calculate the maximum heat flux and dynamic pressure during each pass and also calculate the time of these maximum points in relation to the periapsis of the orbit

4.5.2 Ephemeris Timing Correction

Since the NAV Team would only commit to periapsis timing errors less than 225 seconds [Personal Communication, P. Esposito, 6/96], a method for refining the peripasis time to within 10 seconds was created. The product, called ephemeris timing correction (ETC), was the time in seconds from the NAV estimated periapsis time to the time of actual periapsis assuming a symmetrical atmosphere. A symmetrical atmosphere has no latitudinal or longitudinal variation, i.e. densities encountered before periapsis are equal to densities calculated after periapsis. To determine the ETC, the time corresponding to the accelerometer measurements was shifted until all variation between pre- and post-periapsis densities were minimized. The amount of time shift which minimizes this variation was the ETC.

When tested on models with symmetric atmospheres, the ETC process could detect errors in periapsis time on the order of 1 second. This process was not used during aerobraking because NAV team timing errors were consistently less than 3 seconds and average timing errors calculated with ETC were 10 seconds. This lack of accuracy in the ETC product shows the very non-symmetric nature of the Martian atmosphere.

4.5.3 Effective Scale Height for NAV

As part of the orbit determination process, the NAV team estimated the density at periapsis using a constant density scale height model of the atmosphere. Since the NAV team could not determine scale height, a process was generated to use accelerometer data to estimate a scale height that best describes the entire pass. This scale height was known as 'Effective Scale Height for NAV'.

The following procedure was used to calculate 'Effective Scale Height for NAV'. First, the density calculated at periapsis by the accelerometer was assumed to be the

correct density. Second, the total change in velocity recorded by the accelerometer during the entire pass was calculated by determining the sum of all individual 0.1 second measurements. To correct for differences between accelerations in the z-direction and accelerations along the velocity vector, each accelerometer point was divided by the cosine of U_x and U_y before the summation was taken. Third, a density profile was generated using a constant density scale height model with the accelerometer-calculated periapsis density and an arbitrary scale height. Fourth, Equation 3-1 was used to calculate accelerations over the entire pass from the density profile generated in step three and the NAV constant ballistic coefficient ($C_D=1.99$, $A=17.03$). The sum of the accelerations from step 4 was compared to the total acceleration calculated in step 2. Finally, steps 3 and 4 are repeated changing the arbitrary scale height until the difference between the acceleration in step 2 and in step 4 was minimized. The scale height which minimizes this process was the ‘Effective Scale Height for NAV’.

4.5.4 Atmospheric Disturbance Level

To describe the volatility of the atmosphere, a metric was devised so that the magnitude of changes in density could be compared from pass to pass. The metric, known as Atmospheric Disturbance Level (ADL), is defined by Equation 4-5.

$$ADL = 200 * 10^{\frac{1}{5} \sqrt{\left(\frac{\sum_{i=O-5}^O \frac{\log_{10}(\rho_{i-1})}{\log_{10}(\rho_i)}}{\frac{\sum_{i=O-5}^O \frac{\log_{10}(\rho_{i-1})}{\log_{10}(\rho_i)}}{6}} \right)^2}} \quad (4-5)$$

In Equation 4-5, O is the present orbit number and ρ_n is the density of the n^{th} orbit. ADL examines the 2 sigma percent deviation of the density ratios of 6 previous orbits relative to the mean density ratio.

4.6 Prediction Methods

Two basic prediction methods using accelerometer data were developed for MGS aerobraking: the wave model and the look ahead model.

The wave model was based on the discovery that Mars has two distinct density peaks on opposite sides of the planet which remain in the same general area over long periods of time [16]. This discovery was made after a standing wave pattern was recognized in the density data. To form a prediction model using this discovery, a least-squares process was used to determine the constants of a standing-wave density model. The inputs to the least squares process were the densities and the longitudes of a set of previous orbits. To predict future densities, this model was evaluated at the predicted longitudes of the future orbits. The wave model used during aerobraking, shown in Equation 4-6, contains a constant term, a linear term, and standing wave 1 and wave 2 terms. A standing wave 1 is defined as a sinusoidal density variation with a 360 degree longitude variation and a wave velocity equal to zero. Wave 2 is similarly described except a full wave 2 has a 180 degree longitude variation.

$$\rho_{\text{model}} = A_0 + A_1 t + A_2 \cos L + A_3 \sin L + A_4 \cos(2L) + A_5 \sin(2L) \quad (4-6)$$

In equation 4-6, A_{0-5} are constants determined from previous orbits, t is time, L is the longitude and ρ is the density.

The look-ahead model was based on the assumption that the density over any latitude will form a consistent density profile independent of time. To calculate predictions, data from previous orbits at the same latitude as the prediction periapsis were fit with a constant density scale height atmospheric model. This model was extrapolated downward to the altitude of the prediction point to determine the density prediction. A sample diagram describing how the model works is shown in Figure 4-9.

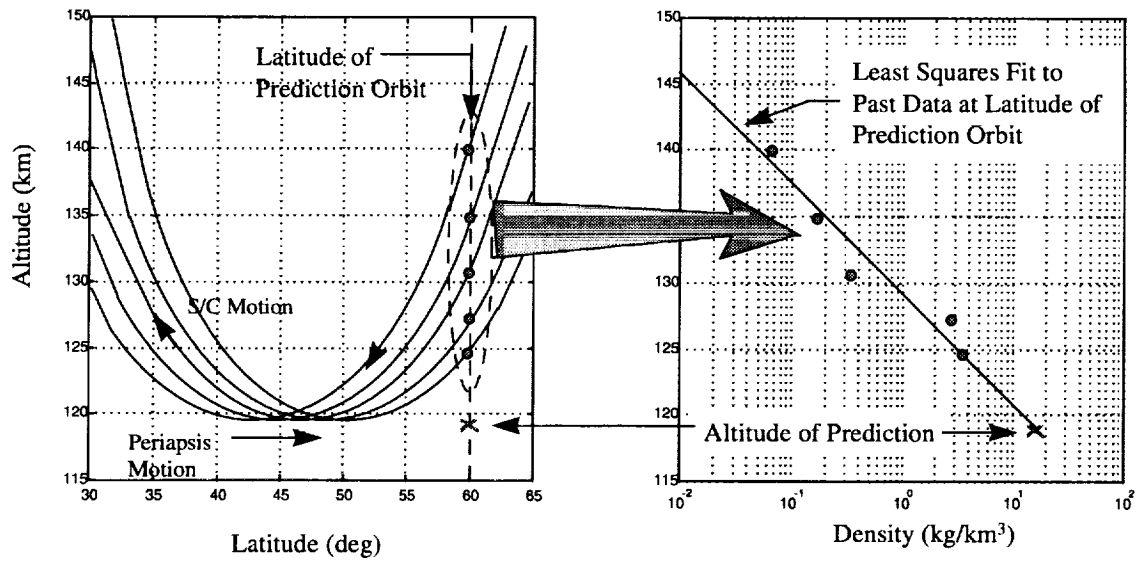


Figure 4-9: Look-ahead model diagram

5. Analysis of Process Errors

Section 5 analyzes the error induced into the calculations of density by the operational methods described in Section 4. The total induced error can be determined by the root-mean square of all the possible errors inherent to these methods. These error sources include:

1. Ephemeris errors
2. Errors in determining ballistic coefficient
3. Errors in determining bias
4. Digitization errors due to the accelerometer instrument

5.1 Ephemeris Errors

Ephemeris errors include errors from the use of periapsis osculating elements away from periapsis, and timing and altitude errors from orbital elements generated by the NAV Team. Errors from the use of osculating elements are described in Section 3.2. Timing error is the amount of time that elapses from the actual periapsis point to the one predicted by the NAV Team, assuming the orbit is correct. Altitude error is the error in altitude assuming the timing of periapsis is correct. From discussions with the NAV Team [Personal Communication, P. Esposito, 6/96], the ephemeris errors in a reconstructed orbit were estimated at 0.1 km in altitude and 0.1 second in time.

Total altitude error is the combination of the range errors in Section 3.2 and NAV altitude errors. The equivalent density error was determined by solving the equation of a standard exponential atmosphere ($\rho = \rho_0 \exp[\Delta H/H_s]$) for density ratio, ρ/ρ_0 , assuming a scale height, H_s , of 7 km and a ΔH of the corresponding total altitude error. The results of the total altitude error for several altitude ranges are shown in Table 5-1.

Table 5-1: Total Altitude Error Results

Altitude Range (km)	Section 3.2 Avg Range Error (km)	NAV Altitude Error (km)	Total Altitude Error (km)	Equivalent Density Error (%)
103 (periapsis)	0.0001	0.1	0.1001	1.44
110-120	0.0507	0.1	0.1507	2.18
120-130	0.0896	0.1	0.1896	2.75
130-140	0.1166	0.1	0.2166	3.14
140-150	0.1376	0.1	0.2376	3.45
150-160	0.1553	0.1	0.2553	3.71
160-170	0.1718	0.1	0.2718	3.96

To determine timing error, a constant density scale height atmospheric model with no latitudinal variation was simulated with an density data point every 0.1 seconds. The data points were then shifted 0.1 seconds forward in time to simulate the 0.1 second timing error. The error between the shifted and original points was calculated by subtracting the shifted value from the original value and then dividing by the original value. The equivalent density error was calculated as the average of these errors over several different altitude ranges and shown in Table 5-2.

Table 5-2: Ephemeris Timing Error Results for 0.1 Seconds of Timing Error

Altitude Range (km)	Equivalent Density Error (%)
103 (periapsis)	0.00
110-120	0.35
120-130	0.49
130-140	0.60
140-150	0.68
150-160	0.76
160-170	0.83

5.2 Errors in Determining Ballistic Coefficient

In determining ballistic coefficient, the spacecraft mass was assumed to be accurately known. Therefore, the error in determining ballistic coefficient was from errors in determining the force coefficient. The errors in the force coefficient tables were estimated by a combination of accommodation coefficient error and geometric modeling errors. A 10% change in accommodation coefficient was observed to produce a 2% change in force coefficient. Assuming the accommodation coefficient for MGS is

between 0.95 and 1.0 results in a 1% error in force coefficient. Error in force coefficient due to geometric model imperfections was estimated at 2% [Personal Communication, R. Wilmoth, 9/14/98]. Therefore, the error inherent to the calculation of force coefficient tables is the root-mean square of the accommodation coefficient and model imperfections errors or 2.24%. To determine total error in force coefficient, the inputs to the interpolation of the force coefficient tables, wind orientation and panel deflection, were also considered.

To calculate the wind orientation error, a 1 degree error in wind orientation was assumed. The greatest variation in the interpolation tables shows C_z changes from 2.12 for the free molecular table with $U_x=U_y=0$ to 1.98 for the free molecular table with $U_y=10$ degrees. This constitutes a 0.0134 C_z change per degree of orientation error which can be used to state that a 1 degree orientation error will cause a 0.65 % error in density estimation.

For determining error in calculation of panel deflection, the panel position calculated using methods from Section 4.4.3 and the panel deflection calculated from sun sensor data were compared. The greatest difference between the two independent calculations inside the atmosphere is approximately 1 degree. Using a similar method to the one used above, the greatest variation in the interpolation tables occurs from 2.12 for the free molecular table, with no panel deflection to 2.0194 for the free molecular table with 10 degrees panel deflection. This constitutes a 0.01006 C_z change per degree of panel deflection error which was used to state that a 1 degree deflection error will cause a 0.47 % error in density estimation.

5.3 Errors in Determining Bias

The average standard error in determining the bias was 0.005 counts/0.1 seconds. By simulating a sample pass using a linear temperature profile described in Section 4.2, the counts every 0.1 second can be determined at various altitude levels. By assuming a 0.005 counts/0.1 second error on each acceleration value, an error can be identified as a

function of acceleration. The equivalent density error is then the average acceleration error over each altitude interval and is shown in Table 5-3.

Table 5-3: Bias Percent Error as a Function of Count Level

Altitude Range (km)	Average Acceleration (counts/0.1sec)	Equivalent Density Error (%)
103 (periapsis)	9.060	0.06
110-120	2.119	0.24
120-130	0.618	0.81
130-140	0.219	2.28
140-150	0.089	5.63
150-160	0.040	12.60
160-170	0.019	25.95

Note that this density error is an orbit-to-orbit variation dependent on the ability to accurately determine the bias value. Since this error does not vary during the orbit, the scale heights determined from accelerometer data do not suffer from this error type.

5.4 Errors due to Instrument Output

The accelerometer instrument output suffers from quantization, only integer count levels can be reported by the instrument, and data rate errors, the same data rate can produce several permutations of the existing atmosphere. Both of these errors are determined by the simulations in Section 4.3. The results of the simulation done to investigate these errors for the 10 measurements per second case are repeated in Table 5-4 as the errors due to the accelerometer instrument output.

Table 5-4: Quantization and Data Rate Error Results

Altitude Range (km)	Average Acceleration (counts/0.1sec)	Equivalent Density Error (%) (10 acceleration measurements /sec)
103 (periapsis)	9.060	0.82
110-120	2.119	0.89
120-130	0.618	0.44
130-140	0.219	0.79
140-150	0.089	1.85
150-160	0.040	4.37
160-170	0.019	6.84

Note that at approximately 125 km, the accelerometer instrument is recording 1 count every 0.1 seconds. Without the averaging techniques used in the operational data reduction procedure, the error due to quantization of the signal at that altitude level should be 100%, ie the instrument could report 2 or 0 counts instead of 1 count. Table 5-4 shows that using averaging techniques outlined in this paper reduces this error to approximately 1%.

5.5 Total Data Reduction Process Error

By combining all the error sources described in Section 5.1 through 5.4, a total error was generated as a function of altitude and acceleration. The total error was found by taking the root mean square of all error sources. All the error sources and the total data reduction process error are shown in Table 5-5.

Table 5-5: Total Data Reduction Process Error

Altitude Range (km)	Average Density (kg/km ³)	Average Acceleration (counts/40s)	Ephemeris Errors		Ballistic Coef. Errors			Natural Bias Error (%)	Instrument Output Error (%)	TOTAL PROCESS ERROR (%)
			Altitude Error (%)	Timing Error (%)	Force Coef. Error (%)	Orientation Error (%)	Panel Deflection Error (%)			
103 (periapsis)	60.00	3624	1.44	0.00	2.24	0.65	0.47	0.06	0.82	2.90
110-120	13.91	847.6	2.18	0.35	2.24	0.65	0.47	0.24	0.89	3.37
120-130	4.12	247.2	2.75	0.49	2.24	0.65	0.47	0.81	0.44	3.78
130-140	1.46	87.6	3.14	0.60	2.24	0.65	0.47	2.28	0.79	4.66
140-150	0.59	35.6	3.45	0.68	2.24	0.65	0.47	5.63	1.85	7.29
150-160	0.27	16	3.71	0.76	2.24	0.65	0.47	12.60	4.37	14.07
160-170	0.13	7.6	3.96	0.83	2.24	0.65	0.47	25.95	6.84	27.24

The data in Table 5-5 is plotted in Figure 5.1. The left hand side of Figure 5-1 shows the total data reduction process error plotted as a function of altitude and the right hand side shows the same error as a function of density.

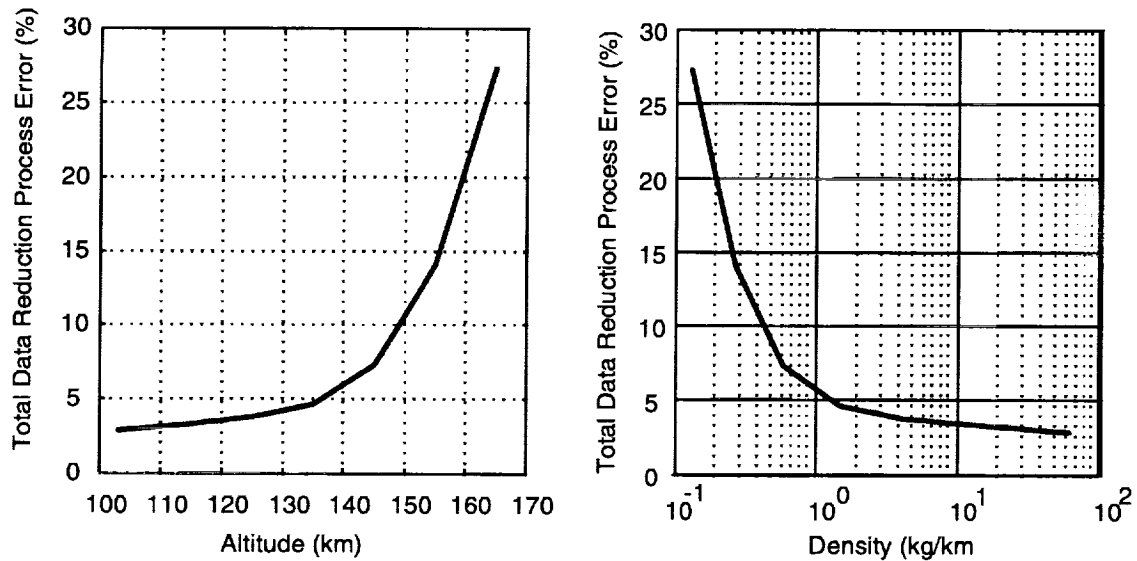


Figure 5-1: Accelerometer process error vs. model altitude and density

This study demonstrates that accelerometer measurements can be converted to density with only 5% error for the 33 km range between periapsis at 103 km and 136 km. Higher altitudes up to 162 km can be examined but 25% uncertainty should be expected. The total process error can also be examined as a function of density using the right hand side of Figure 5-1.

An important note is that the total process error developed in this section contains components that are only correct for the density structure used to generate these errors. Altitude error, timing error, natural bias error and instrument output error are all functions of the density and the density change with altitude. Since the density structure used here was based on a previous aerobraking orbit, the total process error results are typical of what was experienced during aerobraking at Mars but not indicative of every aerobraking pass.

6. Verification of Accelerometer Results

Section 6 presents the studies done to verify the accelerometer data reduction procedure outlined in Section 4. Studies were also performed to verify the effectiveness of prediction schemes described in Section 4.6.

6.1 Data Reduction Process Verification

To verify the accelerometer data reduction process, two data products were examined. The first product, SAM panel deflection, was estimated during the density iteration scheme. The Spacecraft (S/C) Team also calculated panel deflection by using spacecraft attitude data and data from sun sensors on the SAM. The second product, change in orbital period, was estimated by the ACC Team and the NAV Team.

6.1.1 Panel Deflection Comparison: ACC vs. Sun Sensor

For all orbits in which SAM deflection angle was calculated using the sun sensor, the accelerometer calculated panel deflection was always within 1.5 degrees of the sun sensor data. Four passes are shown as examples of this accuracy. Passes 50, 100, 125 and 162 are shown in Figure 6-1.

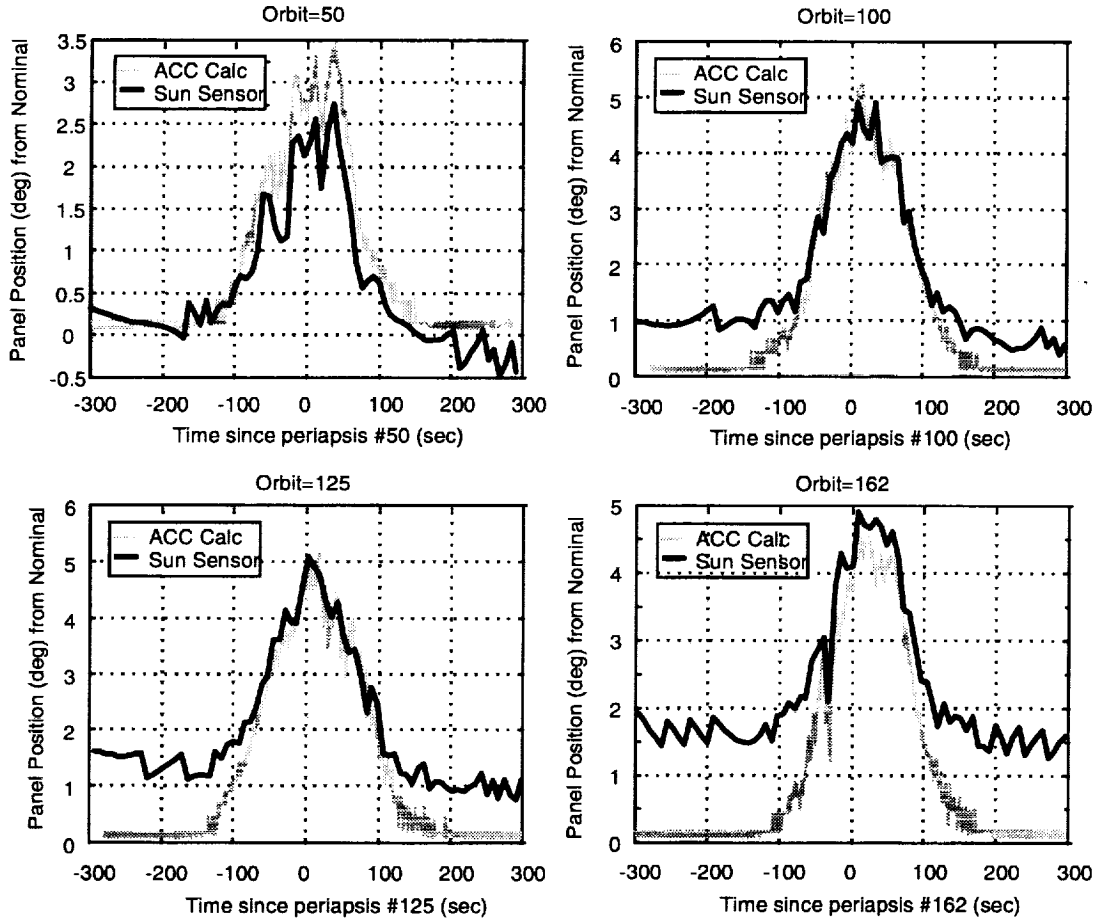


Figure 6-1: Comparison of panel position calculated using accelerometer data and sun sensor data

As shown in Figure 6-1, the two measurements are in good agreement near periapsis. The deviations outside this range were interpreted by the S/C Team as thermal distortion of the panel causing the crack to not fully close. The accelerometer-calculated deflection only considered aerodynamic forces, therefore, the deflection is zero outside the atmosphere. The agreement between the two measurements within the atmosphere validates the density iteration scheme and the convergence of the iteration scheme on the proper density values.

6.1.2 Orbital Decay Comparison: ACC vs Period Reduction

The NAV Team and ACC Team both monitored the change in orbital period due to drag during aerobraking. For high eccentricity orbits, the reduction in period is proportional to the density at periapsis multiplied by the square-root of the scale

height.[17] The product was used as a metric to compare drag calculations by the NAV Team and the ACC Team. In Figure 6-2, the $\rho\sqrt{H_s}$ product generated by NAV Team data was compared against the same product composed of the accelerometer calculated density at periapsis and the Effective Scale Height for NAV for orbits 140 to 200. Below the $\rho\sqrt{H_s}$ product plot in Figure 6-2 is the error between the two calculations.

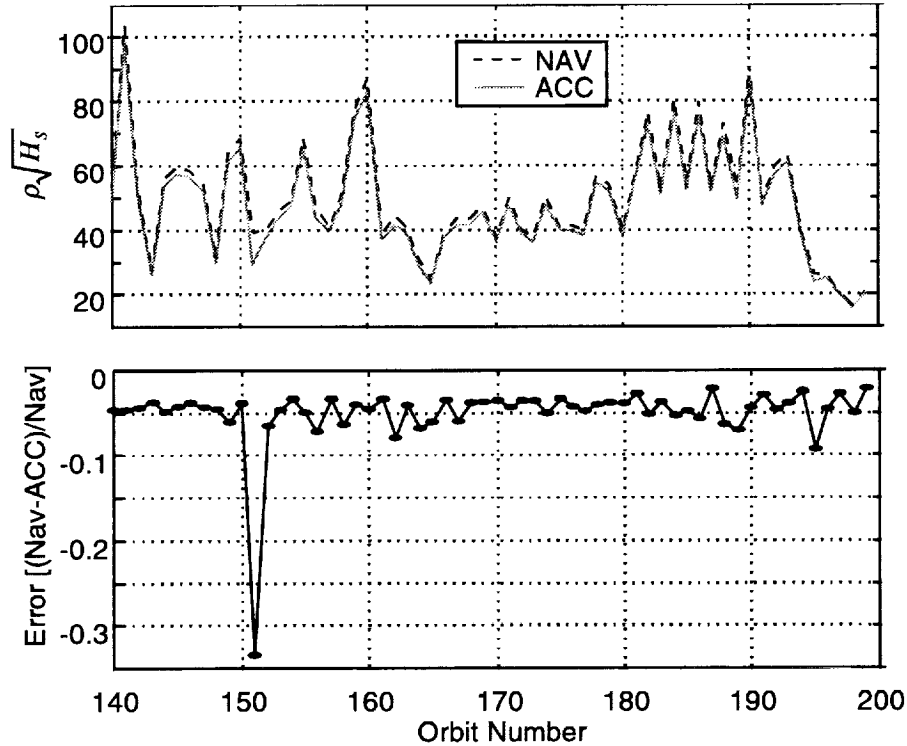


Figure 6-2: Orbital decay comparison of NAV and ACC using $\rho\sqrt{H_s}$ product

As shown, the ACC Team estimate of the $\rho\sqrt{H_s}$ product was on average 5% below the NAV Team estimate. This error was believed to be due to the differences between the constant drag coefficient used by the NAV Team (1.99) to calculate periapsis density and the variable force coefficient used by the ACC Team to calculate periapsis density. If the percent difference is calculated between the NAV coefficient of drag number of 1.99 and the average force coefficient near periapsis determined for this orbit range of 1.9, the 5% results. The ability to exactly reproduce the $\rho\sqrt{H_s}$ product generated by the NAV Team, validates the periapsis densities determined by the accelerometer data reduction process

and the method for isolating acceleration due to aerodynamic forces from the measured acceleration over the entire pass.

The ‘Effective Scale Height for NAV’ product was also validated using the $\rho\sqrt{H_s}$ product. Two simulation runs of aerobraking passes were made, first with the NAV Team scale height and then with the ACC Team effective scale heights. The results of these tests are shown in Table 6-1 [Personal Communication, P.Esposito, 12/11/97].

Table 6-1: Results of NAV Simulation Runs with Accelerometer Calculated Effective Scale Height

Pass Number	NAV Scale Height	NAV Density Using NAV H_s	ACC Effective Scale Height	NAV Density Using ACC H_s	ACC Calculated Density
59	7.0	8.83	11.5	6.92	7.23
60	7.0	12.90	6.21	13.55	14.60

Comparing the NAV density calculated using the NAV scale height to the ACC density values resulted in a 22% error for pass 59 and a 12% error for pass 60. If the NAV density is re-calculated using the ACC effective scale height, the error between NAV density and accelerometer density was reduced to 4% for pass 59 and 7% for pass 60. This demonstrates not only the dependence of the NAV Team on proper scale height information but how much improvement can be made on orbit determination when a more precise calculation of scale height can be made.

6.2 Prediction Scheme Verification

To verify the prediction methods, densities of previous passes were predicted and compared to the actual density calculated for that orbit. Prior to aerobraking the MGS project estimated the variability inherent to the Martian atmosphere at a two sigma value of 70%. Therefore, an accurate prediction method is one that could consistently predict upcoming densities below this variability value.

Several prediction schemes were used during aerobraking. These schemes included: Persistence, which used scale height and density of the previous pass to predict one orbit ahead; 5-Orbit Mean, which used 5 previous densities, scaled to the

prediction orbit altitude and then averaged, to predict ahead; and the wave model and the look-ahead model both described in Section 4.6.

To compare these models, passes 100 through 200 were predicted with each model assuming the spacecraft had just experienced the previous pass. Persistence, 5-orbit mean and the wave model predict 1 orbit ahead, while the look-ahead model predicts 20 orbits ahead. The predictions were then compared to what actually was measured by the ACC Team for that pass. An error was determined for each point as well as the mean and standard deviation of that error for the entire range of passes from 100 to 200. The prediction error plots for each model are shown in Figure 6-3.

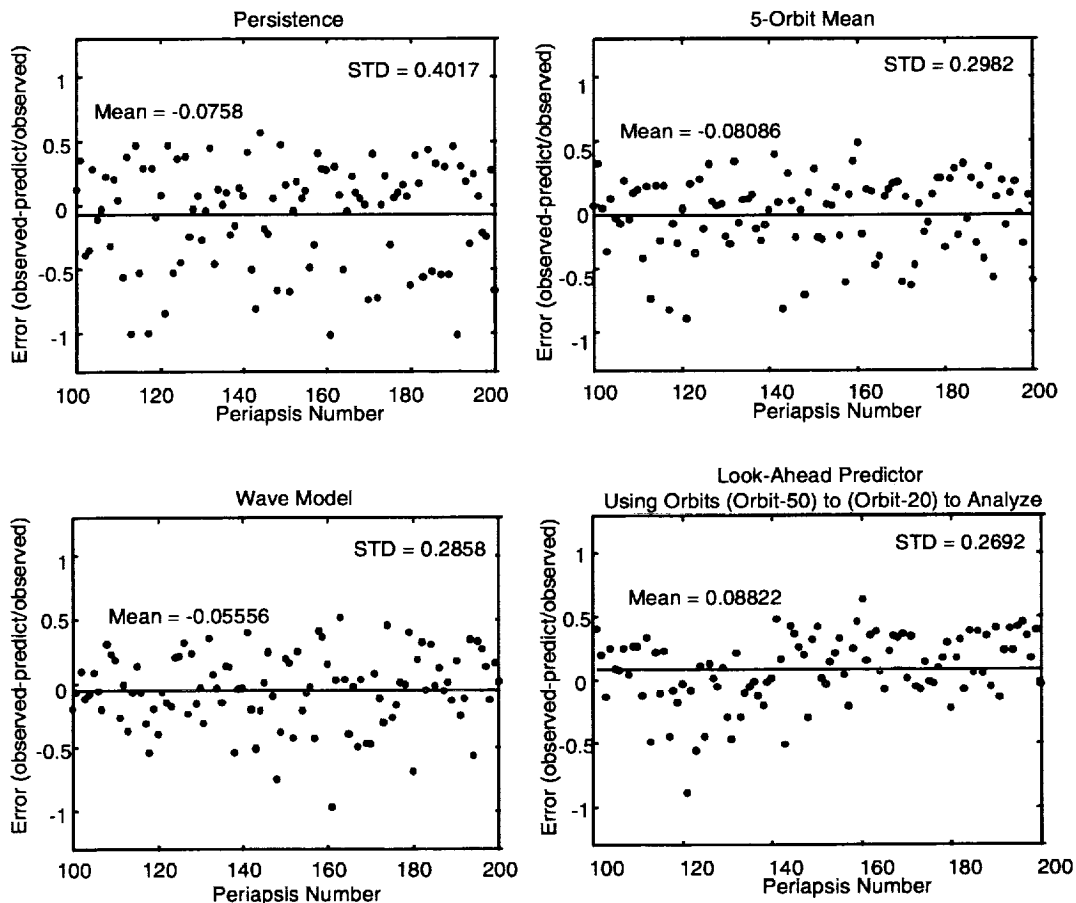


Figure 6-3: Comparison of effectiveness of persistence, 5-orbit mean, longitudinal wave, and look ahead prediction schemes over Orbits 100-200

Each model predicted the mean within 9% of the actual, however, the standard deviations of each model vary from 40% for the persistence model to 27% for the look-ahead model. The wave model, used for predictions during aerobraking, has a standard deviation of 29%, or a 2 sigma variability of 58%. This value was below the 2 sigma atmospheric variability parameter of 70% and, therefore, the predictions made by the ACC Team during the first phase of aerobraking were within the constraints originally set by the MGS project.

An important note, by examining the persistence model, the actual atmospheric variability of the atmosphere over this range of orbits can be determined. The two sigma atmospheric variability is approximately 80%. This value is slightly higher than the pre-aerobraking project estimate of 70%.

For predicting one orbit ahead the wave model produces the lowest standard deviation of all the methods and also produces the most accurate results (wave model had the lowest mean error of all prediction methods). The results from the look-ahead model demonstrate that accurate long range predictions, up to 20 orbits into the future, are possible. Therefore, a new direction for predictions with accelerometer data could be the combination of the wave model and the look-ahead model into an accurate short range and long range predictor.

7. The Effect of Panel Vibration on MGS and the Accelerometer Data Reduction Process

The vibration of the SAM panel has contributed a 6.7 second period oscillating signal to the acceleration. Three methods were developed to remove this signal: averaging described in Section 4.4.4, the 4-DOF dynamics model described in Section 3.1.7, and a filtering process.

The filtering process used band-pass filtering to isolate the 6.7 second period signal in the accelerometer data. The filtered signal can then be subtracted from the measured acceleration to remove the effects of panel vibration. To quantify the band-pass filtered signal a least-squares process was then used to obtain the constants in Equation 7-1 which described the oscillating component of the acceleration data in terms of the oscillating components of the rates and angular accelerations.

$$a_{z_{BP}} = C_1 \omega_x + C_2 \alpha_x \quad (7-1)$$

In Equation 7-1, $a_{z_{BP}}$ is the acceleration in the spacecraft z-direction due to panel vibration, ω_x is the angular rate in the spacecraft x-direction filtered with a similar band-pass as above, α_x is the band-pass filtered angular acceleration in the spacecraft x-direction, and C_1 and C_2 are the constants determined in the least squares process.

This section will describe the effectiveness of the 4-DOF dynamics model in determining the oscillating component of the acceleration data. Since the results from the model do not exactly agree with results from the filtering process, sensitivity studies were performed to determine which combinations of spacecraft and SAM physical properties could make the two methods agree. Finally, the effectiveness of averaging techniques used to compensate for the panel vibration signal are determined by comparing the results of the 4 DOF dynamics model method to several different averaging techniques.

7.1 Effectiveness of the 4 DOF Dynamics Model

To demonstrate the effectiveness of the 4 DOF dynamics model in removing the acceleration component due to panel vibration, sample plots were generated for several passes. The sample plots, shown in Figures 7-1 and 7-2, were generated using rate data from the spacecraft, physical data of the SAM shown in Appendix E. In these figures, the raw acceleration profile is shown on top, the acceleration profile after using the 4-DOF model, from Section 3.1.7, in the middle, and the profile after using the filtering method on the bottom.

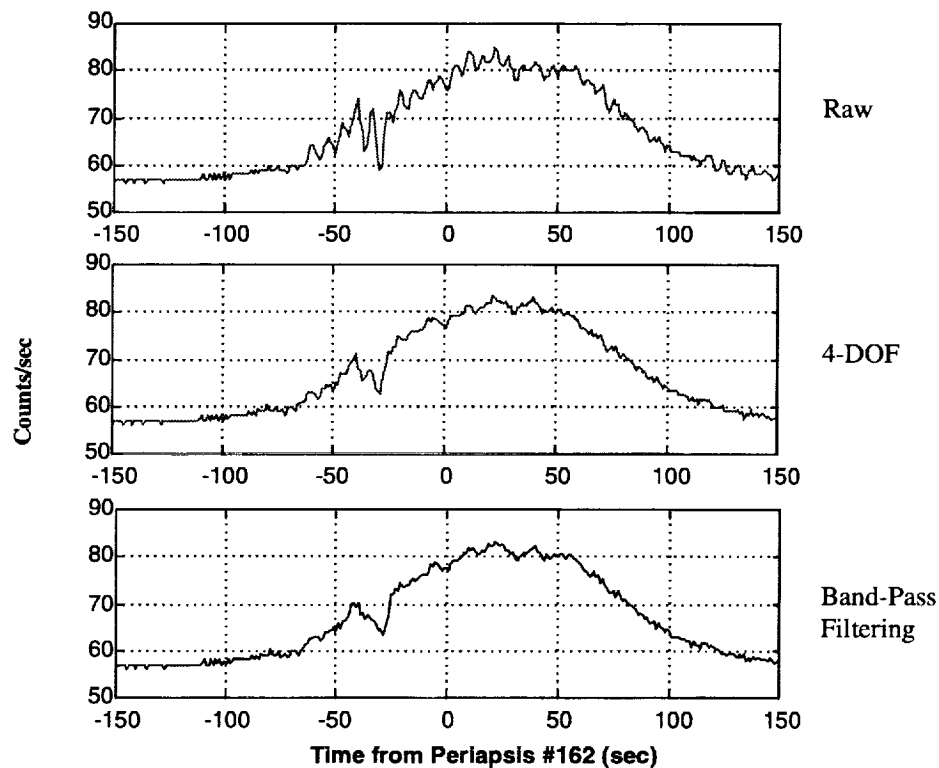


Figure 7-1: Acceleration profiles for Orbit 162 - raw data, reduced data using 4 DOF model, and reduced data using band-pass filtering method

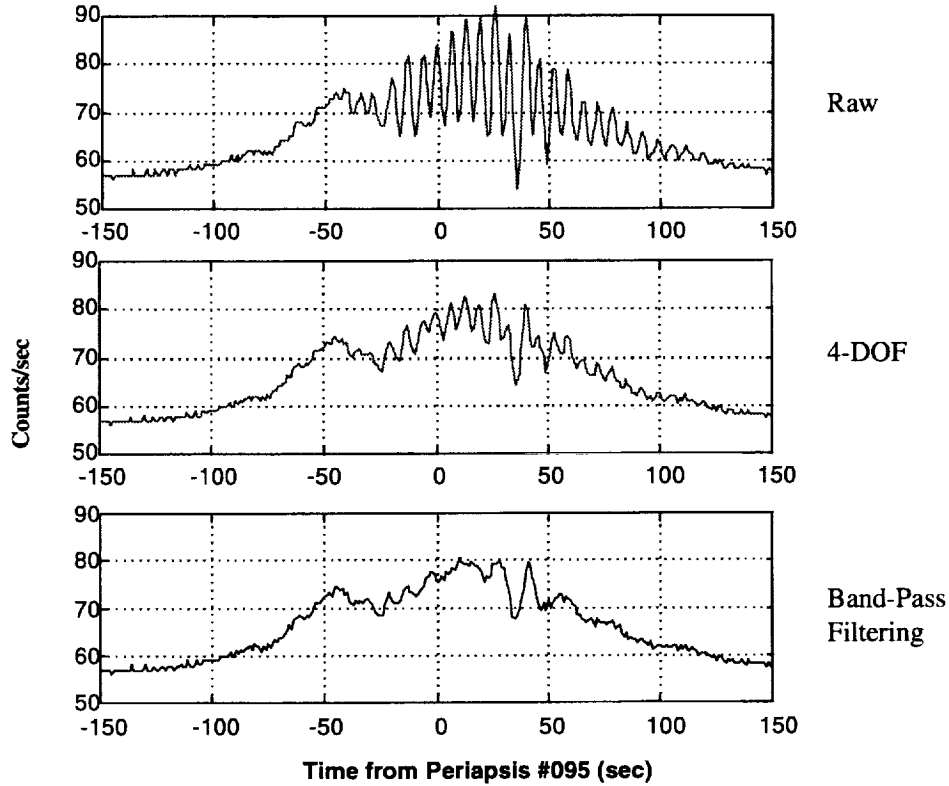


Figure 7-2: Acceleration profiles for Orbit 95 - raw data, reduced data using 4 DOF model, and reduced data using band-pass filtering method

The difference between the two processes can be quantified using Equation 7-1. The constants, C_1 and C_2 , from the filtering process were determined to be approximately $-211 \text{ counts}/(\text{rad/s})$ and $-2339 \text{ counts}/(\text{rad/s}^2)$, respectively, for all orbits examined. The dynamics model method can be reduced to the similar equation described only by the C_2 term. The value of C_2 for the dynamics model is $-2115 \text{ counts}/(\text{rad/s}^2)$. Therefore, the two different processes are only 10% apart. If the filtering method is assumed to compensate for all the vibration signal, the 4 DOF dynamics model and the physical properties used in this model can be further examined to give a better insight on the panel vibration.

7.2 Verification of the Dynamics Model And Assumptions

To check the validity of the derivation of the 4 DOF dynamics model, all the terms describing the panel deflection motion were set to zero. If the panel deflection is set to zero and the center of mass of the system is assumed to be at the center of mass of the

BUS+SAP body, the C_2 constant determined by the combined process of the dynamics model and the angular method, outlined in Section 3.1.7, should result in the same C_2 if only the angular method, outlined in Section 3.1.5, is used and the center of mass of the system is assumed to be at the center of mass of the spacecraft. When the panel deflection terms were set to zero, the C_2 values determined were equal to each other. The spreadsheet demonstrating this calculation is shown in Appendix F.

To validate the small angles assumption, the panel deflection and the spacecraft angular position about the spacecraft x-axis were further examined. The panel deflection exceeded 5 degrees under the normal effects of the atmosphere. However, the vibration amplitude never exceeded 1 degree off this quasi-steady state deflection. The same properties were observed in the spacecraft x-axis angular position. Therefore, the deflection angle and the x-axis angular position exceeded small angles but the vibrating components of these generalized coordinates did not. Since the 4 DOF dynamics model is only concerned with the vibrating components of these coordinates the small angle approximation is valid.

To validate the 'no external forces' assumption, the atmospheric force on the two bodies was further examined. The force of the atmosphere on the panel and the remaining part of the spacecraft were different due to the different surface areas. However, this force difference did not oscillate with the 6.7 second period vibration signal. The oscillation of the atmospheric force would be too low a frequency to affect the short period oscillation of the damaged panel. Therefore, if the two oscillations never affect each other, the no external forces assumption is valid.

A unique problem arises when the 4 DOF dynamics model is modified to examine the effect of external forces on the spacecraft. To determine the external forces on the spacecraft, the density and the force coefficients must be known. However, the accelerometer data used to determine density contains the vibration. By adding external forces to the equation, the vibration would be added twice to the problem. To apply

external forces to the model, the forces must be determined by the aerodynamic forces alone. Band-pass filtering of the accelerometer data may reveal accelerations due to the aerodynamics alone, however, the filtering process may also remove the data necessary to show that the natural oscillations of the atmosphere and of the damaged panel are resonating and amplifying the vibration of the panel.

7.3 Sensitivity Studies on Panel Physical Parameters

Assuming the dynamics model outlined in Section 3.1.7 is valid, sensitivity studies were performed to analyze the effect of modifying the physical properties used in the dynamics model. The properties used in the sensitivity study were the mass of the broken SAM section, the moment of inertia of the SAM broken section, the center of mass position of the broken SAM section, and the yoke crack position. Except for crack position, each of these studies were performed by modifying the individual parameters mentioned above without disturbing the other parameters. For crack position, parameters were generated by choosing a position for the crack and then modifying the other parameters (SAM mass, SAM moment of inertia, and SAM center of mass) so that the crack position described the object which is vibrating. Table 7-1 describes the position of the crack and the resulting physical parameters used in the crack position sensitivity study. In Table 7-1, position #2 corresponds to the position of the hinge between the yoke and the panel and position #4 corresponds to the best estimate of the crack position by Lockheed Martin Astronautics (LMA).

Table 7-1: Crack-Line Position and Resulting Physical Parameters for Sensitivity Study

Position	SAM mass	SAM CG			Ixx SAM	Hinge Pos		
#	kg	x	y	z	kg-m2	x	y	z
1	22.174	-0.032	-2.99	2.473	38.2325	0.038	-1.52	1.49
2 (hinge)	27.896	-0.023	-2.79	2.339	47.09	0.038	-1.31	1.355
3	33.618	-0.015	-2.59	2.204	55.9475	0.038	-1.11	1.221
4 (LMA)	39.34	-0.006	-2.39	2.07	64.805	0.038	-0.9	1.086
5	45.062	0.003	-2.18	1.936	73.6625	0.038	-0.7	0.952

The trends developed from the sensitivity studies of SAM moment of inertia, SAM mass, SAM center of mass and crack position are shown below in Figures 7-4

through 7-7. C_2 is used as a metric to describe the effect of modifying the physical parameters on the dynamics model. In each figure, C_2 is shown as a function of the modified physical parameter. Also shown on each figure is a line demonstrating C_2 from the filtering method. This line represents the physical parameters necessary to make the 4 DOF dynamics model reproduce the same results as the filtering method.

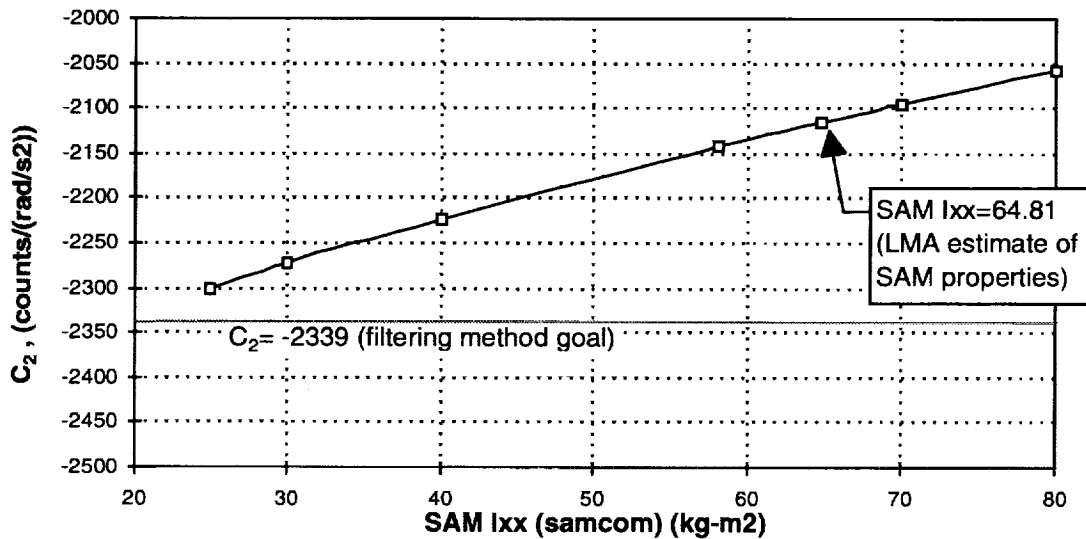


Figure 7-3: Sensitivity study on SAM moment of inertia about the spacecraft x-axis at the SAM center of mass

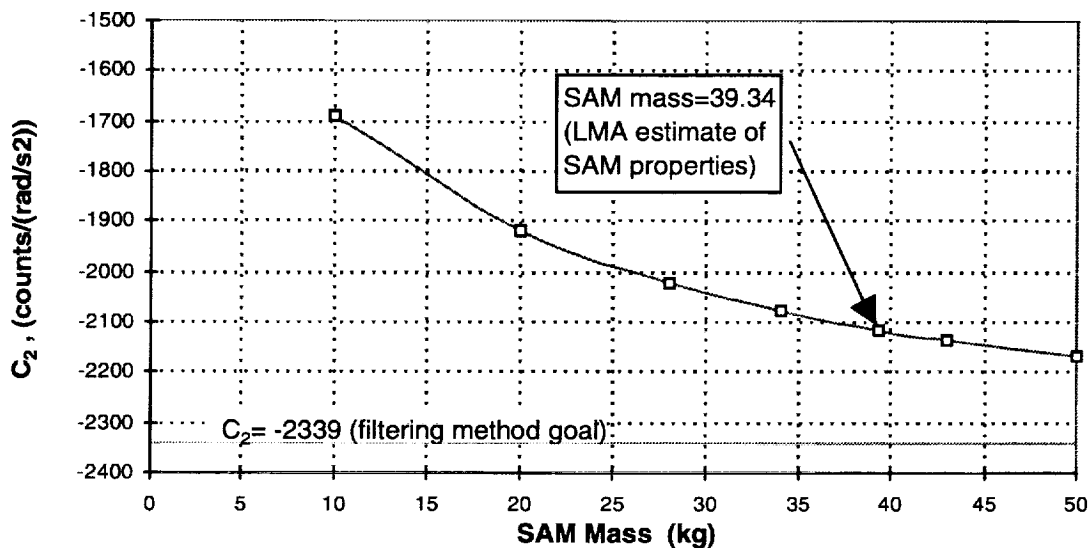


Figure 7-4: Sensitivity study on SAM mass

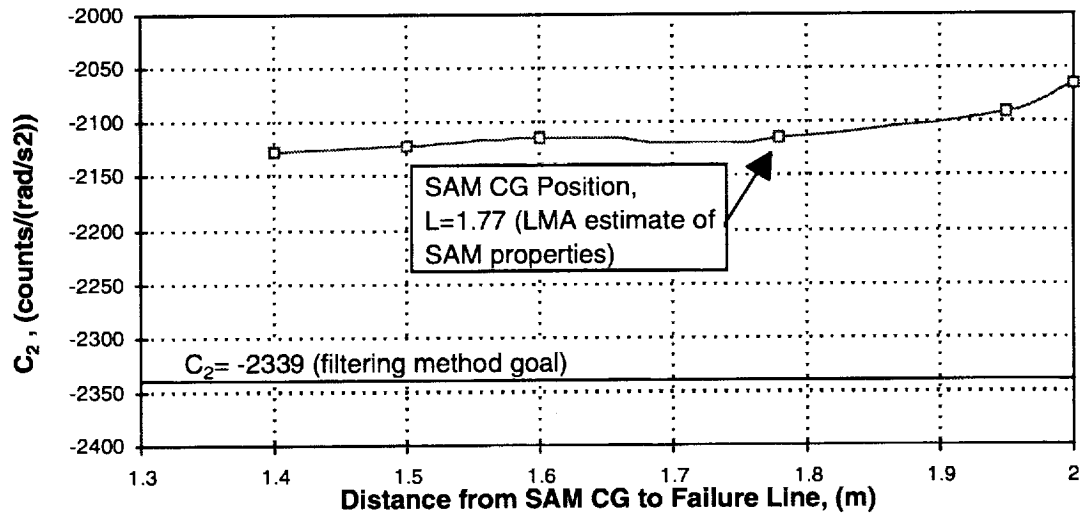


Figure 7-5: Sensitivity study on SAM center of gravity position

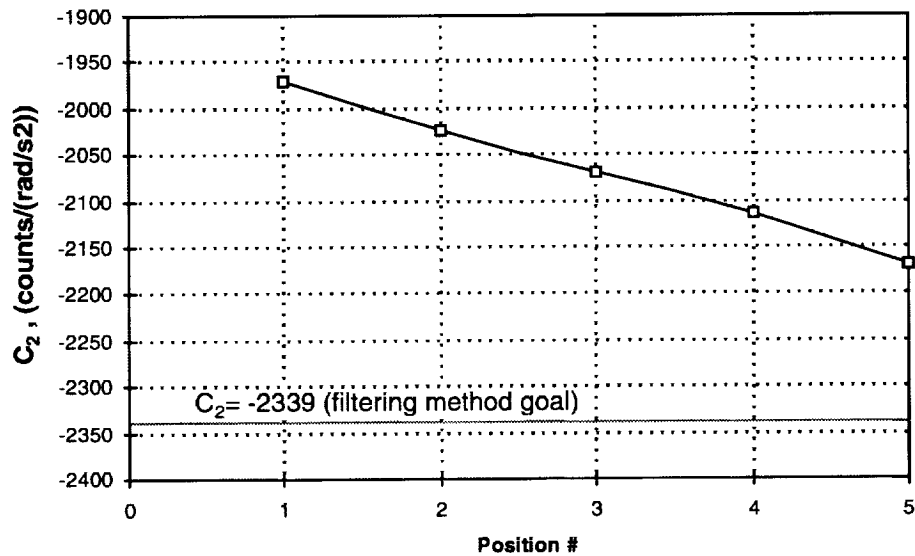


Figure 7-6: Sensitivity study on crack-line position

From examining the four studies above, it can be shown that only unrealistic modifications to the SAM moment of Inertia, SAM mass, SAM center of mass position, or crack position will allow the dynamics model to agree with the filtering method. If the dynamics model is assumed to be correct, this data demonstrates that something else may be moving on the spacecraft with the same vibration frequency as the damaged panel.

7.4 Averaging Techniques Used to Compensate for Vibrating Panel Effects

Before the development of the 4 DOF dynamics model or the filtering process, accelerometer fluctuations due to panel vibration were compensated for by various averaging techniques described in Section 4.4.4. The comparison can now be made between what is presently believed to be the aerodynamic acceleration and what was believed to be the aerodynamic acceleration during aerobraking. Figure 7-7 demonstrates the comparison between the acceleration profile developed using the 4 DOF dynamics model and the profile developed using averaging for Pass 162. The graph on the left in Figure 7-8 is the comparison between the 4 DOF dynamics model (gray line) and the 40 point running mean averaging technique (black line). The graph on the right in Figure 7-7 is the comparison between the 4 DOF dynamics model (gray line) and the 6 point running mean averaging technique (black line).

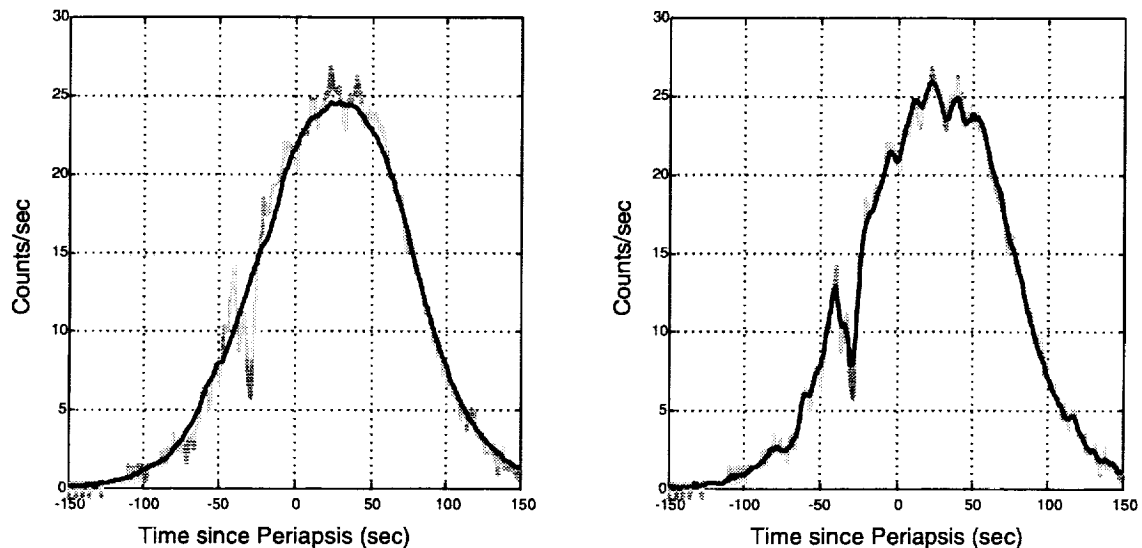


Figure 7-7: Comparison between 4 DOF dynamics model and 40 pt (left) and 6 pt running means (right) for Orbit 162

Figure 7-7 shows that the 40 point average accurately describes the general trend of the overall pass and the 6 point average describes the small effects of the atmosphere as originally planned. Most importantly, Figure 7-7 shows that averaging of data is the simplest method to compensate for unwanted vibrations in the accelerometer signal.

8. Conclusions

Aerobraking is a low-cost technique which was employed during the MGS mission and will be used on many upcoming missions. To effectively aerobrake, the density which the spacecraft encounters on every aerobraking pass must be known. No accurate density models had been created for the Martian atmosphere at the time of MGS, therefore, the MGS project was dependent on densities estimated by operational methods to plan the altitudes at which aerobraking would occur. Aerobraking at Mars was made even more complex and risky by the malfunction of one of the two solar arrays during initial deployment.

The MGS Accelerometer Team, formed at George Washington University, used an operational data reduction procedure to estimate densities given acceleration data from an on-board accelerometer instrument. This paper has described the operational data reduction procedure and has also described two methods used to predict the densities of upcoming orbits. These density estimations and predictions formed the basis for the planning of aerobraking altitudes during the first 201 orbits of MGS aerobraking. In addition, the operational data reduction procedure has provided the density data necessary for 1) the discovery of two longitudinal density bulges on opposite sides of Mars and 2) the first record of the effects of a dust storm on the density of the Martian neutral upper atmosphere.

The operational data reduction procedure was developed around an iterative process which determines density by calculating the deflection of the damaged solar array and a variable force coefficient which accounts for aerodynamic flight regime, spacecraft orientation and solar array deflection. This procedure has been demonstrated to determine densities up to 33 km above periapsis in 7 minutes (approximately 1/20th of 2 hour time period allotted for MGS operational density analysis). The possible errors over this altitude range were determined to be less than 5% by considering the total density

error from ephemeris errors, errors in force coefficient and instrument errors. The accuracy of this procedure has also been verified by comparing the solar array deflection and orbital period reduction calculated by this procedure to independent calculations performed by other MGS Teams including the Navigation and Spacecraft Teams.

The damaged solar array deflected and vibrated each pass through the atmosphere, producing an oscillating signal in the accelerometer data. To analyze and remove this signal, three methods were developed: averaging, band-pass filtering and a 4 degree of freedom dynamics model. By using the averaging method, the analysis of accelerometer data was not affected by this vibration. By comparing the remaining two methods developed to analyze the vibration signal, a greater understanding of the dynamics of the panel and the spacecraft was established. The 4 degree of freedom model successfully compensated for 90% of vibration signal determined by the filtering process. Sensitivity studies, performed to determine the source of the outstanding 10%, revealed that the remaining signal may be due to external forces not represented in the model or another component on the spacecraft moving at the same vibration frequency such as fuel sloshing.

References

- [1]- "Mars Global Surveyor Fact Sheet", Jet Propulsion Laboratory Publication, JPL 410-44-2, Dec 1994.
- [2]- Dallas, S. Sam, "Mars Global Surveyor Mission." Presented at the 1997 IEEE Aerospace Conference, Snowmass at Aspen, CO, 1997. Vol. 4, pp173-189.
- [3]- Lyons, D.T., "Aerobraking Magellan: Plan Versus Reality," AAS-94-118, 1994.
- [4]- Tolson, R.H., et al., "Magellan Windmill and Termination Experiments," Spaceflight Dynamics, CNES June 1995 Conference, Toulouse, France.
- [5]- Keating, G.M. et al., "Models of Venus Neutral Upper Atmosphere: Structure and Composition," *Adv. Space Res.* Vol. 5, No. 11, 1985 pp 117-171.
- [5]- Shane, R.W. and Tolson, R.H., "Aerothermodynamics of the Mars Global Surveyor Spacecraft," NASA/ CR-1998-206941, March 1998.
- [7]- Wilmoth, R.G. et al., "Rarefied Aerothermodynamic Predictions for Mars Global Surveyor," To be published in the Journal of Spacecraft and Rockets.
- [8]- Kahn, R. et. al., Mars, H.H. Kieffer, B.M. Jakosky, C.W. Synder, M.S. Matthews, Eds., Univ. of Arizona Press, Tucson, 1992. Pp 1017-1053. Martin, L.J. and Zurek, R.W., Journal of Geophysical Research, 97, 3221, 1993.
- [9]- Lyons, D. T. et al., "Mars Global Surveyor: Aerobraking Mission Overview." To be published in the Journal of Spacecraft and Rockets.
- [10]- Diamond, P.S. and Tolson, R.H., "A Feasibility Study of a Microgravity Enhancement System for Space Station Freedom." AAS Paper 93-626, August 1993.
- [11]- Larson, W. J. and Wertz, J.R., Space Mission Analysis and Design, Microcosm Inc, CA, 1992.
- [12]- Meirovitch, L., Methods of Analytical Dynamics, McGraw-Hill Inc., 1970.
- [13]- Cestero, F.J. and Tolson, R.H., "Magellan Aerodynamic Characteristics During the Termination Experiment Including Thruster Plume-Free Stream Interaction." NASA/CR-1998-206940, March 1998.
- [14]- Henderson, D. M., "Euler Angles, Quaternions, and Transformation Matricies – Working Relationships," NASA TM-74839, JSC-12960, July 1977.

- [15]- Blanchard, R.C. and Walberg, G.D.. "Determination of the Hypersonic-Continuum/Rarefied-Flow Drag Coefficient of the Viking Lander Capsule 1 Aeroshell from Flight Data." NASA Technical Paper 1793, Dec 1980.
- [16]- Keating G.M., Cancro G. J., et al., "The Structure of the Upper Atmosphere of Mars: In-Situ Accelerometer Measurements from Mars Global Surveyor," Science, Vol. 279, March 13, 1998, pp 1672-1676.
- [17]- King-Hele, D., "Satellite Orbits in an Atmosphere: Theory and Applications," Blackie and Sons, Ltd, 1987.

Appendix A: Quick-Look Data Products

Actual Preliminary Quick-Look Sheet

--Preliminary Quick-Look File for Accelerometer Experiment (Keating et. al.) (GWU)--

Date and Time (UTC)= 1998- 65 T11: 0:6.227

Time of Calculation (EST)= 1998/ 3/ 6 8: 2:12.270

OPTG file: optg_i_980305_OD161_171_V1;

Periapsis#= 162 Ephemeris (PREDICT)

Altitude of Periapsis= 120.00 km, Periapsis N. Lat= 55.3 deg,

Periapsis E. Long= 39.3 deg(320.7 deg W. Long)

Periapsis Local Solar Time= 11.7 Martian Hrs

MGS Period from Periapsis Elements= 13.80 hrs Earth-Sun-Mars Angle= 202.4 deg

RESULTS

Accel Bias +/- Std. Error= 5.66 +/- 0.00 Counts/0.1sec

Effective Scale Height for NAV= 7.11 km

PERIAPSIS

Periapsis Density= 16.71 kg/km³

Estimated Periapsis Scale Height = 6.11 km (T= 109.6 K)

NAV Density Predict = 17.36 kg/km³

Periapsis Density/NAV Density Predict Ratio= 0.96

Dynamic Pressure at Periapsis = 0.179 N/m²

Freestream Heatflux at Periapsis= 0.083 W/cm²

Max density(18.96 kg/km³) and max dynamic pressure(0.203 N/m²) occurs 22 sec after periapsis

COMMENTS:

- 1) After correcting for altitude, periapsis density is 2% above and maximum density is 16% above our P162 prediction given in the P161 Intermediate Quick-Look.
- 2) After correcting for altitude, P162 periapsis density increased from P161 by 41%.
- 3) Extraordinarily strong latitudinal gradient of 11% per degree to the south averaged over 1 scale height. This is a strengthening of the strong latitudinal gradient detected on P161. When the gradient relaxes densities at periapsis are expected to increase.

Line by Line Description of Preliminary Accelerometer Quick-Look Sheet

Line	Value	Description
1	<i>title</i>	
2	Date and Time (UTC)	Time of Periapsis Passage
3	Time of Calculation (EDT)	Eastern Daylight Time which sheet was created
4	OPTG filename	Name of NAV file used to generate orbit data
5	<i>blank</i>	
6	Periapsis#	Number of Periapsis used in Analysis
6	Ephemeris	Describes the type of NAV product used to develop QuickLook: (PREDICT, INTERMEDIATE, FINAL)
7	Altitude of Periapsis	Geodetic Altitude of S/C periapsis in degrees
7	Periapsis N. Lat	Geodetic North Latitude of S/C Periapsis in degrees
8	Periapsis E. Long	East Longitude of S/C in degrees, developed using Mars pole parameters in OPTG at Date and Time
9	Periapsis Local Solar Time	Local Solar Time of S/C in hours measure from real sun subsol point at Date and Time (24 hours/ day) (Midnight - >LST=0.0)
10	<i>blank</i>	
11	MGs Period from Periapsis Elements	Orbital period developed using periapsis orbital elements
11	Earth-Sun-Mars Angle	Angle between the Earth and Mars using the Sun as the middle point
12	<i>blank</i>	
13	<i>subtitle</i>	
14	<i>blank</i>	
15	Accel Bias +/- Std. Error	Accelerometer Instrument Bias and Standard Error calculated by averaging accelerometer values above the atmosphere before the start of the drag pass
15	<i>blank</i>	
16	Effective Density Scale Height for NAV	Density Scale Height in km corresponding to a spherically symmetrical atmosphere with a constant temperature. See Section 4.5.2
17	<i>blank</i>	
18	<i>subtitle</i>	
19	Periapsis Density	Density at periapsis
20	Estimated Periapsis Scale Height	Temperature and scale height in close proximity to periapsis
21	NAV Density Predict	Density estimation at periapsis from NAV
22	Periapsis Density/ NAV Density Predict Ratio	Ratio of Accelerometer density and NAV Predicted density RATIO=Line 19 / line 21
23	Dynamic Pressure at Periapsis	Dynamic Pressure at Periapsis in N/m2 DYN. Press.=1/2*density (line 18) *Periapsis Velocity.**2
24	Freestream Heatflux at Periapsis	Freestream Heatflux at Periapsis in W/cm2 Qdot=1/2*density (line 18) *Periapsis Velocity.**3
25	Max density Occurrence	Density, dynamic pressure and time of maximum density in reference to periapsis time
27	<i>blank</i>	
28	Comments	Human analysis of 'Quick-Look' data

Actual Intermediate Quick-Look Sheet

--Intermediate Quick-Look File for Accelerometer Experiment (GWU)--
 Date and Time (UTC)= 1998- 65 T11: 0:6.356
 Time of Calculation (EST)= 1998/ 3/ 6 12:12:11.220
 OPTG file: optg_i_980305_OD161_171_V1;

Periapsis#= 162 Ephemeris (INTERMEDIATE)
 Altitude of Periapsis= 120.00 km, Periapsis N. Lat= 55.3 deg,
 Periapsis E. Long= 39.3 deg(320.7 deg W. Long)
 Periapsis Local Solar Time= 11.7 Martian Hrs

MGS Period from Periapsis Elements= 13.80 hrs Earth-Sun-Mars Angle=
 202.4 deg

RESULTS

Accel Bias +/- Std. Error= 5.66 +/- 0.00 Counts/0.1sec
 Effective Scale Height for NAV= 7.05 km

	Periapsis	INbound	OUTBound
		130km	130km
Effective Density (kg/km3)	16.76	1.52	5.52
Scale Height (km)	6.06	5.23	6.60
Estimated Temperature (degK)	108.7	93.8	118.4
Dynamic Pressure (N/m2)	0.179	-	-
Freestream Heatflux (W/cm2)	0.083	-	-
Density/5-orbit mean	-	0.59	1.33
Scale Height/5-orbit mean	-	0.70	0.83
Altitude of 1.26 nbar level (km)	-	123	132
Atmospheric Disturbance Level(2sig%)	115.6	101.7	54.6

Max density(18.97 kg/km3) and max dynamic pressure(0.203 N/m2) occurs
 22 sec after periapsis

NAV Intermediate Density Solution = 15.66 kg/km3

Periapsis Density/ NAV Intermediate Density Solution Ratio= 1.07

LATITUDINAL VARIATION

[61.3 N. Lat (LST= 11.77 hrs, SZA= 85.08 deg) / 48.0 N. Lat (LST=
 11.59 hrs, SZA= 71.88 deg)]

Altitude= 130.00 km
 Density Ratio= 0.28
 Density Scale Height Ratio= 0.79
 Delta Atmospheric Temperature= -24.64 K

COMMENTS:

1) We predict the following periapsis densities and dynamic pressures
 over the next 7 passes (uncertainties are +116 %/- 54 %). Periapsis
 altitudes and longitudes were obtained from optg_i_980305_OD161_171_V1;
 Periapsis 151 through 162 were considered in the analysis.

Periapsis_	Alt (km)	E. Long(deg)	Density(kg/km3)	DynPres(N/m2)
163	120.43	-164.00	8.35	0.09
164	120.73	-6.31	9.48	0.10
165	121.14	152.26	9.90	0.11
166	121.17	-48.23	11.15	0.12
167	120.97	112.19	16.47	0.18
168	120.78	-86.51	14.33	0.15
169	120.76	75.70	18.56	0.20

2) After correcting for altitude, periapsis density is 2% above and
 maximum density is 16% above our P162 prediction given in the P161
 Intermediate Quick-Look.

3) After correcting for altitude, P162 periapsis density increased from
 P161 by 41%.

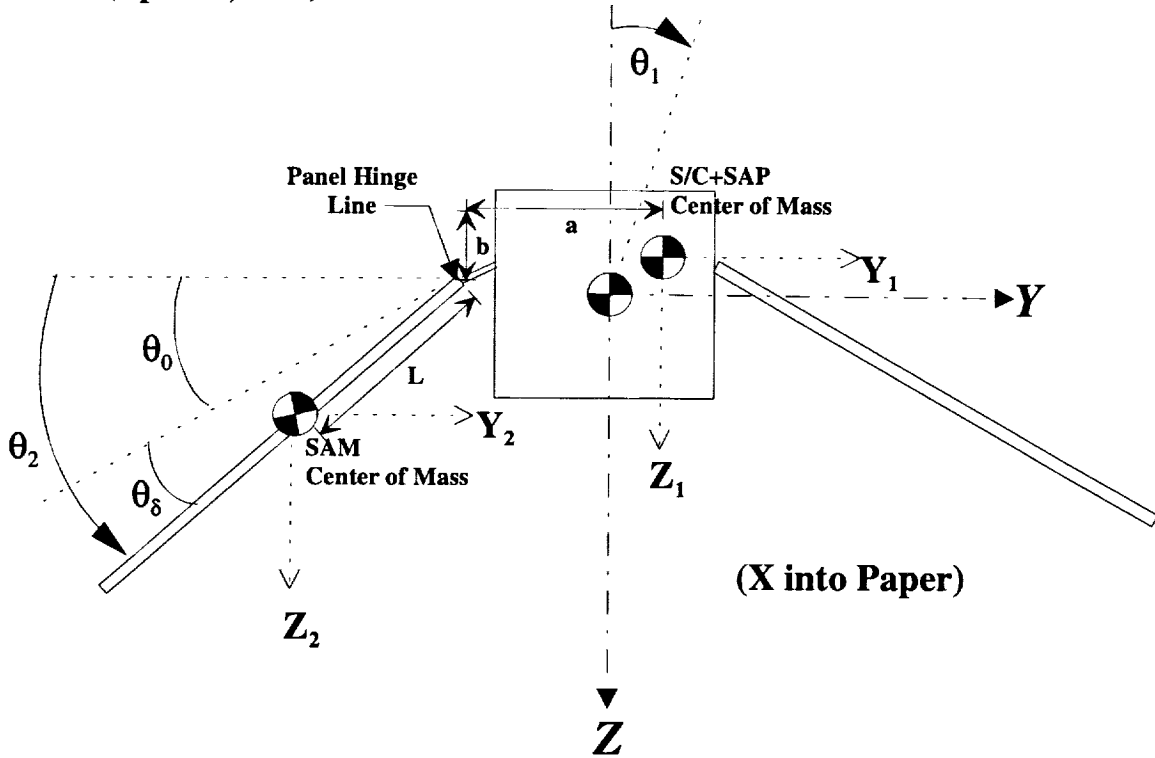
Line by Line Description of Intermediate Accelerometer Quick-Look Sheet

Line	Value	Description
1	<i>title</i>	
2	Date and Time (UTC)	Time of Periapsis Passage
3	Time of Calculation (EDT)	Eastern Daylight Time which sheet was created
4	OPTG filename	Name of NAV file used to generate orbit data
5	<i>blank</i>	
6	Periapsis#	Number of Periapsis used in Analysis
6	Ephemeris	Describes the type of NAV product used to develop QuickLook: (PREDICT, INTERMEDIATE, FINAL)
7	Altitude of Periapsis	Geodetic Altitude of S/C periapsis in degrees
7	Periapsis N. Lat	Geodetic North Latitude of S/C Periapsis in degrees
8	Periapsis E. Long	East Longitude of S/C in degrees, developed using Mars pole parameters in OPTG at Date and Time
9	Periapsis Local Solar Time	Local Solar Time of S/C in hours measure from real sun subsol point at Date and Time (24 hours/ day) (Midnight - >LST=0.0)
10	<i>blank</i>	
11	MGS Period from Periapsis Elements	Orbital period developed using periapsis orbital elements
11	Earth-Sun-Mars Angle	Angle between the Earth and Mars using the Sun as the middle point
12	<i>blank</i>	
13	<i>subtitle</i>	
14	<i>blank</i>	
15	Accel Bias +/- Std. Error	Accelerometer Instrument Bias and Standard Error calculated by averaging accelerometer values above the atmosphere before the start of the drag pass
15	Effective Density Scale Height for NAV	Density Scale Height in km corresponding to a spherically symmetrical atmosphere with a constant temperature. See Section 4.5.2
16	<i>blank</i>	
17	<i>subtitle</i>	
19	Effective Density	Density at periapsis and inbound and outbound reference altitudes
20	Scale Height	Scale height at periapsis and inbound and outbound reference altitudes
21	Estimated Temperature	Temperature at periapsis and inbound and outbound reference altitudes
22	Dynamic Pressure at Periapsis	Dynamic Pressure at Periapsis in N/m2 DYN. Press.=1/2*density (line 19) *Periapsis Velocity.**2
23	Freestream Heatflux at Periapsis	Freestream Heatflux at Periapsis in W/cm2 Qdot=1/2*density (line 19) *Periapsis Velocity.**3
24	Density/5-orbit mean	Density divided by mean of 5 previous densities
25	Scale height/5-orbit mean	Scale height divided by mean of 5 previous scale heights
26	Altitude of 1.26 nbar level	Altitude with pressure of 1.26 nbar
27	Atmospheric Disturbance Level	Volatility of atmosphere. See Section 4.5.3
28	<i>blank</i>	

29	Max density Occurrence	Density, dynamic pressure and time of maximum density in reference to periapsis time
31	NAV Density	Density Guess at periapsis from NAV
32	Periapsis Density/ NAV Density Predict Ratio	Ratio of Accelerometer density and NAV Predicted density RATIO=Line 19 / line 31
33	<i>blank</i>	
34	<i>subtitle</i>	
35	Variation Positions	Latitude, local solar time, and solar zenith angle of inbound and outbound reference altitude point
36	<i>blank</i>	
37	Altitude	Reference altitude for latitudinal variation
38	Density Ratio	Ratio of inbound and outbound densities at reference altitude
39	Density Scale Height Ratio	Ratio of inbound and outbound scale heights at reference altitude
40	Delta Atmospheric Temperature	inbound temperature minus the outbound temperature at reference altitude
41	Comments	Human analysis of 'Quick-Look' data
45	Predictions	Predictions for 7 upcoming orbits using wave model (see Section 4.6) and 10 previous orbits

Appendix B: 4 DOF Derivation for Eliminating SAM panel Motions from Z-Accelerometer Data

(April 27, 1998)



Kinetic Energies for 2 bodies (SAM and BUS+SAP)

(Where $\theta_1 \Rightarrow$ angle rotation about S/C positive x-axis

$\theta_2 \Rightarrow$ yoke azimuth angle plus panel deflection angle

$m_1 \Rightarrow$ mass of BUS + SAP

$m_2 \Rightarrow$ mass of SAM

z_1 and $y_1 \Rightarrow$ position of BUS/SAP C.O.M in S/C coordinates

z_2 and $y_2 \Rightarrow$ position of SAM C.O.M in S/C coordinates)

$$T_{BUS+SAP} = \frac{1}{2} m_1 \dot{y}_1^2 + \frac{1}{2} m_1 \dot{z}_1^2 + \frac{1}{2} I_{xx_{BUS+SAP}} \dot{\theta}_1^2 \quad (1)$$

$$T_{SAM} = \frac{1}{2} m_2 (\dot{y}_2^2 + \dot{z}_2^2) + \frac{1}{2} I_{xx_{SAM(SAMcom)}} (\dot{\theta}_1^2 - 2\dot{\theta}_2 \dot{\theta}_1 + \dot{\theta}_2^2) \quad (2)$$

Location and velocity of SAM C.O.M

(Where a => absolute value of y distance from BUS/SAP COM to line on which SAM hinges (hinge line or break line)

b => absolute value of z distance from BUS/SAP COM to line on which SAM hinges (hinge line or break line)

L => absolute value of distance from line on which SAM hinges to SAM COM)

$$y_2 = y_1 - a \cos \theta_1 - b \sin \theta_1 - L \cos(\theta_2 - \theta_1) \quad (3)$$

$$z_2 = z_1 - a \sin \theta_1 + b \cos \theta_1 + L \sin(\theta_2 - \theta_1) \quad (4)$$

Time Derivative of Equations 3 and 4

$$\dot{y}_2 = \dot{y}_1 + a\dot{\theta}_1 \sin \theta_1 - b\dot{\theta}_1 \cos \theta_1 + L(\dot{\theta}_2 - \dot{\theta}_1) \sin(\theta_2 - \theta_1) \quad (5)$$

$$\dot{z}_2 = \dot{z}_1 - a\dot{\theta}_1 \cos \theta_1 - b\dot{\theta}_1 \sin \theta_1 + L(\dot{\theta}_2 - \dot{\theta}_1) \cos(\theta_2 - \theta_1) \quad (6)$$

Small angle approximations of θ_1 and θ_2

(where small angle $\theta_1 = \delta\theta_1$, and derivative = $\delta\dot{\theta}_1$

small angle $\theta_2 = \theta_0 + \delta\theta_\delta$, and derivative = $\delta\dot{\theta}_\delta$)

$$\begin{aligned} \dot{y}_2 &\approx \dot{y}_1 + a\delta\dot{\theta}_1 \sin \delta\theta_1 - b\delta\dot{\theta}_1 \cos \delta\theta_1 + L(\delta\dot{\theta}_2 - \delta\dot{\theta}_1) \sin(\delta\theta_2 - \delta\theta_1) \\ \dot{y}_2 &\approx \dot{y}_1 + a\delta\dot{\theta}_1 \delta\theta_1 - b\delta\dot{\theta}_1 + L(\delta\dot{\theta}_\delta - \delta\dot{\theta}_1) \sin(\theta_0 + \delta\theta_\delta - \delta\theta_1) \\ \dot{y}_2 &\approx \dot{y}_1 + 0 - b\delta\dot{\theta}_1 + L(\delta\dot{\theta}_\delta - \delta\dot{\theta}_1) [\sin \theta_0 \cos(\delta\theta_\delta - \delta\theta_1) + \cos \theta_0 \sin(\delta\theta_\delta - \delta\theta_1)] \quad (7) \\ \dot{y}_2 &\approx \dot{y}_1 - b\delta\dot{\theta}_1 + L(\delta\dot{\theta}_\delta - \delta\dot{\theta}_1) [\sin \theta_0 + \cos \theta_0 (\delta\theta_\delta - \delta\theta_1)] \\ \dot{y}_2 &= \dot{y}_1 - b\delta\dot{\theta}_1 + L\delta\dot{\theta}_\delta \sin \theta_0 - L\delta\dot{\theta}_1 \sin \theta_0 \\ \dot{z}_2 &= \dot{z}_1 - a\delta\dot{\theta}_1 \cos \delta\theta_1 - b\delta\dot{\theta}_1 \sin \delta\theta_1 + L(\delta\dot{\theta}_2 - \delta\dot{\theta}_1) \cos(\delta\theta_2 - \delta\theta_1) \\ \dot{z}_2 &= \dot{z}_1 - a\delta\dot{\theta}_1 - b\delta\dot{\theta}_1 \delta\theta_1 + L(\delta\dot{\theta}_\delta - \delta\dot{\theta}_1) \cos(\theta_0 + \delta\theta_\delta - \delta\theta_1) \\ \dot{z}_2 &= \dot{z}_1 - a\delta\dot{\theta}_1 - 0 + L(\delta\dot{\theta}_\delta - \delta\dot{\theta}_1) [\cos \theta_0 \cos(\delta\theta_\delta - \delta\theta_1) - \sin \theta_0 \sin(\delta\theta_\delta - \delta\theta_1)] \quad (8) \\ \dot{z}_2 &= \dot{z}_1 - a\delta\dot{\theta}_1 + L(\delta\dot{\theta}_\delta - \delta\dot{\theta}_1) [\cos \theta_0 - \sin \theta_0 (\delta\theta_\delta - \delta\theta_1)] \\ \dot{z}_2 &= \dot{z}_1 - a\delta\dot{\theta}_1 + L\delta\dot{\theta}_\delta \cos \theta_0 - L\delta\dot{\theta}_1 \cos \theta_0 \end{aligned}$$

Kinetic and Potential Energy of System in terms of z_1 , y_1 , θ_1 , and θ_δ

$$T_{system} = T_{bus+sap} + T_{sam}$$

$$T_{system} = \frac{1}{2} m_1 (\dot{y}_1^2 + \dot{z}_1^2) + \frac{1}{2} I_{xx_{BUS+SAF}} \delta \dot{\theta}_1^2 + \frac{1}{2} m_2 (\dot{y}_2^2 + \dot{z}_2^2) + \frac{1}{2} I_{xx_{SAM(SAMcom)}} (\delta \dot{\theta}_1^2 - 2 \delta \dot{\theta}_1 \delta \dot{\theta}_\delta + \delta \dot{\theta}_\delta^2) \quad (9)$$

$$V_{system} = \int M d\theta = \int (T_c \theta^{X_e}) d\theta = \frac{1}{X_e + 1} T_c \theta^{X_e + 1} \quad (10)$$

$$L = T - V,$$

After forming the lagrangian, the z_1 , y_1 , θ_1 coordinates are found to be cyclic and the kinetic energy is a homogenous polynomial of degree 2, therefore the momentum in z_1 , y_1 , θ_1 is time independent (derivative equals zero)

$$\frac{d}{dt} \left(\frac{\partial L}{\partial \dot{y}_1} \right) = 0 \quad \frac{d}{dt} \left(\frac{\partial L}{\partial \dot{z}_1} \right) = 0 \quad \frac{d}{dt} \left(\frac{\partial L}{\partial \dot{\theta}_1} \right) = 0 \quad (11)$$

For corresponding momentum in y_1 :

$$\frac{\partial L}{\partial \dot{y}_1} = m_1 \dot{y}_1 + m_2 \dot{y}_2 \frac{\partial \dot{y}_2}{\partial \dot{y}_1} \quad \text{where } \dot{y}_2 = \dot{y}_1 - b \delta \dot{\theta}_1 + L \delta \dot{\theta}_\delta \sin \theta_0 - L \delta \dot{\theta}_1 \sin \theta_0$$

$$\text{and } \frac{\partial \dot{y}_2}{\partial \dot{y}_1} = 1$$

$$\text{therefore } \frac{\partial L}{\partial \dot{y}_1} = m_1 \dot{y}_1 + m_2 (\dot{y}_1 - b \delta \dot{\theta}_1 + L \delta \dot{\theta}_\delta \sin \theta_0 - L \delta \dot{\theta}_1 \sin \theta_0)$$

$$\frac{d}{dt} \left(\frac{\partial L}{\partial \dot{y}_1} \right) = m_1 \ddot{y}_1 + m_2 (\ddot{y}_1 - b \delta \ddot{\theta}_1 + L \delta \ddot{\theta}_\delta \sin \theta_0 - L \delta \ddot{\theta}_1 \sin \theta_0) = 0 \quad (12)$$

For corresponding momentum in z_1 :

$$\frac{\partial L}{\partial \dot{z}_1} = m_1 \dot{z}_1 + m_2 \dot{z}_2 \frac{\partial \dot{z}_2}{\partial \dot{z}_1} \quad \text{where } \dot{z}_2 = \dot{z}_1 - a \delta \dot{\theta}_1 + L \delta \dot{\theta}_\delta \cos \theta_0 - L \delta \dot{\theta}_1 \cos \theta_0$$

$$\text{and } \frac{\partial \dot{z}_2}{\partial \dot{z}_1} = 1$$

$$\text{therefore } \frac{\partial L}{\partial \dot{z}_1} = m_1 \dot{z}_1 + m_2 (\dot{z}_1 - a \delta \dot{\theta}_1 + L \delta \dot{\theta}_\delta \cos \theta_0 - L \delta \dot{\theta}_1 \cos \theta_0)$$

$$\frac{d}{dt} \left(\frac{\partial L}{\partial \dot{z}_1} \right) = m_1 \ddot{z}_1 + m_2 (\ddot{z}_1 - a \delta \ddot{\theta}_1 + L \delta \ddot{\theta}_\delta \cos \theta_0 - L \delta \ddot{\theta}_1 \cos \theta_0) = 0 \quad (13)$$

For corresponding momentum in θ_1 :

$$\frac{\partial L}{\partial \dot{\theta}_1} = m_2 \dot{z}_2 \frac{\partial \dot{z}_2}{\partial \dot{\theta}_1} + m_2 \dot{y}_2 \frac{\partial \dot{y}_2}{\partial \dot{\theta}_1} + I_{xx_{BUS+SAP}} \dot{\theta}_1 + I_{xx_{SAM(SAMcom)}} (\dot{\theta}_1 - \dot{\theta}_\delta)$$

where

$$\frac{\partial \dot{y}_2}{\partial \dot{\theta}_1} = -b - L \sin \theta_0 \quad \text{and} \quad \frac{\partial \dot{z}_2}{\partial \dot{\theta}_1} = -a - L \cos \theta_0$$

therefore

$$\begin{aligned} \frac{\partial L}{\partial \dot{\theta}_1} &= m_2 (\dot{z}_1 - a \dot{\theta}_1 + L \dot{\theta}_\delta \cos \theta_0 - L \dot{\theta}_1 \cos \theta_0) (-a - L \cos \theta_0) \\ &\quad + m_2 (\dot{y}_1 - b \dot{\theta}_1 + L \dot{\theta}_\delta \sin \theta_0 - L \dot{\theta}_1 \sin \theta_0) (-b - L \sin \theta_0) \\ &\quad + I_{xx_{BUS+SAP}} \dot{\theta}_1 + I_{xx_{SAM(SAMcom)}} (\dot{\theta}_1 - \dot{\theta}_\delta) \\ \frac{\partial L}{\partial \dot{\theta}_1} &= \dot{z}_1 (-m_2 a - m_2 L \cos \theta_0) + \dot{\theta}_1 (m_2 a^2 + 2m_2 a L \cos \theta_0 + m_2 L^2 \cos^2 \theta_0) \\ &\quad + \dot{\theta}_\delta (-m_2 a L \cos \theta_0 - m_2 L^2 \cos^2 \theta_0) + \dot{y}_1 (-m_2 b - m_2 L \sin \theta_0) + \\ &\quad + \dot{\theta}_1 (m_2 b^2 + 2m_2 b L \sin \theta_0 + m_2 L^2 \sin^2 \theta_0) + \dot{\theta}_\delta (-m_2 b L \sin \theta_0 - m_2 L^2 \sin^2 \theta_0) \\ &\quad + \dot{\theta}_1 (I_{xx_{BUS+SAP}} + I_{xx_{SAM(SAMcom)}}) - \dot{\theta}_\delta (I_{xx_{SAM(SAMcom)}}) \\ \frac{\partial L}{\partial \dot{\theta}_1} &= \dot{z}_1 (-m_2 a - m_2 L \cos \theta_0) + \dot{y}_1 (-m_2 b - m_2 L \sin \theta_0) \\ &\quad + \dot{\theta}_\delta (-m_2 a L \cos \theta_0 - m_2 L^2 - m_2 b L \sin \theta_0 - I_{xx_{SAM(SAMcom)}}) \\ &\quad + \dot{\theta}_1 (m_2 a^2 + 2m_2 a L \cos \theta_0 + m_2 L^2 + m_2 b^2 + 2m_2 b L \sin \theta_0 + I_{xx_{BUS+SAP}} + I_{xx_{SAM(SAMcom)}}) \end{aligned}$$

$$\begin{aligned} \frac{d}{dt} \left(\frac{\partial L}{\partial \dot{\theta}_1} \right) &= \ddot{z}_1 (-m_2 a - m_2 L \cos \theta_0) + \ddot{y}_1 (-m_2 b - m_2 L \sin \theta_0) \\ &\quad + \ddot{\theta}_\delta (-m_2 a L \cos \theta_0 - m_2 L^2 - m_2 b L \sin \theta_0 - I_{xx_{SAM(SAMcom)}}) \\ &\quad + \ddot{\theta}_1 (m_2 a^2 + 2m_2 a L \cos \theta_0 + m_2 L^2 + m_2 b^2 + 2m_2 b L \sin \theta_0 + I_{xx_{BUS+SAP}} + I_{xx_{SAM(SAMcom)}}) = 0 \end{aligned}$$

Using the momentum equations, 3 equations are produced with 4 unknowns (y_1 z_1 θ_1 and θ_δ) . However, θ_1 in this problem is known as the S/C x-angular position, which is delivered as x-angular rate data once every sec during the drag pass.

This reduces this problem to 3 equations and 3 unknowns that can be solved for dz_1/dt every sec which is the change in velocity each second measured by the z-accelerometer due to the motion of the SAM panel if there are no outside forces on the panel and if small angles apply. This data can be removed from the

acceleration signal further reducing the false signals read by the instruments due to S/C motion.

3 Equations used shown below:

$$(m_1 + m_2)\ddot{y}_1 + (-m_2b - m_2L\sin\theta_0)\delta\ddot{\theta}_1 + (m_2L\sin\theta_0)\delta\ddot{\theta}_\delta = 0 \quad (15)$$

$$(m_1 + m_2)\ddot{z}_1 + (-m_2a - m_2L\cos\theta_0)\delta\ddot{\theta}_1 + (m_2L\cos\theta_0)\delta\ddot{\theta}_\delta = 0 \quad (16)$$

$$\begin{aligned} &\ddot{z}_1(-m_2a - m_2L\cos\theta_0) + \ddot{y}_1(-m_2b - m_2L\sin\theta_0) \\ &+ \delta\ddot{\theta}_\delta(-m_2aL\cos\theta_0 - m_2L^2 - m_2bL\sin\theta_0 - I_{xx_{SAM(SAMcom)}}) \\ &+ \delta\ddot{\theta}_1(m_2a^2 + 2m_2aL\cos\theta_0 + m_2L^2 + m_2b^2 + 2m_2bL\sin\theta_0 + I_{xx_{BUS+SAP}} + I_{xx_{SAM(SAMcom)}}) = 0 \end{aligned} \quad (17)$$

These are solved by setting the following constants:

$$\begin{aligned} a11 &= m_1 + m_2 & a21 &= 0 \\ a12 &= 0 & a22 &= m_1 + m_2 \\ a13 &= -m_2b - m_2L\sin\theta_0 & a23 &= -m_2a - m_2L\cos\theta_0 \\ a14 &= m_2L\sin\theta_0 & a24 &= m_2L\cos\theta_0 \\ a31 &= -m_2b - m_2L\sin\theta_0 \\ a32 &= -m_2a - m_2L\cos\theta_0 \\ a33 &= m_2a^2 + 2m_2aL\cos\theta_0 + m_2L^2 + m_2b^2 + 2m_2bL\sin\theta_0 + I_{xx_{BUS+SAP}} + I_{xx_{SAM(SAMcom)}} \\ a34 &= -m_2aL\cos\theta_0 - m_2L^2 - m_2bL\sin\theta_0 - I_{xx_{SAM(SAMcom)}} \end{aligned}$$

$$\begin{bmatrix} a11 & a12 & a13 & a14 \\ a21 & a22 & a23 & a24 \\ a31 & a32 & a33 & a34 \\ 0 & 0 & 0 & 0 \end{bmatrix} \begin{bmatrix} \ddot{y}_1 \\ \ddot{z}_1 \\ \delta\ddot{\theta}_1 \\ \delta\ddot{\theta}_\delta \end{bmatrix} = \begin{bmatrix} 0 \\ 0 \\ 0 \\ 0 \end{bmatrix} \quad \begin{bmatrix} a11 & a12 & a14 \\ a21 & a22 & a24 \\ a31 & a32 & a34 \end{bmatrix} \begin{bmatrix} \ddot{y}_1 \\ \ddot{z}_1 \\ \delta\ddot{\theta}_\delta \end{bmatrix} = \begin{bmatrix} -a13 \\ -a23 \\ -a33 \end{bmatrix} \delta\ddot{\theta}_1$$

$$\begin{bmatrix} 1 & 0 & \frac{a14}{a11} \\ 0 & a22 & \frac{a24}{a11} \\ a31 & a32 & \frac{a34}{a11} \end{bmatrix} \begin{bmatrix} \ddot{y}_1 \\ \ddot{z}_1 \\ \delta\ddot{\theta}_\delta \end{bmatrix} = \begin{bmatrix} \frac{-a13}{a11} \\ \frac{-a23}{a11} \\ \frac{-a33}{a11} \end{bmatrix} \delta\ddot{\theta}_1 \quad \begin{bmatrix} 1 & 0 & \frac{a14}{a22} \\ 0 & 1 & \frac{a24}{a22} \\ a31 & a32 & \frac{a34}{a22} \end{bmatrix} \begin{bmatrix} \ddot{y}_1 \\ \ddot{z}_1 \\ \delta\ddot{\theta}_\delta \end{bmatrix} = \begin{bmatrix} \frac{-a13}{a22} \\ \frac{-a23}{a22} \\ \frac{-a33}{a22} \end{bmatrix} \delta\ddot{\theta}_1$$

$$\begin{bmatrix} 1 & 0 & \frac{a14}{a11} \\ 0 & 1 & \frac{a24}{a11} \\ 0 & a32 & a34 - a31\frac{a14}{a11} \end{bmatrix} \begin{bmatrix} \ddot{y}_1 \\ \ddot{z}_1 \\ \delta\ddot{\theta}_\delta \end{bmatrix} = \begin{bmatrix} \frac{-a13}{a11} \\ \frac{-a23}{a11} \\ -a33 + a31\frac{a13}{a11} \end{bmatrix} \delta\ddot{\theta}_1 \quad \begin{bmatrix} 1 & 0 & \frac{a14}{a22} \\ 0 & 1 & \frac{a24}{a22} \\ 0 & 0 & C_1 - a32\frac{a24}{a22} \end{bmatrix} \begin{bmatrix} \ddot{y}_1 \\ \ddot{z}_1 \\ \delta\ddot{\theta}_\delta \end{bmatrix} = \begin{bmatrix} \frac{-a13}{a22} \\ \frac{-a23}{a22} \\ C_2 + a32\frac{a23}{a22} \end{bmatrix} \delta\ddot{\theta}_1$$

where $C_1 = a_{34} - a_{31} \cdot (a_{14}/a_{11})$ and $C_2 = -a_{33} + a_{31} \cdot (a_{13}/a_{11})$
 $C_3 = C_1 - a_{32} \cdot (a_{24}/a_{22})$ and $C_4 = C_2 + a_{32} \cdot (a_{23}/a_{22})$

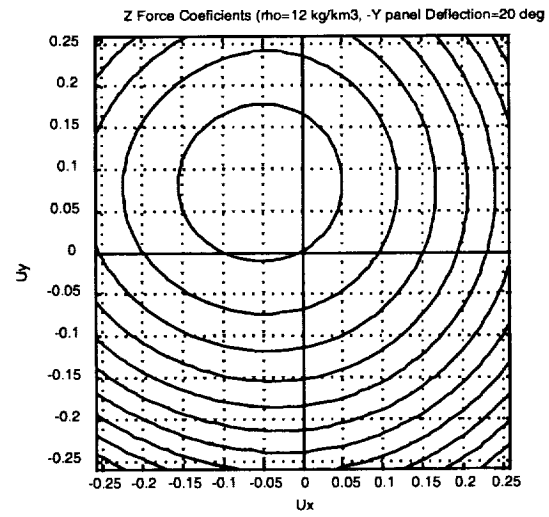
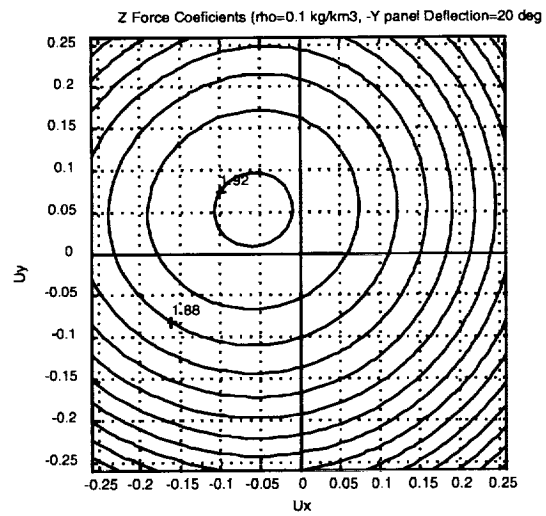
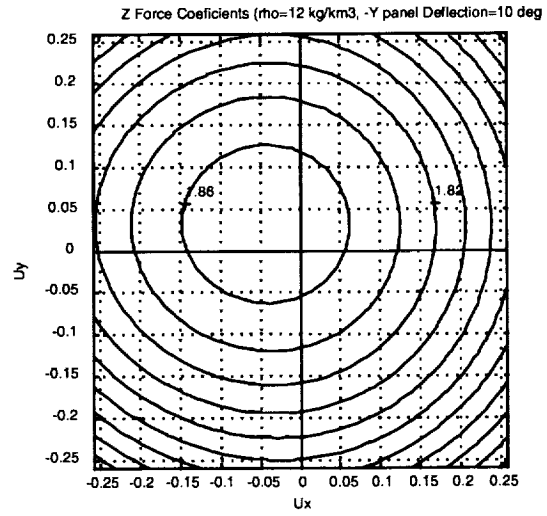
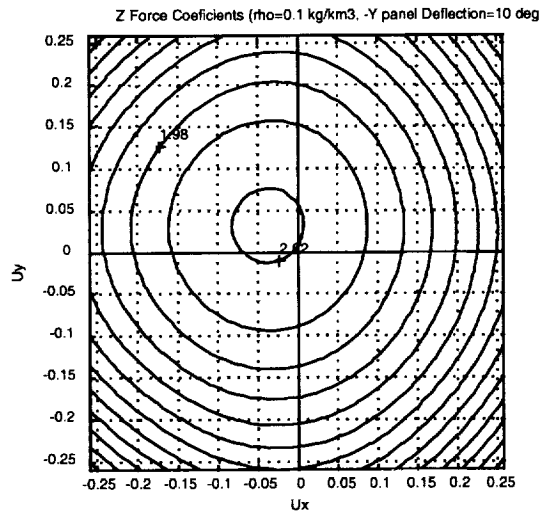
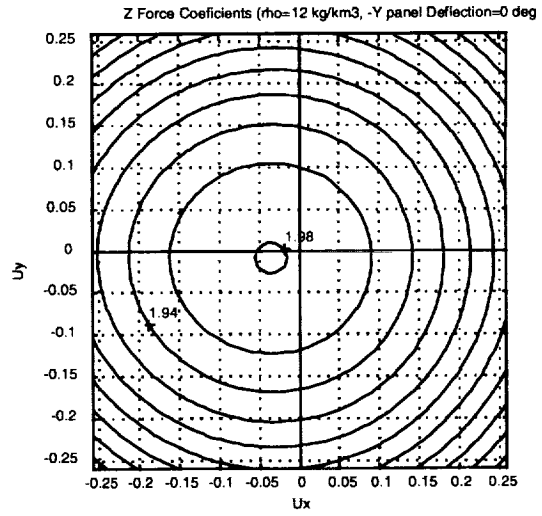
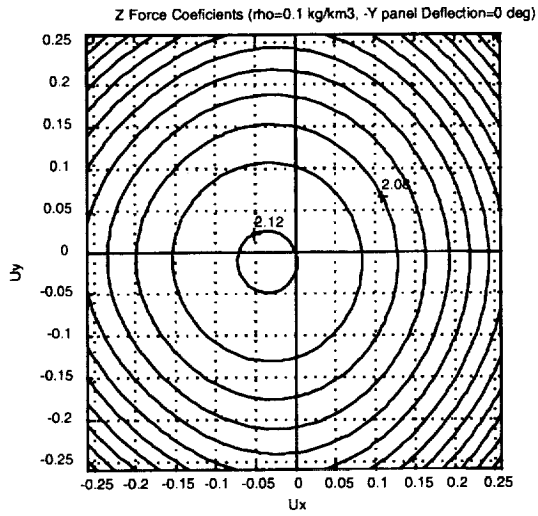
$$\begin{bmatrix} 1 & 0 & \frac{a_{14}}{a_{11}} \\ 0 & 1 & \frac{a_{24}}{a_{22}} \\ 0 & 0 & C_3 \end{bmatrix} \begin{bmatrix} \ddot{y}_1 \\ \ddot{z}_1 \\ \delta \ddot{\theta}_\delta \end{bmatrix} = \begin{bmatrix} -\frac{a_{13}}{a_{11}} \\ -\frac{a_{23}}{a_{22}} \\ \frac{C_4}{C_3} \end{bmatrix} \delta \ddot{\theta}_1$$

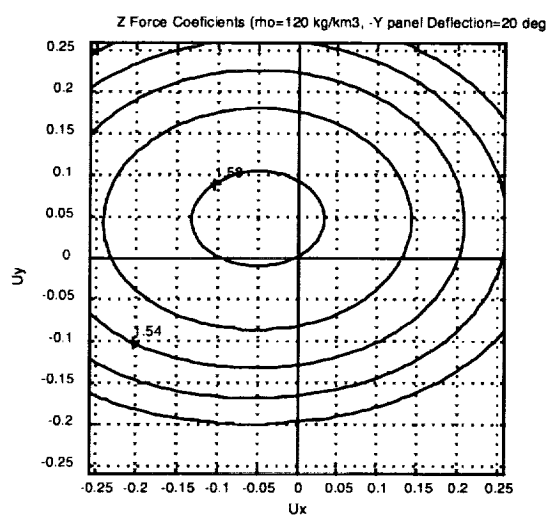
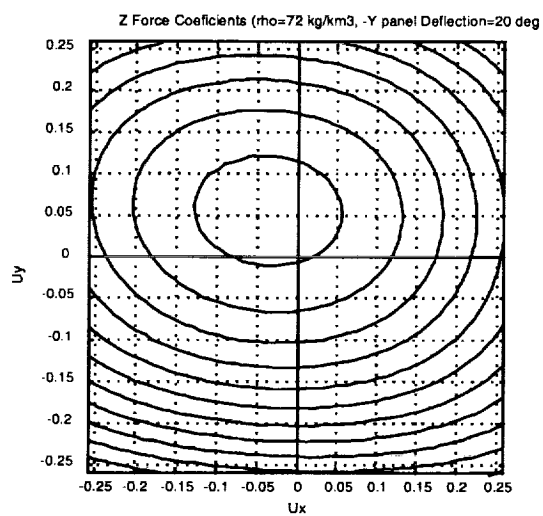
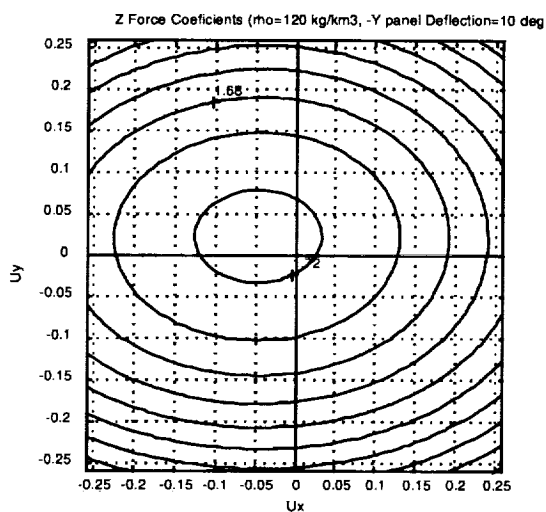
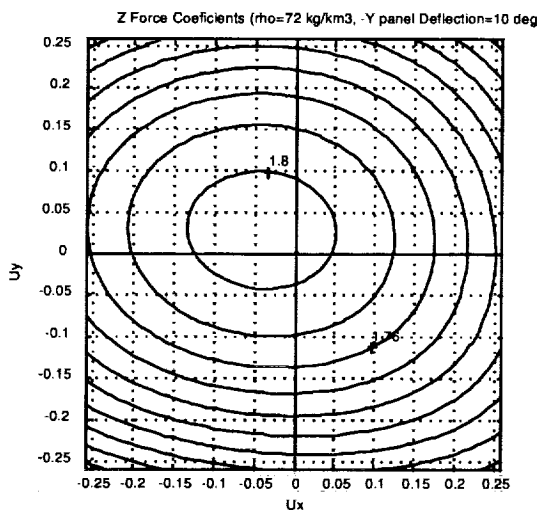
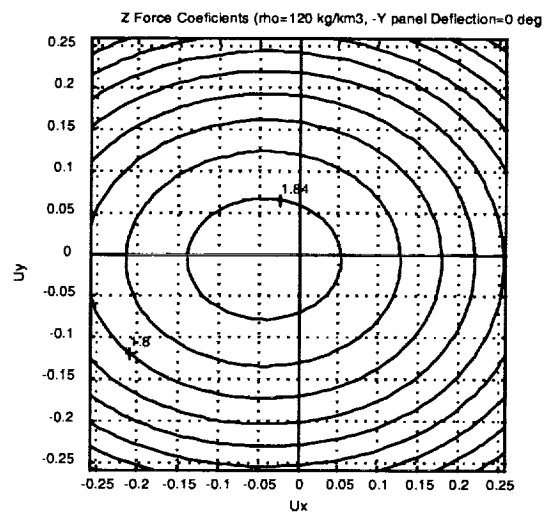
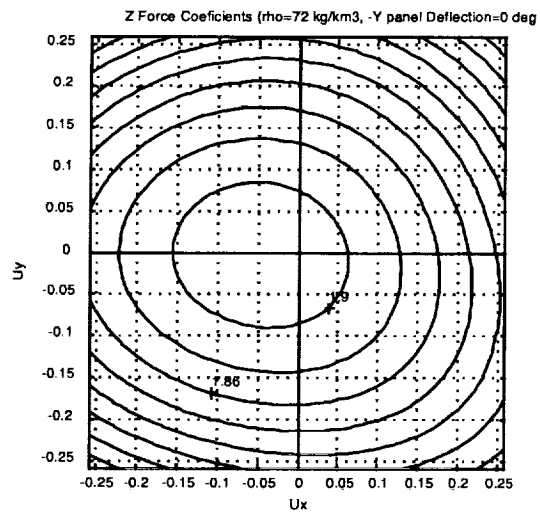
$$\begin{bmatrix} 1 & 0 & \frac{a_{14}}{a_{11}} \\ 0 & 1 & \frac{a_{24}}{a_{22}} \\ 0 & 0 & 1 \end{bmatrix} \begin{bmatrix} \ddot{y}_1 \\ \ddot{z}_1 \\ \delta \ddot{\theta}_\delta \end{bmatrix} = \begin{bmatrix} -\frac{a_{13}}{a_{11}} \\ -\frac{a_{23}}{a_{22}} \\ \frac{C_4}{C_3} \end{bmatrix} \delta \ddot{\theta}_1$$

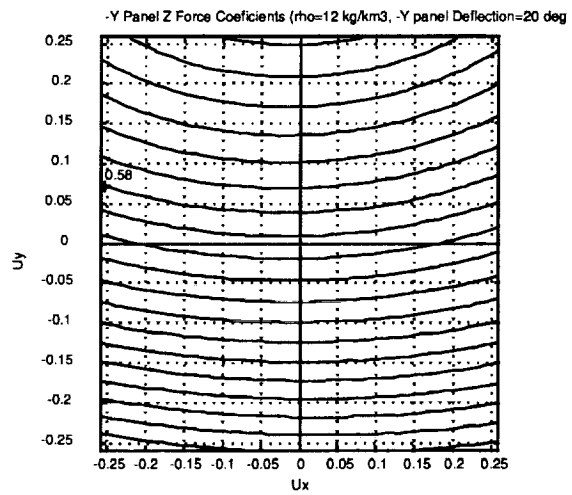
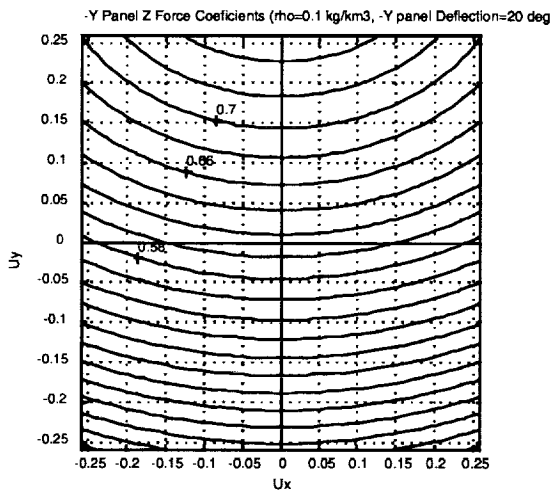
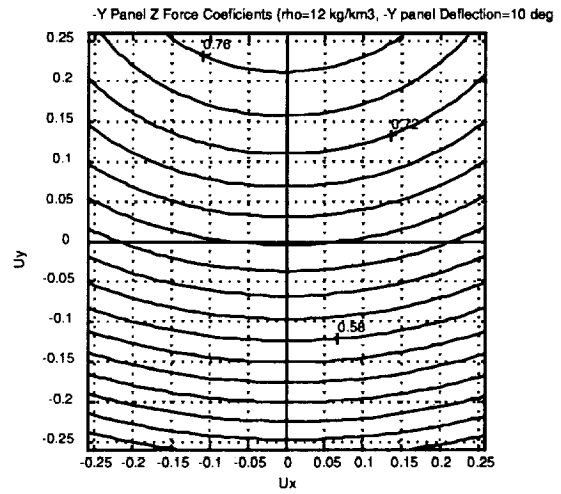
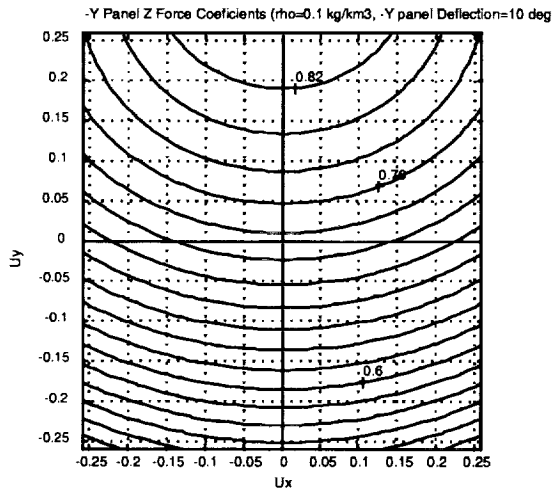
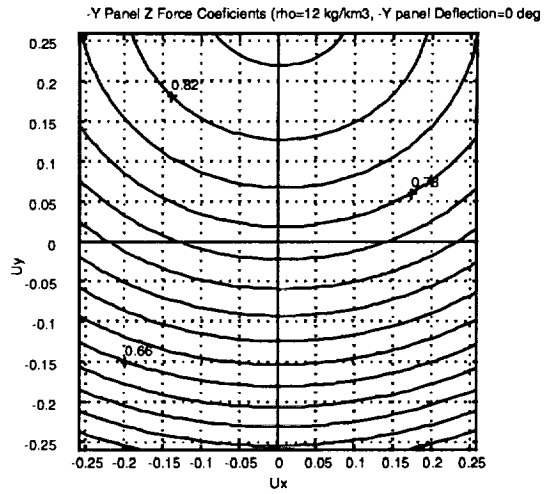
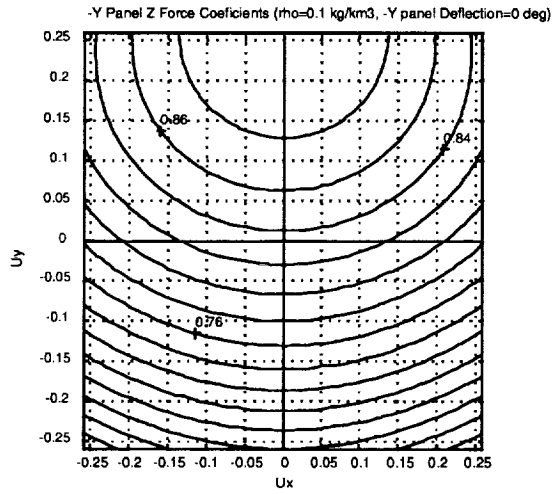
$$\begin{bmatrix} 1 & 0 & \frac{a_{14}}{a_{11}} \\ 0 & 1 & 0 \\ 0 & 0 & 1 \end{bmatrix} \begin{bmatrix} \ddot{y}_1 \\ \ddot{z}_1 \\ \delta \ddot{\theta}_\delta \end{bmatrix} = \begin{bmatrix} -\frac{a_{13}}{a_{11}} \\ -\frac{a_{23}}{a_{22}} - \frac{a_{24} C_4}{a_{22} C_3} \\ \frac{C_4}{C_3} \end{bmatrix} \delta \ddot{\theta}_1$$

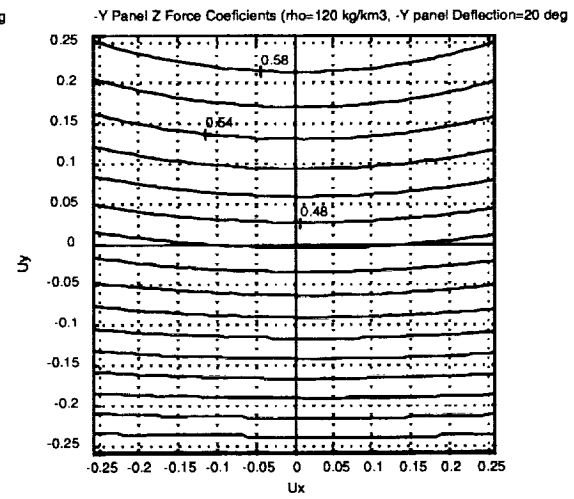
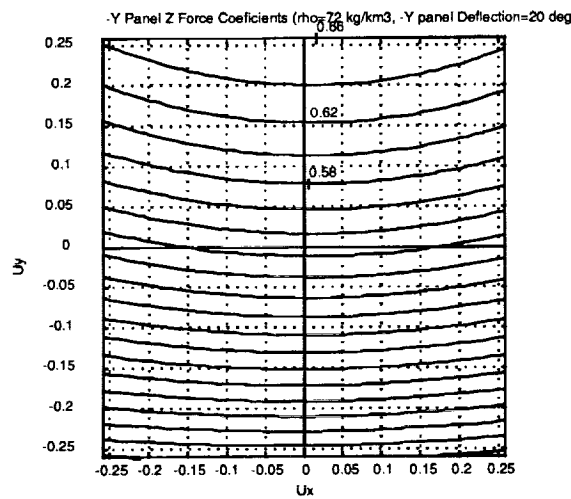
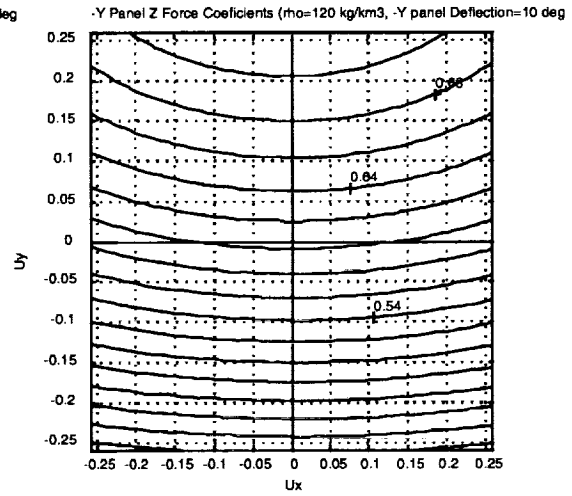
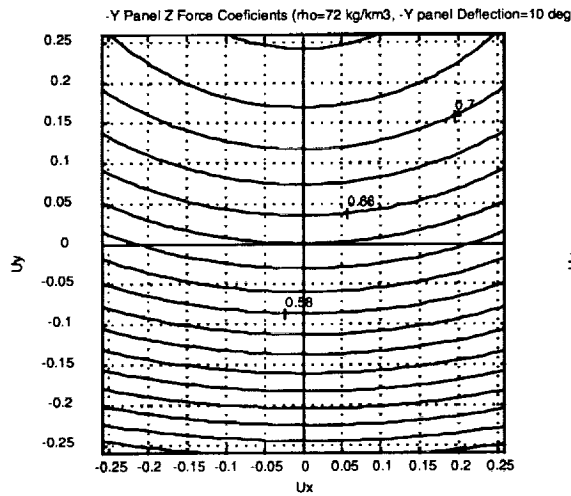
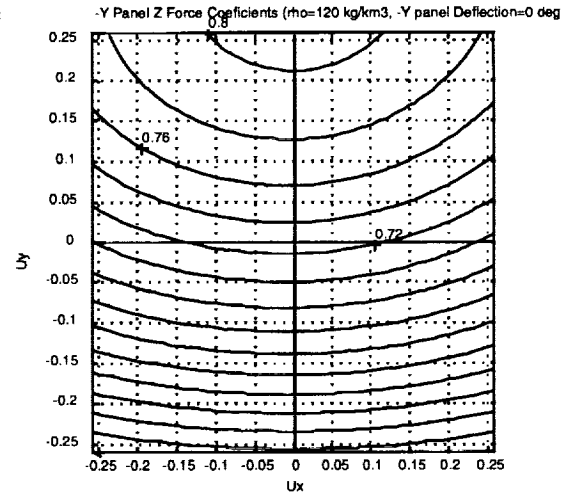
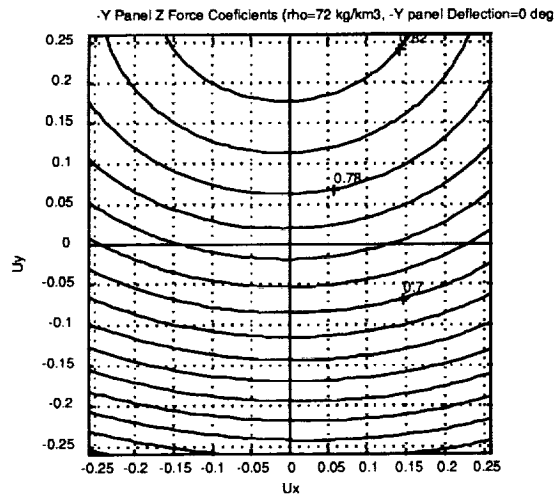
$$\begin{bmatrix} 1 & 0 & 0 \\ 0 & 1 & 0 \\ 0 & 0 & 1 \end{bmatrix} \begin{bmatrix} \ddot{y}_1 \\ \ddot{z}_1 \\ \delta \ddot{\theta}_\delta \end{bmatrix} = \begin{bmatrix} -\frac{a_{13}}{a_{11}} - \frac{a_{14} C_4}{a_{11} C_3} \\ -\frac{a_{23}}{a_{22}} - \frac{a_{24} C_4}{a_{22} C_3} \\ \frac{C_4}{C_3} \end{bmatrix} \delta \ddot{\theta}_1$$

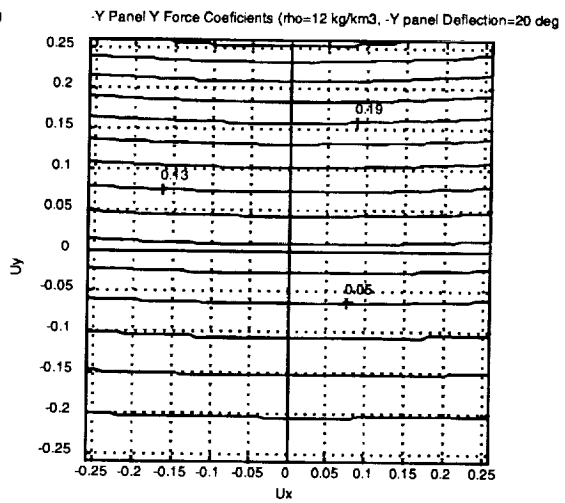
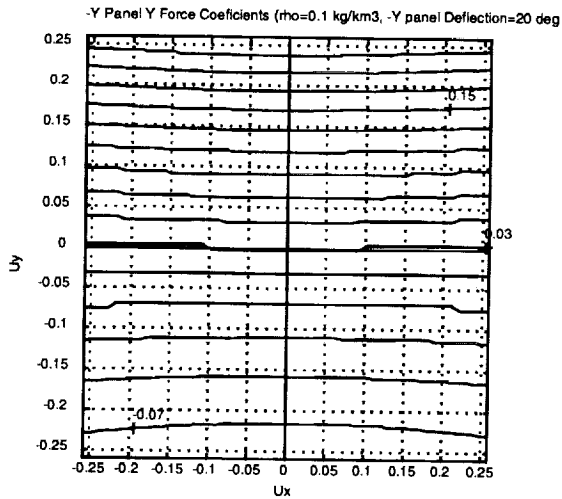
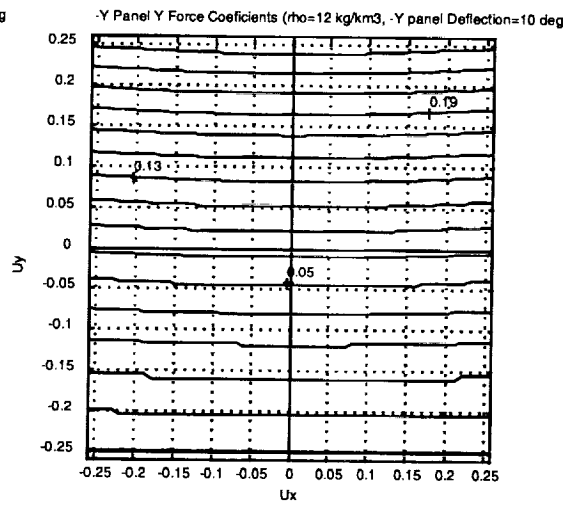
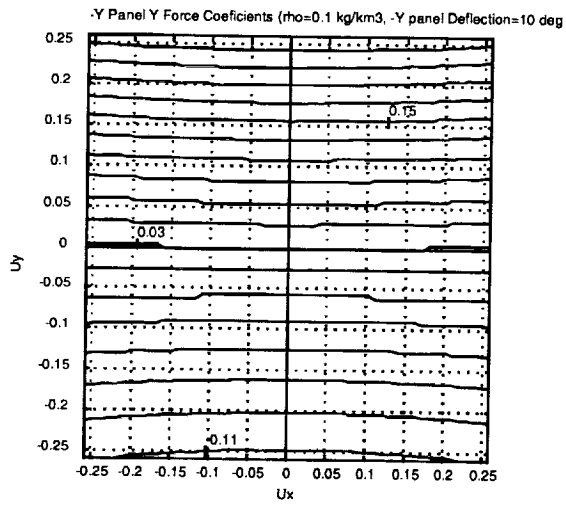
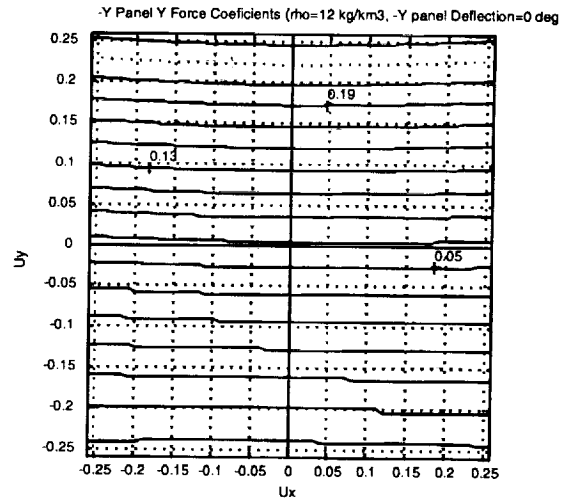
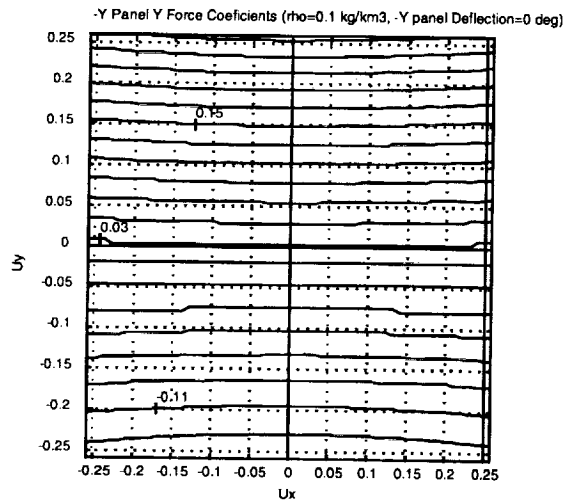
Appendix C: LaRC Aerothermodynamic Database for MGS Operations

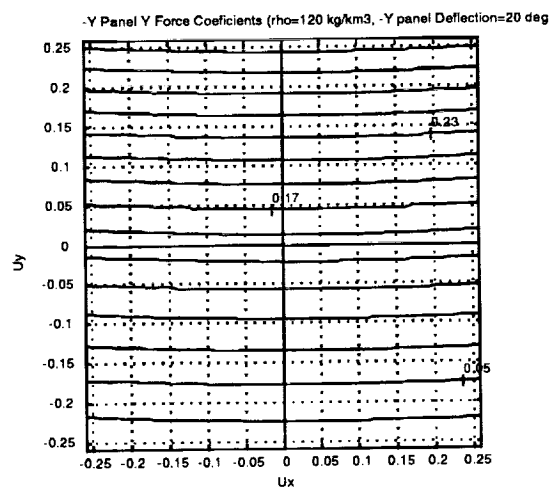
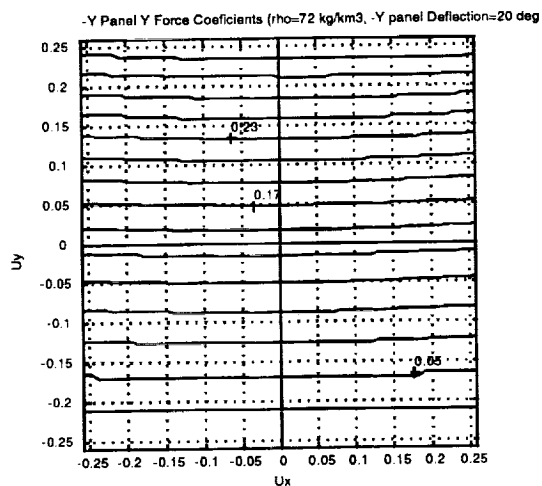
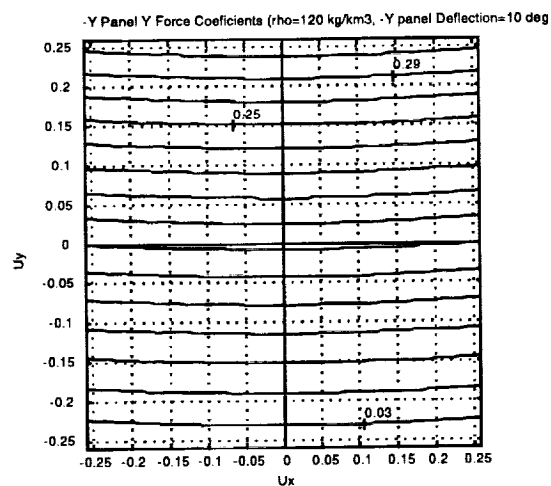
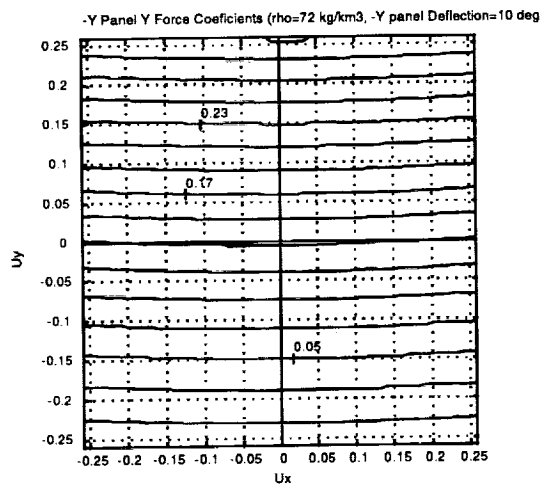
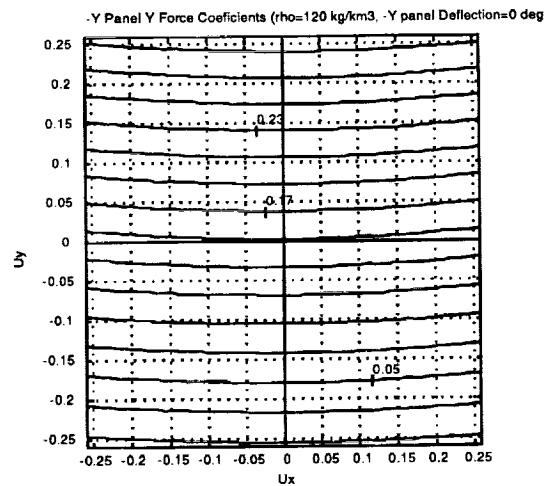
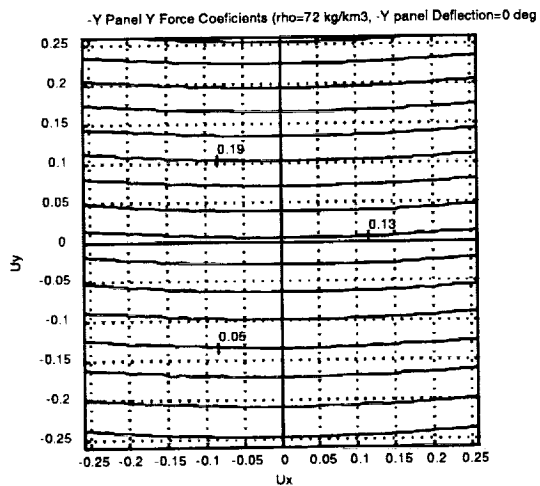


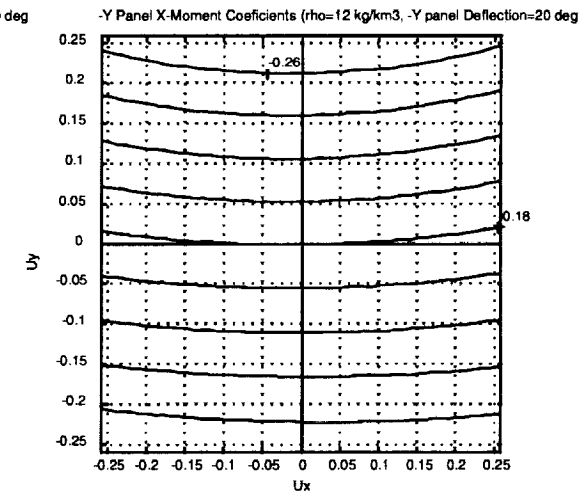
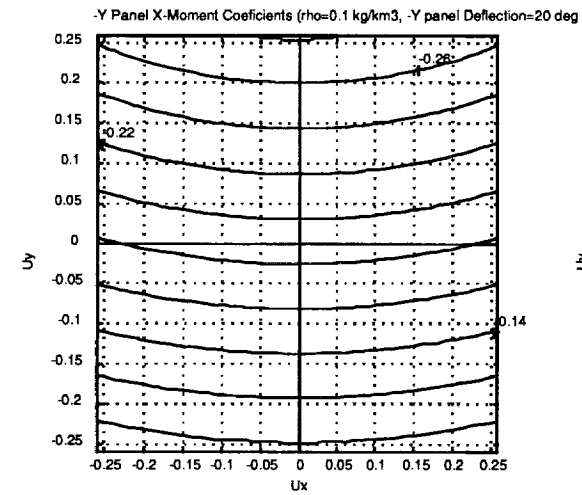
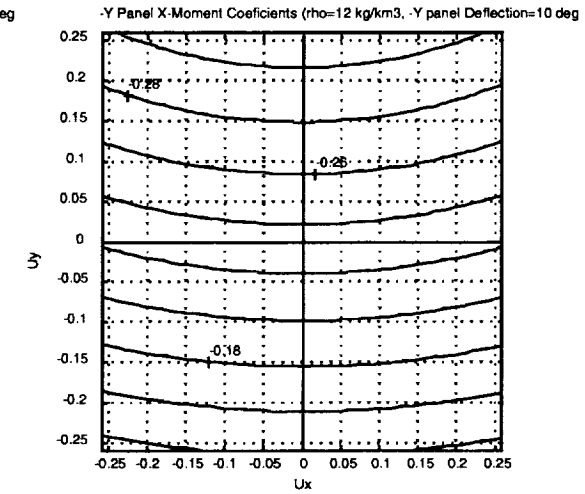
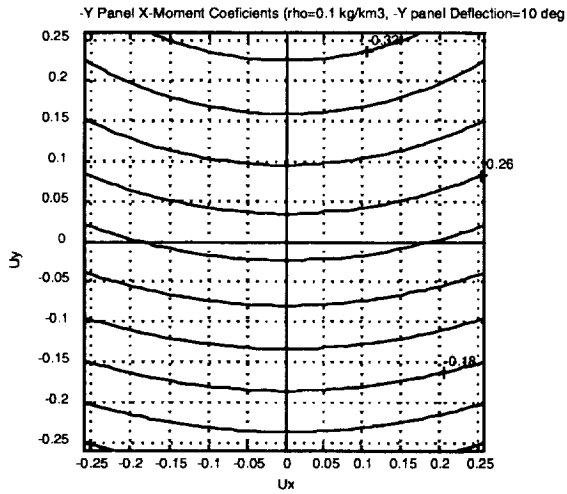
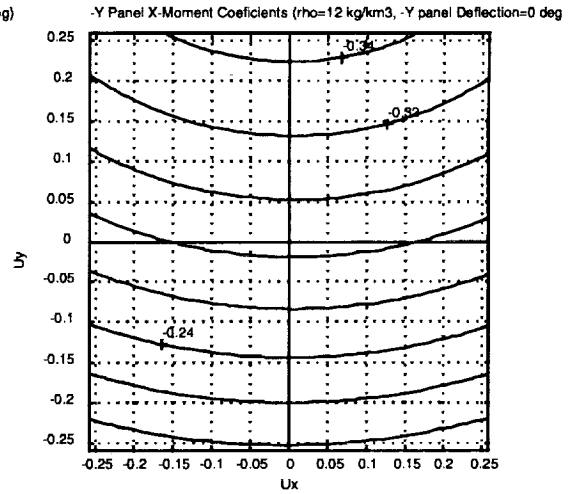
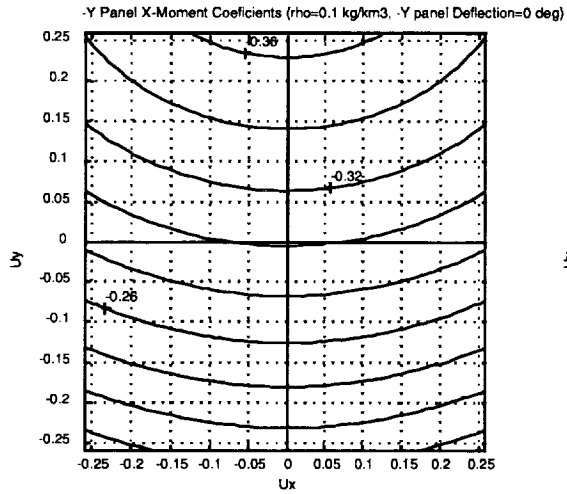


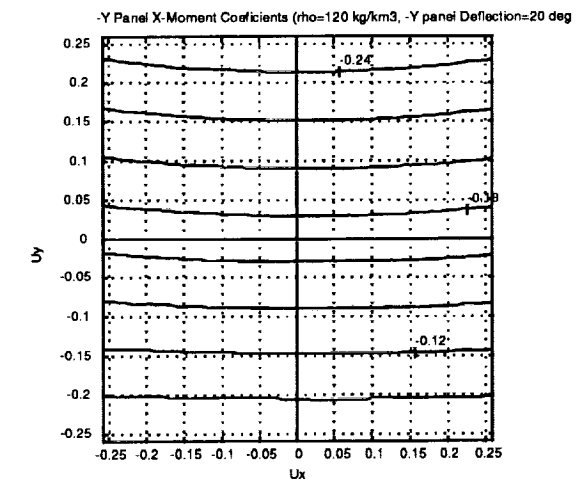
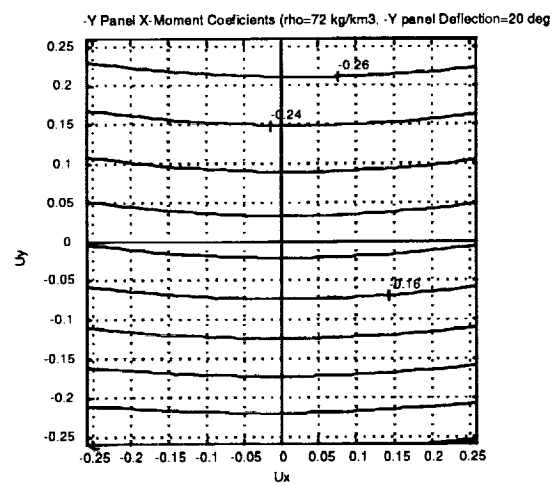
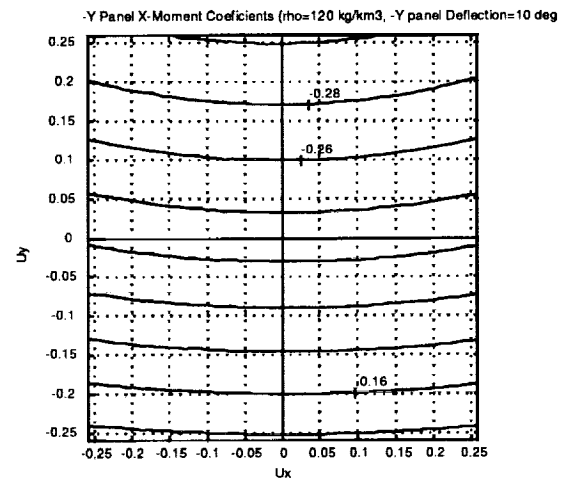
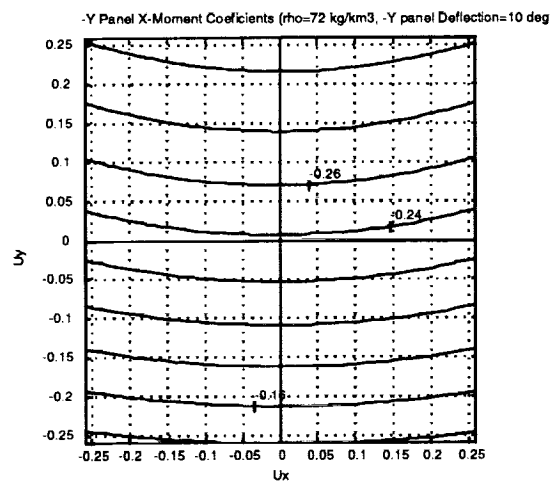
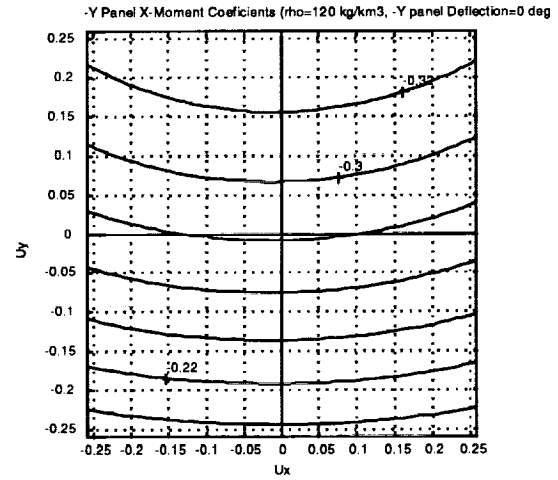
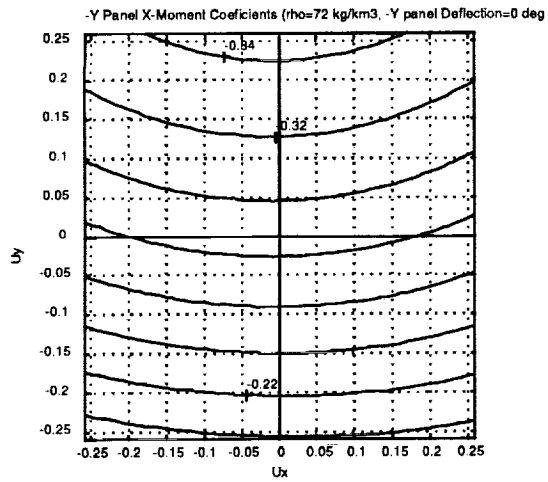












Appendix D: Planetary Ephemeris and Physical Data

Basic Parameters

Gravitational Constant for the Sun = $1.3331 \times 10^{11} \text{ km}^3/\text{s}^2$

Julian Day of J2000 = 2451545

Astronomical Unit (AU) = 149597870 km

MARS Planet Global Parameters

Gravitational Constant for Mars = $42828 \text{ km}^3/\text{s}^2$

Flattening = 0.0052

Equatorial Radius = 3393.4 km

Polar Radius = 3375.7 km

Right Ascension of Pole = 317.6810 degrees

Declination of Pole = 52.8860 degrees

Prime Meridian Position = 176.8680 degrees

Linear term for Right Ascension = -0.1080 degrees/Julian century

Linear term for Declination = -0.0610 degrees/Julian century

Linear term for Meridian Position = 350.8920 degrees/day

Mars Orbital Elements (Danby, p428)

(T = Julian Century)

semi-major axis, $a = 1.5236793419 \text{ AU}$; (**from Almanac)

eccentricity, $e = 0.09340062 + 0.00009048T - 0.00000008T^2$;

inclination, $i = 1.849726 - 0.000601T + 0.000013 T^2$;

longitude of ascending node, $\Omega = 49.558093 + 0.772096T + 0.000016 T^2$;

argument of periapsis, $w = 336.0602 + 1.841044T + 0.000135 T^2 - \Omega$;

true longitude, $L = 355.433275 + 19141.696475T + 0.000311 T^2$;

Earth Solar Longitude (Danby, p428)

$L_{\text{earth}} = 100.466449 + 36000.7698T + 0.000304 T^2$;

REFERENCES:

Danby, J.M.A, Fundamentals of Celestial Mechanics, 2nd Edition, Willmann-Bell Inc., 1992

Seidelmann, K., Explanatory Supplement to the Astronomical Almanac, University Science Books, Mill Valley, CA, 1992.

Appendix E: MGS Physical Properties

	Mid Yoke Failure (D. Shafter)			Hinge Line Failure		
S/C Mass (kg)		763.2			763.2	
S/C CG (m)	-3E-04	-0.0011	1.355	-3E-04	-0.001	1.355
Ixx S/C about S/C CG (kg-m ²)		1043			1043	
SAM Mass (kg)		39.34			27.896	
SAM Azimuth (deg)		33.4			33.4	
SAM CG (m)	-0.006	-2.386	2.07	-0.023	-2.789	2.3388
Ixx SAM about SAM CG (kg-m ²)		64.805			47.09	
Distance from S/C CG to SAM CG	0.0057	2.3849	-0.715	0.0223	2.7883	-0.984
		(2.4898)			(2.9569)	
Location of Failure Line (m)	0.0381	-0.9045	1.086	0.0381	-1.313	1.355
Distance from Failure to SAM CG		1.7791			1.7752	
BUS+SAP Mass		723.86			735.3	
BUS+SAP CG	1E-05	0.1285	1.31614	0.0005	0.1047	1.3177
Distance from B+S CG to SAM CG	0.006	2.5145	-0.7539	0.0231	2.8941	-1.021
		(2.6251)			(3.069)	
Ixx SAM about B+S CG		335.9			309.84	
Distance from B+S CG to S/C CG	0.0003	0.1296	-0.0389	0.0008	0.1058	-0.037
		(0.1353)			(0.1122)	
Ixx BUS+SAP about B+S CG		693.84			723.91	
		a	b		a	b
ABS(Dist. from B+S CG to Failure)	0.0381	1.033	0.23014	0.0376	1.4177	0.0373
Position of Z accelerometer	-0.44	-0.38	2.05	-0.44	-0.38	2.05

Appendix F: Verification of 4-DOF Model Derivation

Mid Yoke Failure (D. Shafter)			
S/C Mass (kg)	783.2		
S/C CG (m)	-0.0003	-0.0011	1.355
Ixx S/C about S/C CG (kg-m ²)	1043		
SAM Mass (kg)	39.34		
SAM Azimuth (deg)	33.4		
SAM CG (m)	-0.006	-2.386	2.07
Ixx SAM about SAM CG (kg-m ²)	64.805		
Distance from S/C CG to SAM CG	0.005701	2.384901	-0.715
		(2.489781)	
Location of Failure Line (m)	0.0381	-0.8045	1.086
Distance from Failure to SAM CG		1.779057	
BUS+SAP Mass		723.86	
BUS+SAP CG	1.09E-05	0.128514	1.316142
Distance from B+S CG to SAM CG	0.006011	2.514514	-0.75386
		(2.625095)	
Ixx SAM about B+S CG		335.9017	
Distance from B+S CG to S/C CG	0.00031	0.129613	-0.03888
		(0.135313)	
Ixx BUS+SAP about B+S CG		893.8446	
	a	b	
ABS(Dist. from B+S CG to Failure)	0.038089	1.033014	0.230142
Position of Z accelerometer	-0.44	-0.38	2.05
Distance from Z accel to B+S CG, (R1)	-0.44001	-0.50851	0.733858
Distance from Z accel to S/C CG, (R2)	-0.4307	-0.3789	0.695

EQUATIONS OF MOTION

$$1) a_{11} \ddot{Y} + a_{13} \ddot{T}_1 + a_{14} \ddot{T}_2 = 0$$

$$a_{11} = 783.2$$

$$a_{13} = -47.5809$$

$$a_{14} = 0$$

$$2) a_{22} \ddot{Z} + a_{23} \ddot{T}_1 + a_{24} \ddot{T}_2 = 0$$

$$a_{22} = 783.2$$

$$a_{23} = -99.0682$$

$$a_{24} = 0$$

$$2) a_{31} \ddot{Y} + a_{32} \ddot{Z}$$

$$a_{31} = -47.5809$$

$$+ a_{33} \ddot{T}_1 + a_{34} \ddot{T}_2 = 0$$

$$a_{32} = -99.0682$$

$$a_{33} = 1065.677$$

$$a_{34} = 0$$

Linear Component

$$\ddot{z} = (-a_{23}/a_{22}) \ddot{T}_1$$

$$\ddot{z} = 0.129806 \ddot{T}_1 \text{ m/s}^2$$

Angular Component

$$\ddot{z} = \ddot{T}_1 \text{ r1}$$

$$\ddot{z} = -0.50851 \ddot{T}_1 \text{ m/s}^2$$

$$\ddot{z} \text{ TOTAL} = C_2 \ddot{T}_1$$

$$C_2 = (\ddot{z} \text{ linear} + \ddot{z} \text{ angular})$$

$$C_2 = -0.3787 \text{ m/s}^2 / (\text{rad/s}^2)$$

$$(\text{in counts}) \quad C_2 = -1140.7 \text{ counts}/(\text{rad/s}^2)$$

Just Angular Component

$$\ddot{z} = \ddot{T}_1 \text{ r2}$$

$$\ddot{z} = -0.3789 \ddot{T}_1 \text{ m/s}^2$$

$$C_2 = -0.3789 \text{ m/s}^2 / (\text{rad/s}^2)$$

$$(\text{in counts}) \quad C_2 = -1141.3 \text{ counts}/(\text{rad/s}^2)$$

REPORT DOCUMENTATION PAGE			Form Approved OMB No. 0704-0188	
Public reporting burden for this collection of information is estimated to average 1 hour per response, including the time for reviewing instructions, searching existing data sources, gathering and maintaining the data needed, and completing and reviewing the collection of information. Send comments regarding this burden estimate or any other aspect of this collection of information, including suggestions for reducing this burden, to Washington Headquarters Services, Directorate for Information Operations and Reports, 1215 Jefferson Davis Highway, Suite 1204, Arlington, VA 22202-4302, and to the Office of Management and Budget, Paperwork Reduction Project (0704-0188), Washington, DC 20503.				
1. AGENCY USE ONLY (Leave blank)		2. REPORT DATE October 1998		3. REPORT TYPE AND DATES COVERED Contractor Report
4. TITLE AND SUBTITLE Operational Data Reduction Procedure for Determining Density and Vertical Structure of the Martian Upper Atmosphere From Mars Global Surveyor Accelerometer Measurements			5. FUNDING NUMBERS NCC1-104 865-10-03-01	
6. AUTHOR(S) George J. Cancro, Robert H. Tolson, and Gerald M. Keating				
7. PERFORMING ORGANIZATION NAME(S) AND ADDRESS(ES) The George Washington University Joint Institute for Advancement of Flight Sciences NASA Langley Research Center Hampton, VA 23681-2199			8. PERFORMING ORGANIZATION REPORT NUMBER	
9. SPONSORING/MONITORING AGENCY NAME(S) AND ADDRESS(ES) National Aeronautics and Space Administration Langley Research Center Hampton, VA 23681-2199			10. SPONSORING/MONITORING AGENCY REPORT NUMBER NASA/CR-1998-208721	
11. SUPPLEMENTARY NOTES The information submitted in this report was offered as a thesis by the first author in partial fulfillment of the requirements for the Degree of Master of Science, The George Washington University, JIAFS. Langley Technical Monitor: Robert Buchan				
12a. DISTRIBUTION/AVAILABILITY STATEMENT Unclassified-Unlimited Subject Category 91 Distribution: Nonstandard Availability: NASA CASI (301) 621-0390			12b. DISTRIBUTION CODE	
13. ABSTRACT (Maximum 200 words) The success of aerobraking by the Mars Global Surveyor (MGS) spacecraft was partly due to the analysis of MGS accelerometer data. Accelerometer data was used to determine the effect of the atmosphere on each orbit, to characterize the nature of the atmosphere, and to predict the atmosphere for future orbits. To interpret the accelerometer data, a data reduction procedure was developed to produce density estimations utilizing inputs from the spacecraft, the Navigation Team, and pre-mission aerothermodynamic studies. This data reduction procedure was based on the calculation of aerodynamic forces from the accelerometer data by considering acceleration due to gravity gradient, solar pressure, angular motion of the MGS, instrument bias, thruster activity, and a vibration component due to the motion of the damaged solar array. Methods were developed to calculate all of the acceleration components including a 4 degree of freedom dynamics model used to gain a greater understanding of the damaged solar array. The total error inherent to the data reduction procedure was calculated as a function of altitude and density considering contributions from ephemeris errors, errors in force coefficient, and instrument errors due to bias and digitization. Comparing the results from this procedure to the data of other MGS Teams has demonstrated that this procedure can quickly and accurately describe the density and vertical structure of the Martian upper atmosphere.				
14. SUBJECT TERMS Mars Global Surveyor mission; Space flight; Mechanics			15. NUMBER OF PAGES 106	
			16. PRICE CODE A06	
17. SECURITY CLASSIFICATION OF REPORT Unclassified	18. SECURITY CLASSIFICATION OF THIS PAGE Unclassified	19. SECURITY CLASSIFICATION OF ABSTRACT Unclassified	20. LIMITATION OF ABSTRACT	

NSN 7540-01-280-5500

Standard Form 298 (Rev. 2-89)
Prescribed by ANSI Std. Z-39-18